Alma Mater Studiorum · Università di Bologna

School of Science
Department of Physics and Astronomy
Master Degree Programme in Astrophysics and Cosmology

Investigating Ionized Gas Emission in Massive Quiescent Galaxies at Cosmic Noon with JWST

Graduation Thesis

Presented by:
Letizia Bugiani

Supervisor:
Chiar.mo Prof. Sirio Belli
Co-supervisor:
Prof. Andrea Cimatti

Academic Year 2022/2023
Graduation Date III

Abstract

The study of massive, quiescent galaxies at high redshift is crucial for understanding the physical processes driving galaxy evolution. The presence of a large population of such galaxies already in place at z $\sim$ 2 poses the questions of how they formed and what mechanisms hide behind the quenching of their star formation. The advent of the James Webb Space Telescope (JWST) has opened up a new window into the early universe, making it possible to study high-redshift quiescent galaxies in detail. The aim of this work is to analyze ionized gas emission lines found in the near-infrared spectra of quiescent galaxies at z $\sim$ 2, in order to derive information about the underlying sources of ionization and thus constrain the quenching mechanism.

This work is based on proprietary data from the Blue Jay survey (PI: S. Belli), carried out with the NIRCam and NIRSpec instruments onboard JWST. The survey observed a total of 147 galaxies at $1.7 < z < 3.5$ in the COSMOS field, using three filters of medium resolution R $\sim$ 1000 covering the 1 - 5 micron wavelength range. A sample of massive quiescent galaxies was selected by employing a rest-frame UVJ color selection and selecting only systems with stellar mass $M_* \geq 10^{10}$ $M_\odot$: the final sample consists of 22 galaxies.

Their spectra were continuum fitted using the `Prospector` code for stellar population inference and then continuum subtracted, in order to isolate rest-frame optical emission lines produced by ionized gas. The most prominent lines detected are Hα, Hβ, [OII]$\lambda\lambda$3727,3729, [OIII]$\lambda\lambda$4959,5007, [NII]λ6548, [NII]λ6583, [SII]$\lambda\lambda$6716,6731 and He I λ10830: these were all fitted using single Gaussian model profiles. At least one emission line from ionized gas was detected with SNR>3 in 82% of the sample (i.e. 18 out of 22 galaxies), indicating the presence of continued ionizing sources in this passive population.

From the results of the line fits I obtained the emission line flux ratios and used them to investigate the primary source of excitation through line diagnostic diagrams, such as the [OIII]λ5007/Hβ vs [NII]λ6583/Hα ratios - known as the BPT diagram, after Baldwin, Phillips, and Terlevich (1981) - the Hα equivalent width vs [NII]λ6583/Hα diagram, from Cid Fernandes, Stasińska, Mateus, and Vale Asari (2011), and two other. All of these diagrams found that most of the sample's galaxies fall under the AGN-powered excitation range: of the whole sample, 12 out of 22 galaxies (54.5%) were able to be classified using diagnostic diagrams, and, among these, 8 systems (67%) were confirmed to host an active nucleus.

The accuracy of the UVJ color selection was tested by measuring the current SFR of each galaxy from the Hα line luminosity. The majority of the sample was indeed confirmed to be quiescent, with only 2 galaxies (9% of the selected sample) who turned out to be star-forming and 1 galaxy found to actually be a merger.

Finally, in 4 galaxies I found that the spectral fitting required multiple Gaussian components in order to accurately replicate the observed emission lines. To further investigate this occurrence, I included for each emission line a narrow and a broad component, the former fixed at systemic velocity and the latter free to vary in redshift. This improved fitting unveiled the presence of powerful ionized gas outflows in all four galaxies, plus the presence of very clear Broad Line Region emission in only one of them, COSMOS-18977. These ionized gas outflows are actively leaving their galaxies

with measured velocities of the order of 1000s of km/s and are thus only traceable back to AGN-feedback at work in these passive systems.

The general picture emerging from this study is that massive quiescent galaxies at Cosmic Noon may harbour a significant fraction of never-before-detected AGNs. The high percentage of nuclear activity present in this quiescent population is a strong indication of AGN activity and feedback as the primary channel of star-formation quenching at work in these massive and passive systems. Furthermore, the detection of ionized gas outflows in a subset of active galaxies in the sample is an even more direct evidence of AGN feedback actively quenching these galaxies through gas ejection at very high velocities, further reinforcing the link between quenching of star-formation in massive quiescent galaxies and AGN activity.

Contents

Chapter 1

Introduction

1.1 Main properties of quiescent galaxies

Historically, galaxies have been first and foremost classified through their morphology observed in optical images: this classification is referred to as *morphological classification* and it was first defined by Hubble in 1926. It is still in use today and sees the galaxy population divided into two main separate groups: the early-type galaxies (or ETGs), which include ellipticals and lenticular galaxies, and the late-type galaxies (or LTGs), which comprises spirals and irregular galaxies. This basic classification is then articulated in many subclasses that make up the classic "tuning fork" Hubble classification scheme (Figure 1.1).

The fundamental bimodality present in the ETG vs LTG morphological classification correlates with the bimodal distribution of many galaxy properties: ETGs tend to be quite red in their photometric colors, while LTGs are characterized by bluer SEDs; star formation rate is very low in early-types and much higher in late-types; UV-optical spectra of late-type galaxies are characterized by powerful emission lines, while UV-optical spectra of ETGs typically do not show any emission lines but are instead rich in deep absorption lines. Figure 1.2 shows the color-mass diagram of a sample of present day galaxies, divided by morphology types: ETGs and LTGs are segregated in different parts of the diagram, reflecting the bimodal distribution in colors.

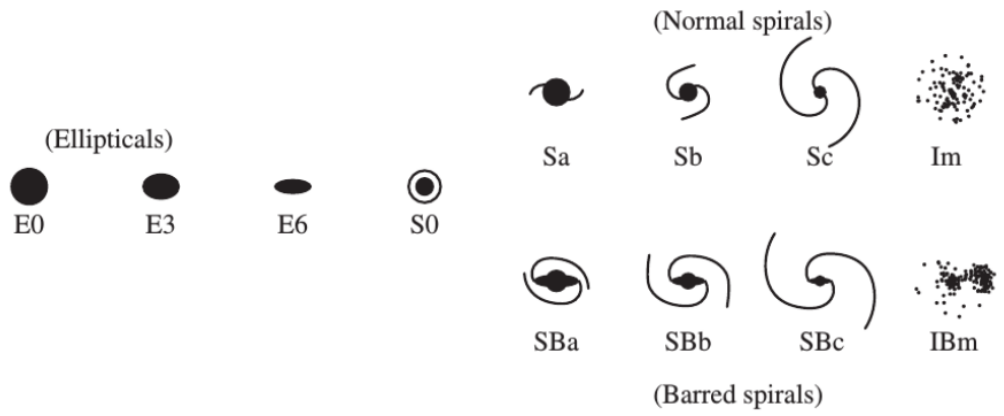

Figure 1.1: *The Hubble "tuning fork" classification scheme. From Mo et al. (2010).*

The correlation between morphology and rate of star formation is the reason why ETGs are often referred to as *quiescent* or *passive* galaxies, while LTGs are called *star-forming* galaxies: it is important, however, to stress the difference between the morphological distribution, which is based on imaging data and is quite dependent on the wavelength at which a galaxies is observed at, and the SFR-based one, which usually relies on SFR measurement from spectroscopic data and thus it's based on the spectrum of a galaxy rather than its image. Even though the two classification are tightly correlated, this does not mean that they always overlap (Moresco et al., 2013). Since this work is primarily based on spectroscopic data of cosmic-noon galaxies (i.e., at $z \sim 2$), from now on we will refer to the galaxies in the sample by using the star-forming/quiescent spectroscopic classification.

Quiescent galaxies are characterized by low or completely absent star formation. For example, a galaxy may be classified as quiescent adopting a threshold of SFR < 1 $M_\odot$/yr or $\log(\mathrm{sSFR/Gyr}) < -1$ (Pozzetti et al., 2010). Quiescent systems are typically high-mass galaxies (with stellar masses $> 10^{10}$ $M_\odot$) made up of evolved stellar populations, and are generally quite gas-poor and dust-poor.

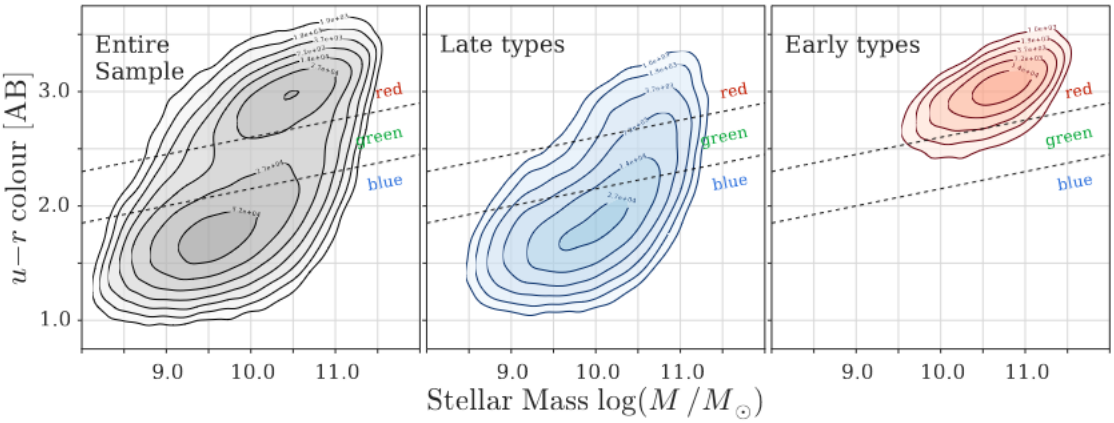

Figure 1.2: *The rest-frame $u-r$ color index as a function of stellar mass for a sample of* $\sim$ 100000 *present-day galaxies, from Weigel et al. (2016).*

1.2 Evolution of quiescent galaxies and the role of quenching

Though many different evolutionary scenarios of quiescent galaxy formation have been proposed through the years, the theory of ETGs formation is not yet fully understood. Some of the most famous scenarios proposed are the *monolithic collapse* theory (Arimoto & Yoshii, 1987; Bressan, Chiosi, & Fagotto, 1994), by which quiescent galaxies formed on very rapid time scales through the collapse of a single protogalaxy that produced a violent starburst event followed by a passive evolution of the stellar population and the *hierarchical merging* theory (Blumenthal, Faber, Primack, & Rees, 1984; White & Rees, 1978), which supports the thesis that modern-day ETGs are the results of the hierarchical assembly of pre-existing galaxies through mergers.

In recounting the evolution of quiescent galaxies, anyway, it's important to distinguish between the *star formation history* and the *star formation assembly* of the

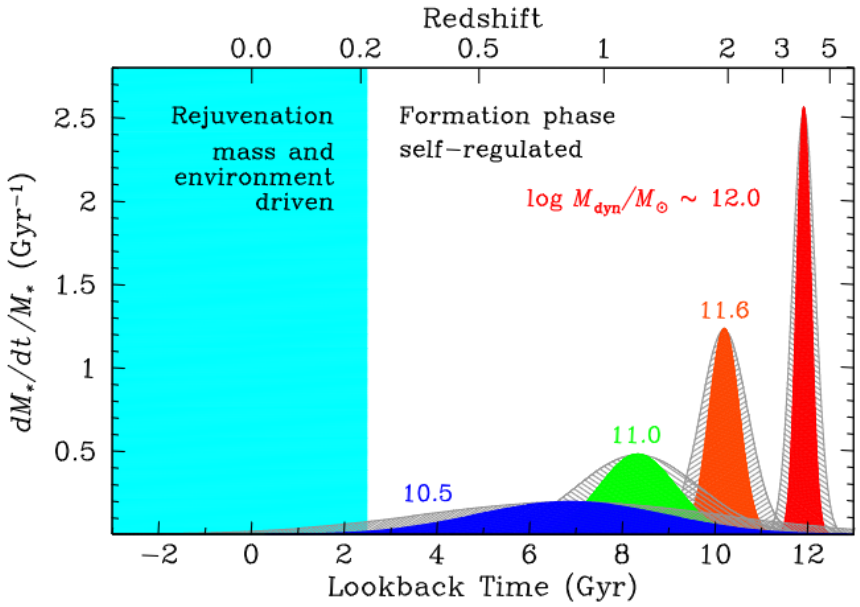

Figure 1.3: *The downsizing scenario: specific SFR as function of look-back time for early-type galaxies of various masses as indicated by the labels. From Thomas et al. (2010).*

galaxy, particularly in the case of ETGs: while the former simply refers to the stars actually formed by the galaxy as a function of time, the latter describes how the galaxy has accreted stars from dry mergers during its evolution. A widely accepted framework consists in the *two-phase* formation model in which we can distinguish a first, rapid phase of *in situ* star formation followed by a prolonged hierarchical phase of *ex situ* stellar mass assembly.

1.2.1 Quiescent galaxy evolution from observations

The standard and widely accepted ΛCDM cosmological model puts forward the idea that galaxies are formed through a *hierarchical* process, in which smaller DM halos merge together and produce in this way more massive halos, with baryonic matter following suit: according to this model, in our Universe the first structures to form were the smallest ones, gradually increasing in size through mergers and producing the large scale structures that we observe today. Thus, the expectation would be to observe massive systems only at low redshift and to find younger stellar populations in the more massive galaxies, since they would be the ones to have formed more recently.

In the past few years, however, it has become evident that there exists an extraordinary population of massive galaxies which have already ceased their star formation and become quiescent when the universe was just 2 billion years old ($z \geq 3$) (Carnall et al., 2023; Girelli, Bolzonella, & Cimatti, 2019; Marsan et al., 2017; Schreiber et al., 2018). Furthermore, the detailed study of the star formation history of present-day quiescent galaxies in the so-called *archeological approach* has brought to light an unexpected evolutionary picture called *the downsizing scenario*. According to Thomas et al. (2010), ETGs do not share the "bottom-up" evolution scheme of DM halos, but instead show the opposite behaviour: it seems that the most massive systems actually formed *earlier* and with much more rapid star formation than smaller systems (see Figure 1.3). These

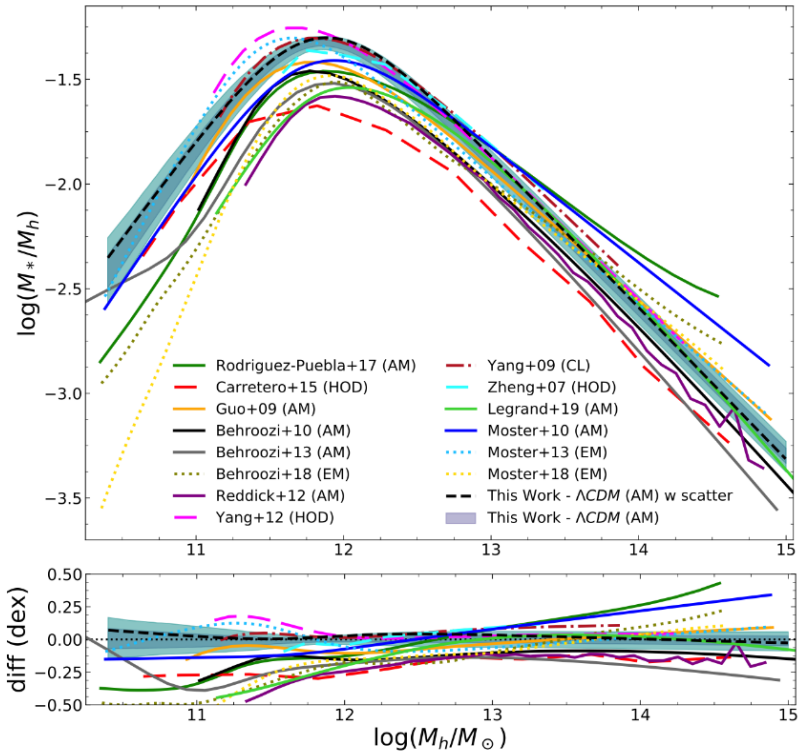

Figure 1.4: *Ratio between DM halo and galaxy mass function in a variety of studies from $z \sim 4$ to the present. As we can see, the ratio dips both at the low-mass and at the high-mass end. From Girelli et al. (2020).*

observations are in contrast with the hierarchical assembly paradigm of ΛCDM.

Another point of dissonance between modern cosmology and observational astrophysics concerning massive galaxies is the discrepancy between the observed galaxy mass function and the theoretical halo mass function. The predicted mass function distribution of baryonic matter in galaxies is supposed to mirror the DM halos' own mass function, since according to ΛCDM, the collapse of baryonic matter always follows the one of dark matter. However, as illustrated by Figure 1.4, the observed galaxy mass function does not follow the dark matter's one, but instead we observe a decrease in density with respect to the DM halos both at the low-mass and the high-mass end of the spectrum. This issue clearly affects the quiescent population, since the majority of massive galaxies are quiescent.

1.2.2 The role of quenching

If a suitable mechanism is discovered to be capable of successfully quenching star formation in massive galaxies at early times, we would have explained the observed downsizing scenario and provided a justification to the poor star-formation efficiency at the higher end of the DM halo mass function. Thus, star-formation *quenching* is invoked as a fundamental step in the evolution of quiescent galaxies, necessary to reconcile observations with the most successful cosmological framework.

But what are exactly the mechanisms responsible for shutting down star formation in these massive systems is not clear. Over the years, numerous mechanisms have

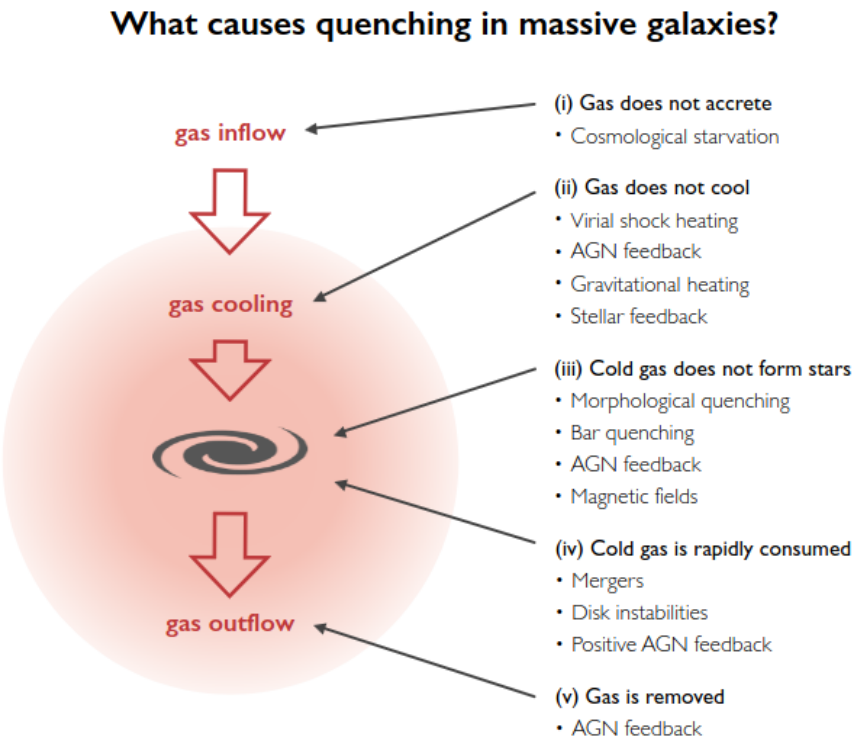

Figure 1.5: *Schematic diagram listing the plausible quenching mechanisms. From Man and Belli (2018).*

been proposed to explain the quenching of massive galaxies, including active galactic nuclei (AGN), stellar feedback, and gravitational effects. A summarizing picture of all proposed quenching mechanisms in the the various stages of gas cycle is illustrated in Figure 1.5: normally, stars form out of molecular gas of temperature T $< 10^2$ K, that cooled and settled from warm and hot gas within the halo (T = 10^3 - 10^6 K) previously accreted from cosmological filaments. Galaxy quenching can be understood as an interruption to any one of the necessary conditions to star formation - of which there are many.

Semi-analytical models and cosmological hydrodynamical simulations are capable of reproducing the basic properties of quiescent galaxies, such as number counts and colours. In all cases, this is made possible by some form of feedback, generally attributed to AGN, that heats up the gas in the halos. This is evidence that AGN feedback may be the most relevant quenching mechanism in massive systems. Even though many AGN feedback mechanisms have been observed at play in massive hosts, we have yet to obtain a direct observational evidence of the effect of AGN activity on the quenching of star formation, particularly at high redshift.

As is clear from Figure 1.5, studying the physical properties of gas in these massive systems is a fundamental step towards understanding star-formation quenching.

1.3 Subject and scope of the thesis

The principal aim of this work is to analyze in detail the rest-frame optical ionized gas emission lines in a sample of massive quiescent galaxies with redshift between 1.7 $<$ z $<$ 3.5 observed in the COSMOS field in order to investigate their current star-forming

activity and shed light on the possible mechanisms responsible for the quenching of star formation in these passive systems.

The spectroscopic data were obtained using MOS (Multi Object Spectroscopy) with the NIRSpec instrument aboard the James Webb Space Telescope, as part of the Blue Jay survey. The observations cover the 1-5 μm wavelength range and were obtained using three different gratings of medium resolution R $\sim$ 1000. The high sensitivity of JWST combined with its very broad, near-IR wavelength range have made it possible to model and fit emission lines that would have been otherwise invisible to any other space-based or earth-based observational facility.

Thanks to the high quality of my data, I am able to spectroscopically fit several optical ionized gas emission lines in these passive systems. From the fitted spectra the SFR and emission line flux ratios of each object are obtained. These results are used to better understand the underlying ionization mechanism behind the lines' production and its implications for the evolutionary history of the galaxy.

In particular, ionized gas line flux ratios are used as a diagnostic tool in several *line diagnostic diagrams*, such as the BPT diagram, after Baldwin et al. (1981): these diagrams take advantage of theoretical models of ISM photoionization to draw a relation between specific line ratios and the fundamental properties of excitation sources inside a given galaxy (Kewley, Nicholls, & Sutherland, 2019), from star formation to AGN and shocks.

Several different diagnostic diagrams are used to classify the ionization source responsible for the production of the observed lines: the final diagnostics produced will show that, according to their optical spectrum, most of the seemingly "normal" galaxies in the sample show signs of actually harbouring a never-observed-before active nucleus. Moreover, in a subsample of cases, broad and asymmetric spectral features in the emission lines are visible: these can be interpreted as the spectral signature of powerful, galaxy-scale outflows of ionized gas, that in absence of bustling star formation activity such as is the case in these passive galaxies, are a strong sign of AGN activity and feedback at work (Fabian, 2012; King & Pounds, 2015).

Chapter 2 will provide a brief introduction to JWST, Chapter 3 will deal with the Blue Jay survey of cosmic-noon galaxies and the selection of the quiescent sample and Chapter 4 will illustrate the algorithm used for the spectral fitting of the lines. Results from the spectral fitting will be discussed and interpreted in Chapter 5 for line ratios diagnostic diagrams, Chapter 6 for the calculation of the star formation rate, and Chapter 7 for the ionized gas outflows. Throughout this work a Λ cold dark matter cosmological model is adopted, with $H_0 = 70$ km s^{-1} Mpc^{-1} , $\Omega_M = 0.3$, and $\Omega_\Lambda = 0.7$.

Chapter 2

The James Webb Space Telescope

The instruments through which data are collected can never be isolated from the physical interpretation of the observational data. Each telescope's capabilities, characteristics, and limitations will always influence the type of science that can be done with it; as a result, in this chapter I will provide a brief introduction to the main facility used in this thesis, which is the James Webb Space Telescope.

Figure 2.1: *JWST in the Northrop Grumman cleanroom following a sunshield deployment test, from G23.*

The James Webb Space Telescope (Gardner et al. (2023, 2006), from now on indicated as G06 and G23) is a large (6.5 m in diameter), cold (<50 K), infrared-optimized observatory with a segmented mirror design, that was launched on December 25, 2021 and is now in science operations. The project was conceived from the beginning as an international one, led by NASA in partnership with the European and Canadian Space Agencies (ESA and CSA).

JWST's revolutionary optics and design enable observations of the distant early universe, potentially reaching beyond redshift z $\sim$ 15, within $\sim$ 300 Myr of the Big Bang (G23). The telescope is equipped with imaging cameras and spectrometers covering the 0.6μm to 28μm wavelength range. No other existing or planned ground- or space-based telescope can obtain comparable observations (G06): Hubble has a collecting area that is 6.25 times smaller and it is not as cold, therefore it emits infrared radiation beyond 1.7μm. Spitzer was just as cold, but had less than 2% of JWST's collecting area. For ground-based facilities, the presence of the Earth's atmosphere results in an infrared background that is 10^6 to 10^7 times higher, with many spectral regions completely blocked from observation (G23).

2.1 Science scope

The James Webb Space Telescope mission was conceived with four main science objectives in mind (G06) in order to trace and investigate cosmic history on every scale, from the birth of the first galaxies to the search for signs of life on other planets.

1. *The End of the Dark Ages: First Light and Reionization.*
   The emergence of the first individual sources of light in the universe marks the end of the "Dark Ages" in cosmic history, a period characterized by the absence of discrete sources of light (Rees, 1997). It is important to understand how these first structures formed, as they influence greatly how the rest of the structures formed after. The first scope that JWST has been set out to is to identify the first luminous sources to ever have been formed and to determine the ionization history of the early Universe.

2. *The Assembly of Galaxies.*
   The second scope of the mission, relevant to the present work, is to investigate in detail all the processes that determined the assembly and evolution of galaxies, from the epoch of reionization to the present day. The mission is going to closely investigate how every part of a galaxy evolves in time, from dark matter, to stars and gas, to metals, to morphological structures and active nuclei.

3. *The Birth of Stars and Protoplanetary Systems.*
   The formation of stars and planets is still a difficult topic to investigate observationally, due to the dust-enshrouded environments in which these phenomena take place. JWST has the capability to reach the most optically-obscured regions and shed light on these topics.

4. *Planetary Systems and the Origins of Life.*
   The last scope of the mission seeks to determine the physical and chemical properties of planetary systems including our own, and investigate the potential for the origins of life in these systems.

2.2 Observatory overview

The JWST observatory was launched from Centre Spatial Guyanais at 12:20 UTC on December 25, 2021 by an Ariane 5 ECA+ rocket. The launch provided a near-perfect

trajectory and burned less on-board fuel than allocated, thus potentially extending the projected 10-year lifetime of the spacecraft up to more than 20 years (G23). All 50 major deployments were successfully completed on 2022 January 8. The observatory performed all midcourse correction maneuvers and achieved its operational 6-month period orbit around the Sun-Earth second Lagrangian point L2: the orbit is inclined slightly with respect to the ecliptic plane and avoids Earth and Moon eclipses of the Sun, ensuring continuous electrical power.

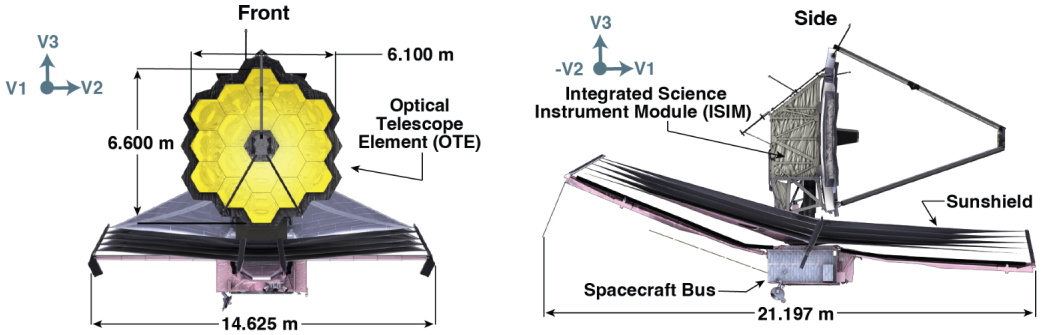

Figure 2.2: *Front (left image) and side (right image) view of the fully deployed JWST observatory, from Menzel et al. (2023)*

The JWST Observatory (Figure 2.2) is comprised of three major elements: the spacecraft bus and sun shield, the Optical Telescope Element (OTE), and the Integrated Science Instrument Module (ISIM) (Lightsey, Atkinson, Clampin, & Feinberg, 2012; Nella et al., 2004).

JWST has 2 distinct thermal regions: the sun-facing 300 K hot side and the 40 K cold side. The spacecraft bus is located on the hot side, while the OTE and ISIM are located on the cold side. The hot and cold sides are separated by a sun shield that intercepts over 200,000 W of radiant energy from the Sun and transmits only about 1 W to the OTE and ISIM. At given time, JWST must maintain a position such as that the OTE and science instruments are always protected from the Sun by the sun shield: this basic constraint determines the telescope's *Field of regard* (FOR), which is the region of the sky where JWST can safely conduct science observations (Menzel et al., 2023). The FOR is defined by the allowed range of boresight pointing angles for the observatory relative to the sun line, which must remain in the range 85° to 135° at all times to keep the telescope behind the sun shield (Figure 2.3). Thus, the FOR is a large torus on the sky that moves roughly 1° per day in ecliptic longitude, following the telescope in its path around the Sun. At any instant, 40% of the sky is visible to the telescope, while over the course of the year the full sky is observable (G06).

2.3 Telescope design

2.3.1 Optical Telescope Element

The Optical Telescope Element (OTE), illustrated in Figure 2.4, is a Tri-Mirror Anastigmat Cassegrain telescope. Its optical configuration consists of an all-reflective four-mirror design in a three-mirror anastigmat configuration (Contreras & Lightsey, 2004;

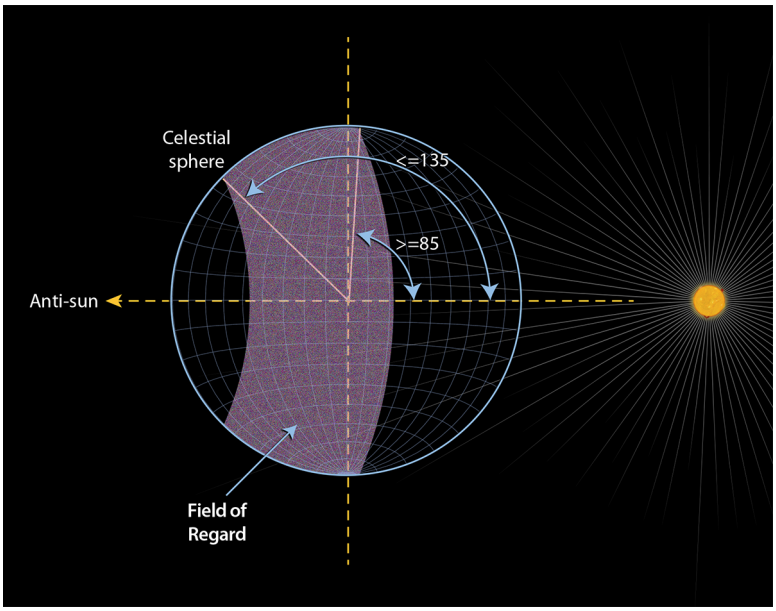

Figure 2.3: *JWST's field of regard. Adapted from: JWST Mission Operations Concept Document.*

Menzel et al., 2023). It contains an elliptical primary mirror made up of 18 hexagonal beryllium primary mirror segment assemblies (PMSAs) (Figure 2.5a), a hyperbolic 0.8m convex secondary mirror, an elliptical tertiary, and an actively controlled fine steering mirror for image stabilization. All the mirrors are coated with gold (G23).

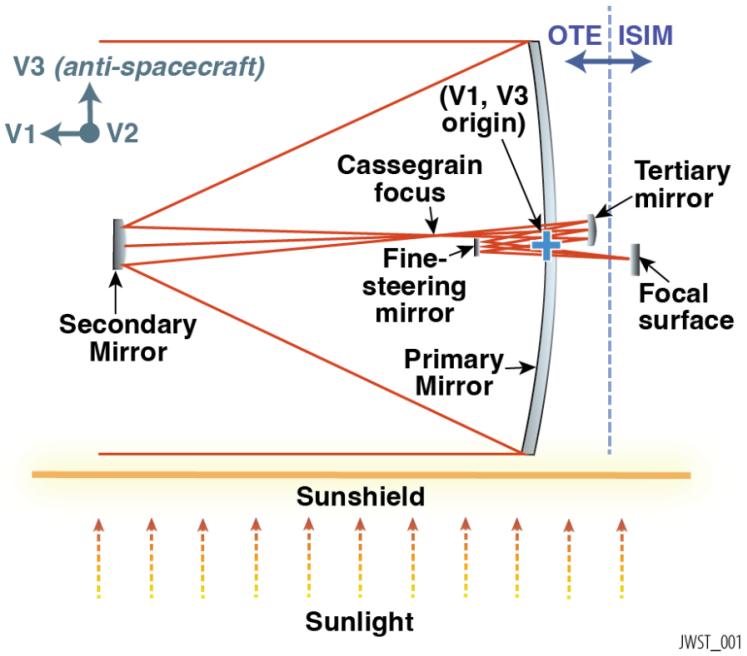

Figure 2.4: *JWST's optical layout. From McElwain et al. (2023)*

The JWST telescope was designed to be stowed in order to fit within the Ariane 5 fairing for launch. Following launch, the observatory needed to be deployed into the operational configuration. Figure 2.5b shows how the 18 primary mirror segments were arranged inside Ariane 5: telescope deployments included separating from the spacecraft bus, driving the secondary mirror into position, rotating and latching the

primary mirror wings into position, and finally deploying the primary mirror segment assemblies and the secondary mirror from their launch locks (Menzel et al., 2023). The telescope alignment used image based sensing and control with the primary mirror segments and secondary mirror (Rigby et al., 2023).

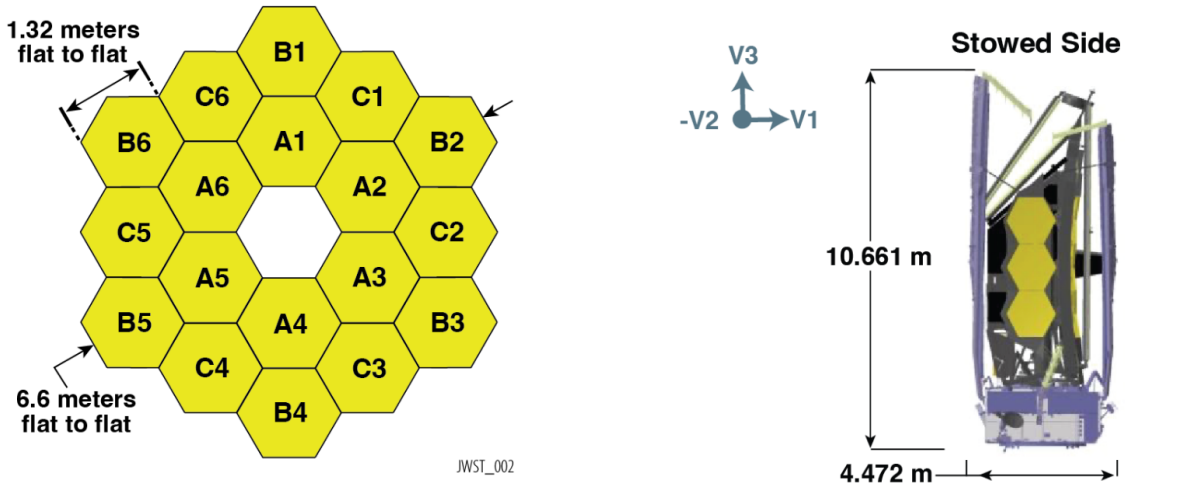

(a) *Primary mirror dimension and prescription. The primary mirror is made up of 18 hexagonal segments, each 1.32 m flat to flat. From G06*

(b) *JWST stowed inside the Ariane 5 fairing, from Menzel et al. (2023)*

Figure 2.5: *The fully deployed (right) and folded (left) primary mirror.*

The total collecting area of the primary mirror is 25.4 m^2, as measured on-orbit using the NIRCam pupil imaging lens, and the instantaneous Field of View is of $\sim$ 9' x 19' (G23). The telescope was designed to be diffraction-limited at $\lambda = 2$ μm wavelength, which can be converted to an equivalent condition of having the rms wave front error less than $\lambda/14$, using the optical Maréchal approximation. During early science operations, the wave front error was measured to be $\sim$ 80 nm RMS: therefore, operationally, the observatory is diffraction limited at $\lambda = 1.1$ μm (Rigby et al., 2023).

2.3.2 Integrated Science Instrument Module

JWST has 4 Science Instruments (SIs) mounted on a common assembly module called the Integrated Science Instrument Module (ISIM), along with the Fine Guidance Sensor (FGS) and the data-handling computer. It also houses the electronics needed for the control and data processing of instrument detectors and the maintenance of the thermal environment. A full view of each SI's field of view and placement on the JWST focal plane is shown in Figure 2.8.

Here is a short list and summary of each Science Instrument's characteristics and observation modes, all adapted from G23.

NIRCam:

The Near InfraRed Camera (Horner & Rieke, 2004; M. J. Rieke et al., 2003, 2023) provides imaging from 0.6μm to 5.0μm in broad-band, medium-band and narrow-band filters. It can also operate in four other science modes: a coronagraphic imaging mode, a

time-series imaging mode for photometric monitoring, a wide field slitless spectroscopy mode between 2.4 - 5.0 μm, and a grism time series for spectroscopic imaging, using a grism with resolving power R $\sim$ 1600 at 4μm. NIRCam is designed with two modules observing parallel fields of view; each module uses a dichroic to observe simultaneously in a short wavelength channel (0.6–2.3 μm) and a long wavelength channel (2.4–5.0 μm). The total field of view is 2.2' $\times$ 4.4'.

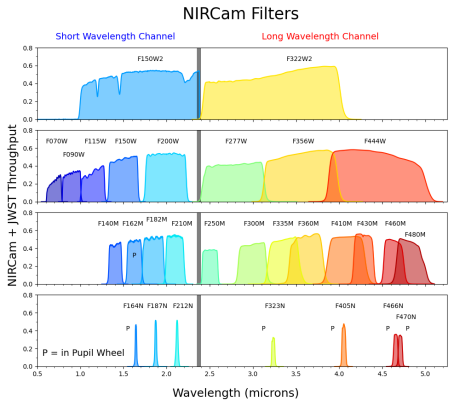

(a) *NIRCam and JWST OTE filter throughputs.*

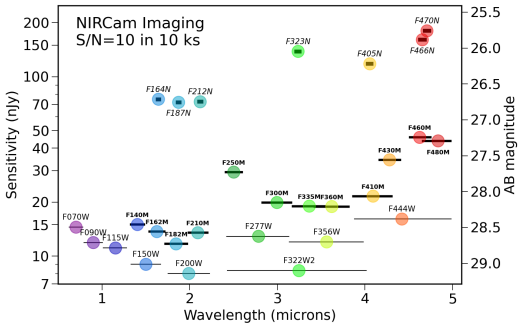

(b) *NIRCam's sensitivity for imaging shown as S/N = 10 detection limits for point sources in a 10 ks image.*

Figure 2.6: *NIRCam's filters and sensitivity, from M. Rieke et al. (2005).*

NIRSpec:

The JWST Near Infrared Spectrograph (Böker et al., 2023; Jakobsen et al., 2022) provides 0.6-5.3 μm spectroscopy at resolving powers of $\sim$100, $\sim$1,000, and $\sim$2,700 in 4 observing modes, using a fixed slits, a Micro Shutter Assembly (MSA) (Ferruit et al., 2022), or an integral field unit (IFU) (Böker et al., 2022). The detector array's pixels are 18μm $\times$ 18μm and project to an average of 0.103" in the dispersion direction and 0.105" in the spatial direction. Dispersion is done with a prism (R = 30 - 300) or gratings (3 gratings at medium resolution R = 500 - 1343 and 3 at high resolution R = 1321 - 3690). The 4 observing modes of NIRSpec are: Multi-Object Spectroscopy (MOS) with the MSA, imaging spectroscopy with the IFU, high contrast single object spectroscopy with the fixed slits and Bright Object Time Series (BTOS) spectroscopy with the NIRSpec wide aperture.

NIRISS:

The Near Infrared Imager and Slitless Spectrograph (Doyon et al., 2012, 2023) provides observing modes for slitless spectroscopy, high-contrast interferometric imaging, and imaging, at wavelengths between 0.6 and 5.0 μm over a 2.2' x 2.2' field of view, matching the FOV of one of the two NIRCam channels. Although NIRISS is packaged with the Fine Guidance Sensor (FGS), the 2 instruments are functionally independent of each other. NIRISS has 4 observing modes: wide field slitless spectroscopy over the entire FOV using 2 grisms, single object slitless spectroscopy with a single grism, aperture masking interferometry (AMI) enabled by specific filters and imaging in a total of 7 wide + 5 medium-band filters.

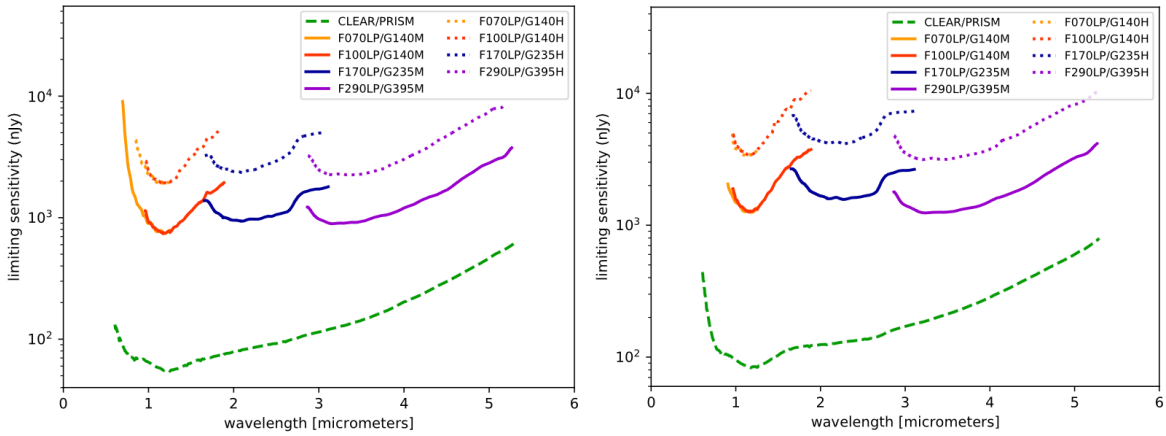

Figure 2.7: *NIRSpec point-source continuum sensitivity in MOS/FS (left) and IFS (right) mode, for the 2 sets of gratings and the prism. From Böker et al. (2023).*

MIRI:

The JWST Mid-Infrared Instrument (G. H. Rieke et al., 2015; Wright et al., 2023, 2015) provides both imaging in broad-band filters and IFU spectroscopy from 5.0μm to 28.0μm. It also has low-resolution slit spectroscopy from 5.0μm to 12.0μm and a coronagraphic capability. The MIRI instrument is actively cooled to an operating temperature of 6.0K with a $\sim$ 6K/18K hybrid mechanical cooler that employs gaseous helium as the coolant.

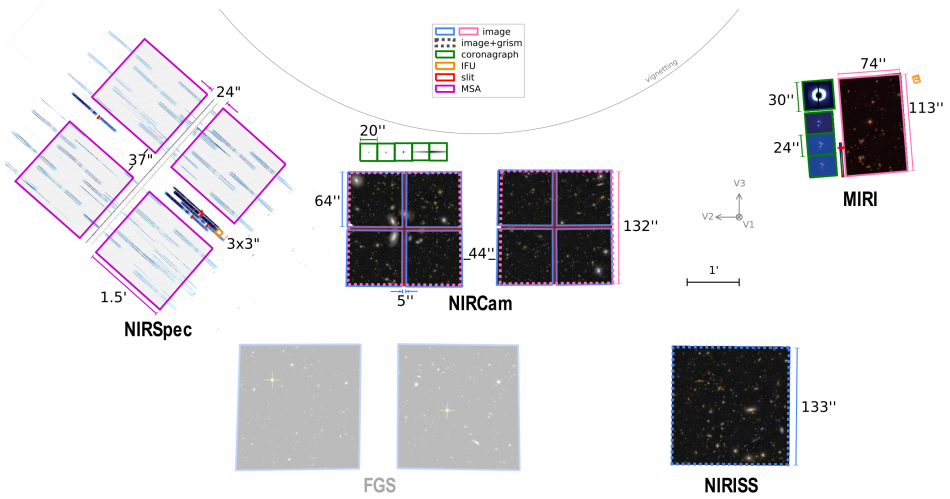

Figure 2.8: *Position of the SIs in the JWST field of view with an example illustration of the type of data that can be obtained. From the JWST User Documentation Guide*

Chapter 3

Data and sample selection

3.1 The Blue Jay survey

The data analyzed in this work are taken from the Blue Jay survey, a medium-sized JWST Cycle-1 observational program (PI: Sirio Belli). This is a deep multi-object spectroscopic survey which observed galaxies in the COSMOS field at redshift between $1.7 < z < 3.5$ (Belli et al. 2023, in preparation).

3.1.1 Parent catalog and target selection

Galaxies observed by the Blue Jay program were selected from observations of the COSMOS field in the F160W filter taken by the Cosmic Assembly Near-Infrared Deep Extragalactic Legacy Survey (CANDELS; Grogin et al., 2011; Koekemoer et al., 2011), a 912-orbit Multi-Cycle HST Treasury imaging program. The parent sample was constructed from the 3D-HST survey's photometric catalogs (Brammer et al., 2012; Momcheva et al., 2016; Skelton et al., 2014), which combine CANDELS and 3D-HST data with photometric ground- and space-based data in a total of 27 broad bands and 17 medium bands from optical to near-infrared.

The first catalog selection uses galaxies with a signal-to-noise ratio in F160W higher than 5 and brighter than $H_{50} = 26.5$ in F160W, to avoid galaxies that are mostly undetected by the CANDELS survey. An important selection criteria is that of stellar mass completeness: this depends on both the redshift and the mass-to-light ratio of the galaxies not observed by the survey. To get a reference mass-to-light ratio, a selection of the least massive half of the galaxies at each redshift was used, in order to represent the true mass-to-light ratio of the low-mass galaxies missing from the catalog. Then, following Pozzetti et al. (2010), a limiting mass was calculated for each galaxy, corresponding to the exact mass it would need to have in order to be observed at exactly 26.5 F160W magnitude (at the same redshift and mass-to-light ratio). This limiting mass is given by:

$$M_{lim} = \log M_* - 0.4(H_{50} - H) \tag{3.1}$$

and the mass completeness level of the sample is defined as the 90th percentile of the M_{lim} function as a function of redshift, which in the case of our redshift limits ($1.7 < z < 3.5$) is well approximated by a linear fit:

$$\log(M./M) = 8.13 + 0.34z. \tag{3.2}$$

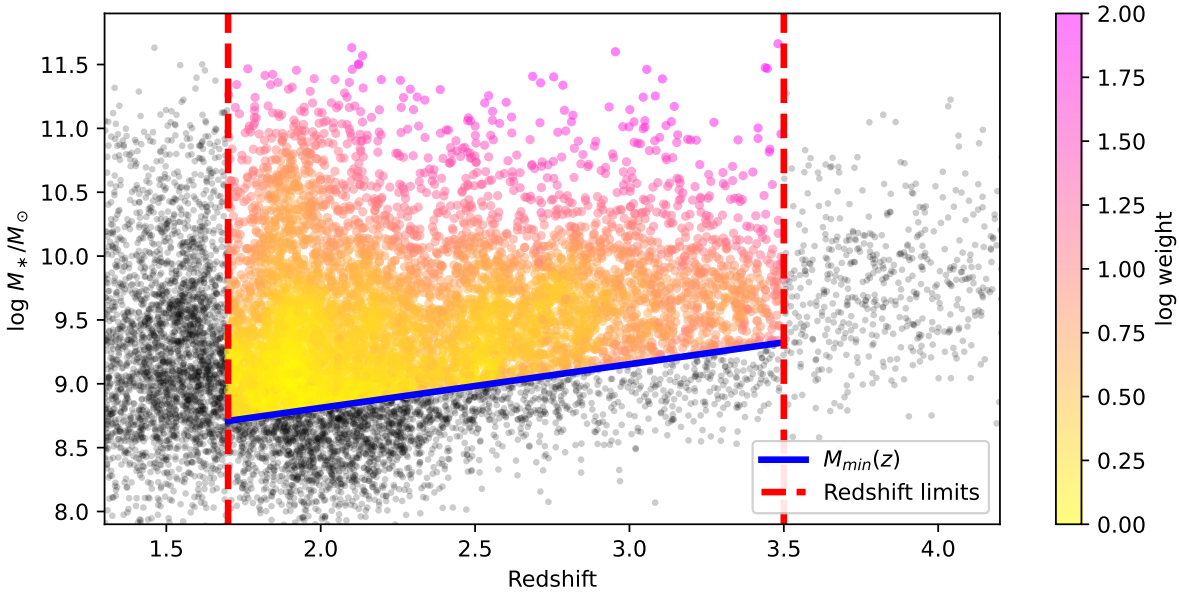

Figure 3.1: *Stellar mass and redshift distribution of the parent catalog: the vertical red dashed lines indicate the targeted spectral range. Each point is colored depending on its assigned spectroscopic weight.*

Finally, a set of spectroscopic weights were assigned to the parent catalog for the final selection, in order to represent the relative probability of being selected for NIRSpec observations of each object. The weight of each galaxy was thus set to be inversely proportional to the local density of stellar masses and redshifts, so as to assign a larger statistical weight to the rarest masses and redshifts in the survey's range. This final selection of the targets yields a truly representative sample for all galaxies more massive than $\sim 10^9 M_\odot$, with a minimal bias at low masses. The resulting mass, redshift and spectroscopic weight distribution of the parent sample is displayed in Figure 3.1.

3.1.2 NIRSpec observational setup

The targets' spectra were taken by NIRSpec in the MOS configuration: NIRSpec's Multi-Object Spectroscopy (MOS) mode provides multiplexed spectroscopy from 0.6 to 5.3 μm over a 3.6' × 3.4' field of view. This mode uses small configurable shutters in the Micro-Shutter Assembly (MSA) to capture many astronomical sources' spectra within a single exposure. The MSA is equipped with ∼ 250 000 micro-shutters of size 0.20" x 0.46" distributed onto 4 quadrants and mounted on a fixed support grid over 2 detector arrays (Ferruit et al., 2022). A schematic illustration of the MSA setup is represented in Figure 3.2.

The small size of individual NIRSpec MSA shutters means that the survey design requires high-quality astrometry of the parent catalog in order to correctly place the sources inside the Micro Shutter Assembly. To overcome this, the astrometric measurements on the parent sample were taken from the 3D-DASH survey's mosaic based on Gaia astrometry (Mowla et al., 2022), which includes the same data from CANDELS.

The NIRSpec observations were divided into 2 different MSA pointings, a North one targeting 74 galaxies and a South one targeting 77, for a total of 151 objects. They were performed with the G140M/F100LP, G235M/F170LP and G395M/F290LP medium-resolution gratings (R ∼ 1000) in order to obtain an almost countinuous wavelength coverage from 1 to 5 μm for all galaxies.

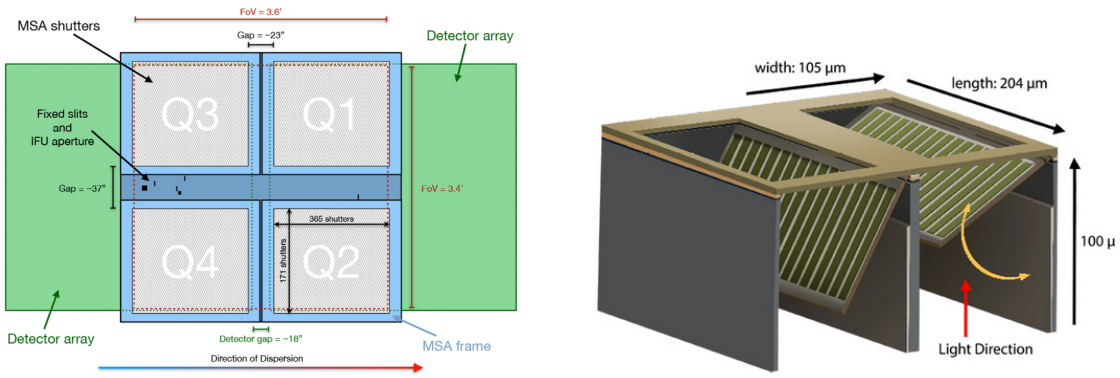

Figure 3.2: *An illustration of the MSA layout in the NIRSpec aperture plane (left) and a cut-away view of 2 micro-shutters of the MSA. From Ferruit et al. (2022).*

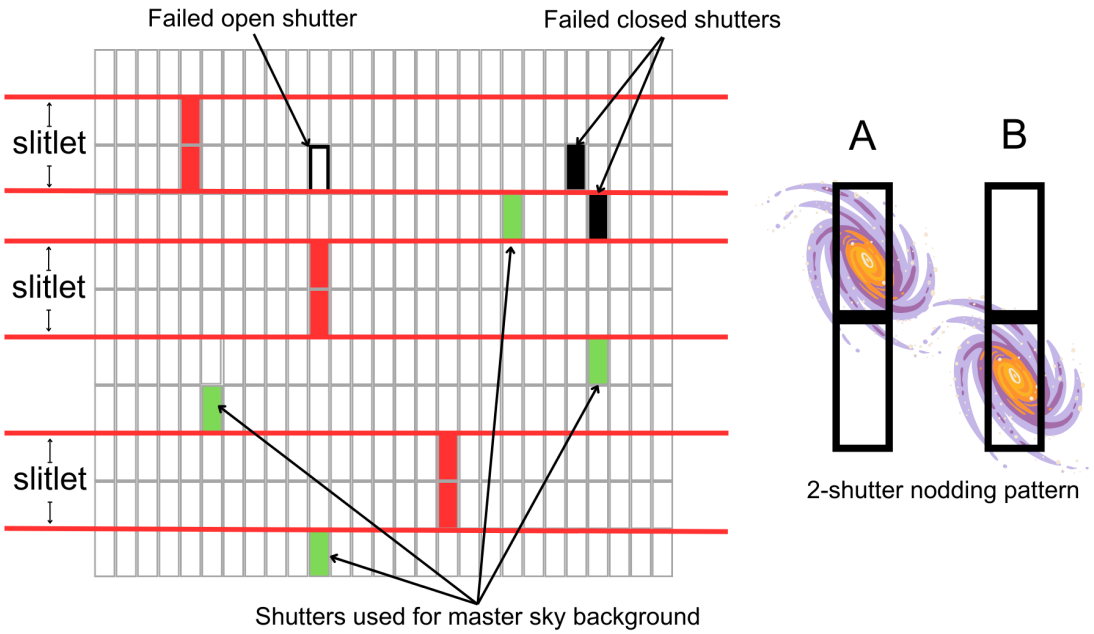

Figure 3.3: *Scheme of the MSA nodding strategy used in Blue Jay: a 2-shutter MSA slitlet configuration is opened on each science target (left), in which 2 adjacent shutters are treated as a unified dither. The telescope executes nods to place the targets within each of the 2 shutters in a slitlet with successive exposures (right), while the background is extracted from other open shutters on the array.*

Grating/Filter	Integrations /exposure	t_{exposure}	Dithering pattern	N_{exposure}	t_{total}
G140M/F100LP	4	97.2 min	$AA'BB'AA'BB'$	8	778 min
G235M/F170LP	2	48.6 min	$AA'BB'$	4	194 min
G395M/F290LP	1	24.3 min	$AA'BB'$	4	97 min

Table 3.1: *Summary of NIRSpec exposures, adapted from Belli et al. 2023 (in preparation).*

The MSA apertures were designed as 2-shutter slitlets and were observed with a nodding pattern, a data acquisition technique in which the telescope is repositioned slightly between exposures to place the target in a different open shutter within the same slitlet. This produces independent measurements of the same source than can be combined to increase signal-to-noise ratio and also enable direct background subtraction: this technique, however, works best with point-like sources.

Since the median size of the primary targets is 0.27 arcsec, comparable to the size of a micro shutter, the standard 3-shutter nodding pattern is not applicable, as most targets partly fill more than one shutter. Thus, a 2-shutter nodding pattern was preferred, although one in which the contributions from the 2 adjacent shutters are treated as a unified dither and summed together, while the background subtraction is done using a master sky background obtained from empty shutters, forgoing the direct background subtraction offered by the nodding pattern. Furthermore, a 2-point dithering pattern along the wavelength direction was employed in order to improve the pixel sampling in the coordinated parallel NIRCam observations. A summary scheme of the nodding and master sky background pattern used is illustrated in Figure 3.3.

The sources were observed by integrating 20 groups in NRSIRS2 readout mode, with a total integration time of between ∼1 h 30 m and ∼13 hours per grating for each MSA pointing (see Table 3.1).

3.1.3 NIRCam coordinated parallel observations

JWST's NIRCam instrument has the possibility to simultaneously operate in coordinated parallel observation mode with the primary observations of NIRSpec, with each instrument viewing a different area of the JWST focal plane. During the primary Blue Jay observations with NIRSpec, parallel NIRCam images were also obtained. With a careful positioning of the two NIRSpec pointings, it was possible to get an area of overlap between spectroscopic and imaging data, as shown in Figure 3.4. NIRCam is capable of observing a 9.7 arcmin^2 field of view simultaneously in a short wavelength channel ($0.6 - 2.3\mu m$) and long wavelength channel ($2.4 - 5.0\mu m$) with a number of wide, medium and narrow filters. NIRCam was used in imaging mode with the filters listed in Table 3.2, for a total parallel observation time of 33.6 hours. The summary of NIRCam parallel observations is found in the same table. This work does not, however, make use of the NIRCam data but only of the spectroscopic data.

Filter	Total integrations	t_{total}
F090W	4	92 min
F115W	8	184 min
F150W	16	368 min
F200W	16	368 min
F277W	12	276 min
F356W	16	368 min
F444W	16	368 min

Table 3.2: *Summary of NIRCam observations and filters used*

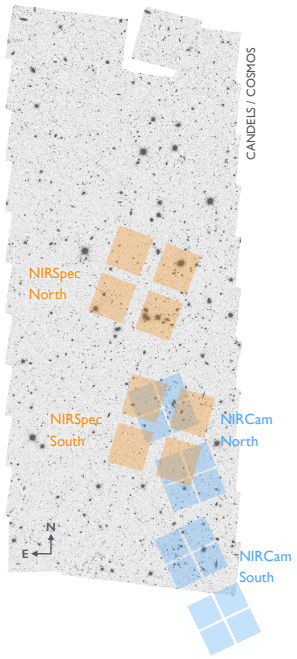

Figure 3.4: *NIRSpec and NIRCam pointings mapped onto the COSMOS field*

3.2 Data reduction and flux calibration

The spectral data reduction was carried out using the JWST pipeline and will be explained in more detail in Belli et al. 2023 (in preparation).

Since the MSA shutters cover only a fraction the targets' angular size (Figure 3.5), the flux must be corrected for the inevitable *slit losses*. In order to more accurately calibrate the JWST spectra, models of the stellar continuum for each galaxies were used. The continuum fits were done using the Bayesian code `Prospector` (Johnson, Leja, Conroy, & Speagle, 2021), following the approach explained in Park et al. (2023) and Tacchella et al. (2022). Blue Jay's catalog continuum fitting procedure and results are explained in more details in Park et al., 2023 (in preparation) and Belli et al. (2023), and will be briefly explored in the next chapter of this work.

A single `Prospector` stellar continuum model was fitted both to the 1D NIRSpec spectrum and the multi-wavelength photometry data of each target. During the fit, a polynomial distortion was applied to the spectrum in order to match it with the photometric information obtained for each target from JWST'S MIRI and NIRCam data, as well as archival photometric data from HST, obtained by the ACS and WFC3 instrument. Assuming that the emission probed by the MSA shutters is only a scaled down version of the total emission coming from the whole galaxy, i.e., ignoring eventual gradients that could be present across the target's angular extension, this method of slit loss correction yields an accurate flux calibration for the NIRSpec data.

An example of the flux calibration's fitting procedure can be seen in Figure 3.6, taken from the Belli et al. (2023) study of COSMOS-11142, one of the sources observed by the Blue Jay survey.

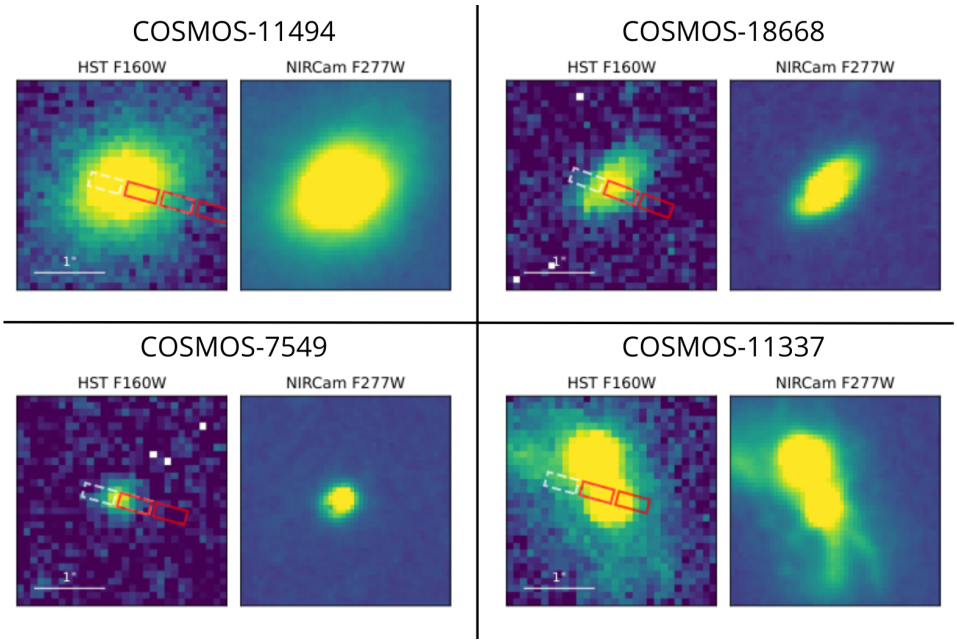

Figure 3.5: *Examples of 4 sources in my sample and their respective MSA shutter positioning. Left panels: F160W filter HST imaging from 3D-HST (Brammer et al., 2012); right panels: F277W filter JWST's NIRCam images, from the PRIMER Treasury Program (Dunlop et al., 2021).*

3.3 Sample selection

3.3.1 Selection criteria

Present-day galaxies exhibit a fundamental bimodality in their SFR distribution, which divides the quiescent galaxy population from the actively star forming one; (e.g. Balogh et al., 2004; Blanton & Moustakas, 2009; Hogg et al., 2004; Kauffmann et al., 2003) and this bi-modality persists out to high redshift (e.g. Bell et al., 2004; Brammer et al., 2009; Taylor et al., 2009; Williams, Quadri, Franx, van Dokkum, & Labbé, 2009). This bimodality is also found in the distibution of some fundamental observational quantities such as *photometric colors*, for example, that can be used as an effective classification tool.

Colors are one of the simplest ways to classify galaxies, since they only require measurements of the integrated flux and are available even when spectra and photometric SEDs are not. Colors alone, however, can be highly degenerate and not reliable for selection: generally, quiescent galaxies have the reddest colours due to their older stellar population, while SF galaxies are bluer due to the presence of young, massive stars in sites of active star formation. But the effects of dust extinction and deep metal absorption lines in stellar atmospheres can significantly redden the intrinsically blue SEDs of very dusty or high metallicity SF galaxies, disguising them as proper "red and dead" quiescent ones (see Cimatti, Fraternali, and Nipoti (2019) for a complete review on galaxy classification). This degeneration worsens when dealing with high-z populations, where the fraction of very dusty star-forming galaxies increases with respect to the present-day Universe (Labbé et al., 2005).

This is why the standard way to select galaxies is done by using color-color selection diagrams, where two different color indices are both taken into consideration. In particular, the rest-frame $U - V$ and $V - J$ colors have been used as selection crite-

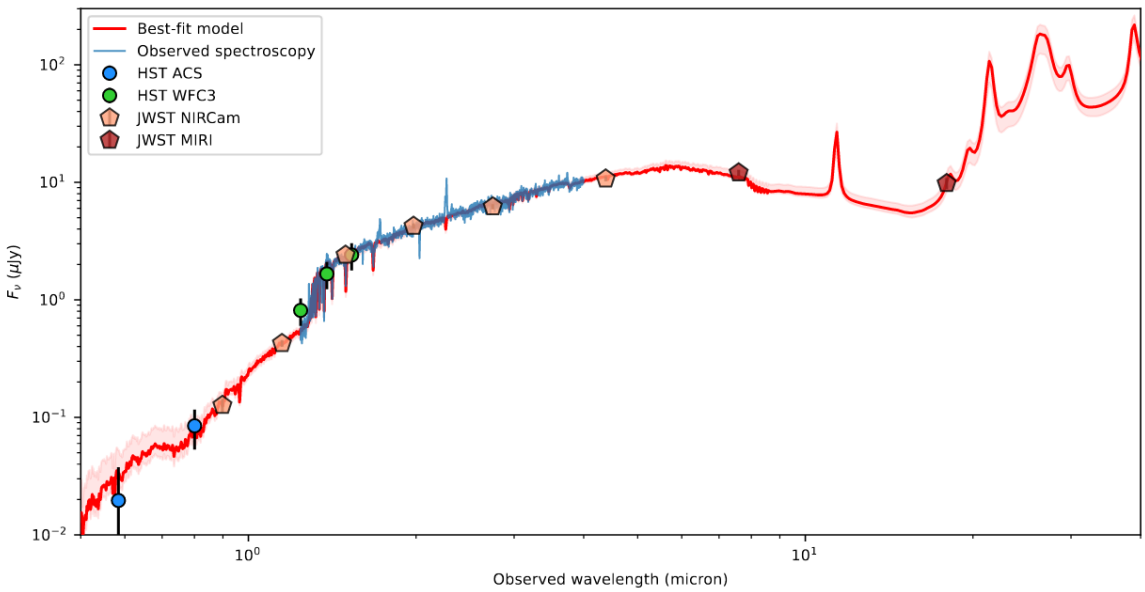

Figure 3.6: *Best-fit model of the stellar continuum by Prospector for COSMOS-11142, fitted to both spectroscopic (blue plot) and photometric data (scatter points).*

ria in the so-called UVJ diagram: in Williams et al. (2009), a bimodality in the plot clearly emerges for galaxies up to z=2, with SF galaxies forming a diagonal track and quiescent galaxies confining themselves to the upper-left part of the diagram. It has been later demonstrated by Whitaker et al. (2011) and Straatman et al. (2016) that this separation extends up to redshift z=3.5 (see Figure 3.7).

The UVJ diagram is an effective tool for the selection of quiescent galaxies, because it allows the dust-age degeneracy between red star-forming and red quiescent galaxies to be broken: both types are red in the $U-V$ color index, but only dust-free, intrinsically red quiescent galaxies are blue in the $V-J$ index. However, some literature exists as well that discourages the reliability on exclusively UVJ colors for the correct classification of galaxies: ad example, Leja, Tacchella, and Conroy (2019) and Antwi-Danso et al. (2023) propose alternative color indices as a way to refine the pure UVJ selection. For this work, I used only the UVJ diagram as a classification tool: the actual effectiveness of my initial selection will be discussed in later chapters.

3.3.2 Quiescent population selection

The first step of my work consists in the selection of my subsample of interest from the whole Blue Jay survey catalog: in particular, the main targets of this thesis' work are quiescent galaxies that have already concluded most, if not all, of their star formation process. The objects observed by NIRSpec are 151: from this first catalog, 4 objects were discarded as they are "filler" galaxies at z $\sim$ 6-7. Thus, the complete Blue Jay catalog is composed of 147 galaxies.

Since I am interested in the mechanisms that brought upon the quenching of the star formation in these systems, I am considering both the typical "red and dead" quiescent galaxy population, characterized by very old stellar population and quite red continuum, as well as the more ambiguous population of "just quenched" galaxies: these are systems that have relatively recently exited their most intense star-forming

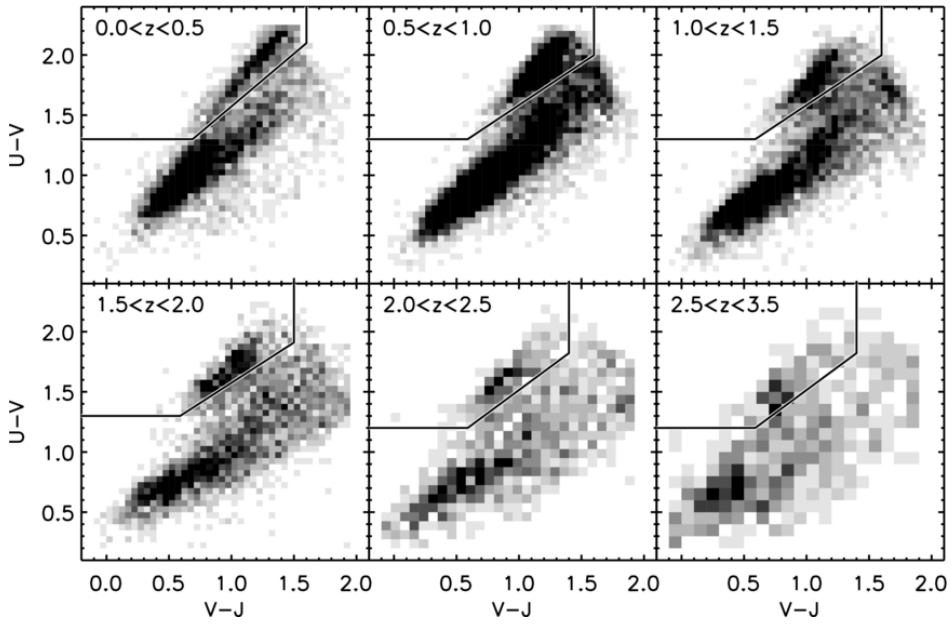

Figure 3.7: *Rest-frame UVJ bimodality for a galaxies in 6 different redshift bins, taken from Whitaker et al. (2011). The gray scale represents the density of points, with the lines indicating the separation between quiescent "red sequence" galaxies and star-forming galaxies. A clear division is visible up to the highest redshift interval $2.5 < z < 3.5$.*

era. The scope of including these objects in my sample is to be able to observe the immediate post-SF transition of these galaxies to the proper quiescent state, in order to, hopefully, directly observe signs of still-active quenching mechanisms in the emission lines (such as outflows, for example).

The sample is selected using the galaxies' U-V and V-J rest frame colors (see Figure 3.8) following Muzzin et al. (2013)'s selection criteria: quiescent galaxies are defined by

$$U - J > 1.3, V - J < 1.5, \quad \text{(all redshifts)} \tag{3.3}$$
$$U - V > (V - J) \cdot 0.88 + 0.69, \quad (0.0 < z < 1.0) \tag{3.4}$$
$$U - V > (V - J) \cdot 0.88 + 0.59, \quad (1.0 < z < 4.0). \tag{3.5}$$

All of the quiescent galaxies in the survey are found at redshift higher than 1 and selected in two consecutive steps:

1. First, I selected the "purely quiescent" population made up of the galaxies which fall entirely inside of the red solid line in Figure 3.9, i.e. those that fully adhere to the selection criteria in Muzzin et al. (2013). This selects a subsample of **18 out of 147** galaxies.

2. Subsequently, I relaxed the selection criteria in order to include the bordering, "just quenched" galaxies: these should be systems that are at the transition point between SF and quiescent and thus are extremely interesting from the point of view of their evolution. These galaxies were selecting by changing the selection criteria to:
$$U - V > (V - J) \cdot 0.88 + 0.49, \tag{3.6}$$
traced by the dashed red line in Figure 3.9.

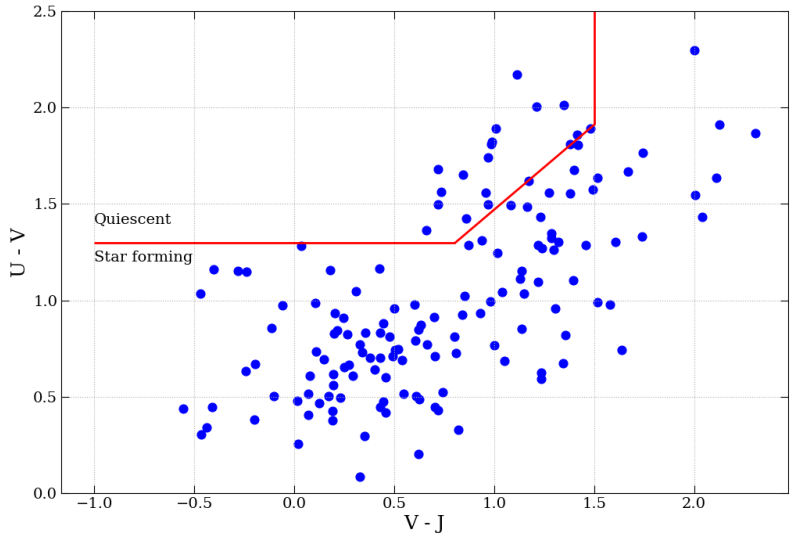

Figure 3.8: *UVJ diagram of all sources in the Blue Jay catalog. In red, the selection criteria from Muzzin et al. (2013).*

The final selected sample is shown in Figure 3.9.

The final sample of galaxies, with the addition of these transitional systems, is of **23 galaxies** out of 147 in the parent catalog. Most of the selected galaxies are found grouped in the central part of the plot, just above the red dividing line: only one galaxy, indicated by the arrow, is dislocated with respect to the others. This particular systems, COSMOS-12175, is a low-mass outlier and is eliminated from the sample through the next selection step.

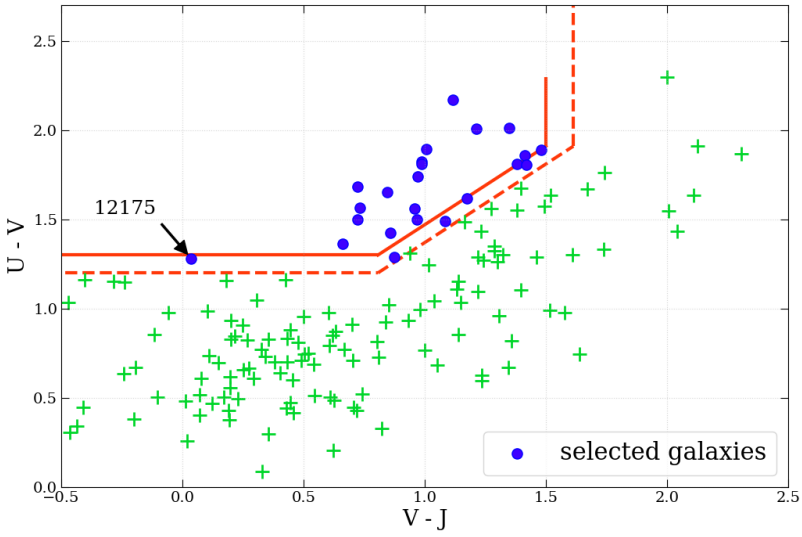

Figure 3.9: *UVJ color selection of quiescent galaxies*

3.3.3 Stellar mass distribution of the sample

I further refine the sample selection by taking into consideration the stellar mass of the selected galaxies: as already illustrated in section 3.1, the Blue Jay survey's targets were selected in such a way to obtain a parent catalog which is complete in stellar mass for every redshift (Figure 3.1). In Figure 3.10, we can see the mass distribution of observed targets on the UVJ diagram: I divided the catalog in *high-mass* galaxies, i.e. galaxies with stellar mass $M_* > 10^{10} M_\odot$, and *low-mass* galaxies, with $M_* < 10^{10} M_\odot$. From the whole *Blue Jay* catalog, the high-mass systems are **74** out of 147. Of these 74, **22** are selected as "quiescent" by the UVJ diagram. This means that most of the galaxies in my sample are massive systems, with $M_* > 10^{10} M_\odot$.

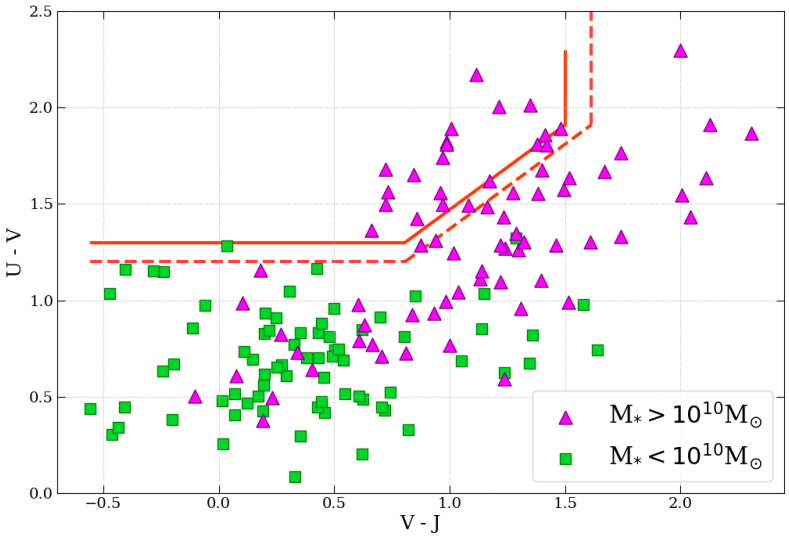

Figure 3.10: *Stellar mass distribution on the UVJ diagram: high-mass galaxies ($M_* > 10^{10} M_\odot$) mainly occupy the upper right part of the plot.*

By taking into consideration the target's stellar mass, I can improve the purity of the first sample selection: as we can see from Figure 3.11, most of the UVJ-selected quiescent galaxies from the first selection are indeed high-mass galaxies. There is only one notable exception of an object with stellar mass $< 10^{10} M_\odot$, COSMOS-12175, which is also the UVJ selection outlier highlighted in figure 3.9. Since I am interested in studying the evolution of massive quiescent galaxies, I have decided to eliminated this system from my sample.

3.4 Final selected sample

From the UVJ color-based selection described in the previous sections, I select **22 out of 147** systems: as an example, 5 of these spectra are plotted in Figure 3.12.
The sample's spectra are generally very long, extending almost uninterrupted from $\sim 1\mu$m to $\sim 5\mu$m: the shape of the continuum is typical of quiescent galaxies and many absorption lines are present. Some gaps in the spectra are visible, in correspondence to the gap between the two detector arrays and some bad pixels are still present

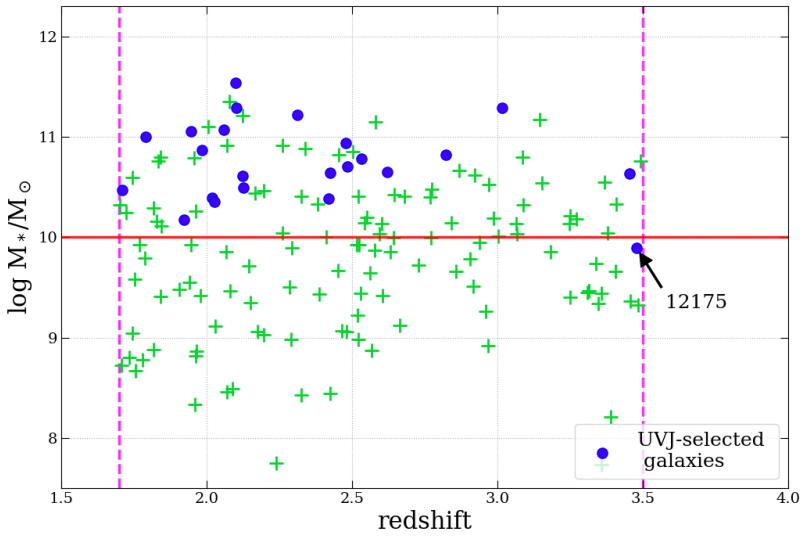

Figure 3.11: *Plot of the stellar mass vs redshift of Blue Jay sources: in blue circles, the galaxies selected as quiescent by my UVJ-based selection, in green crosses the rest. The red horizontal line marks the $10^{10} M_{\odot}$ stellar mass limit, the magenta dashed vertical lines mark the Blue Jay targets redshift bin (1.7<z<3.5).*

even after the data reduction: these, however, do not pose a particular problem to the spectral fitting.

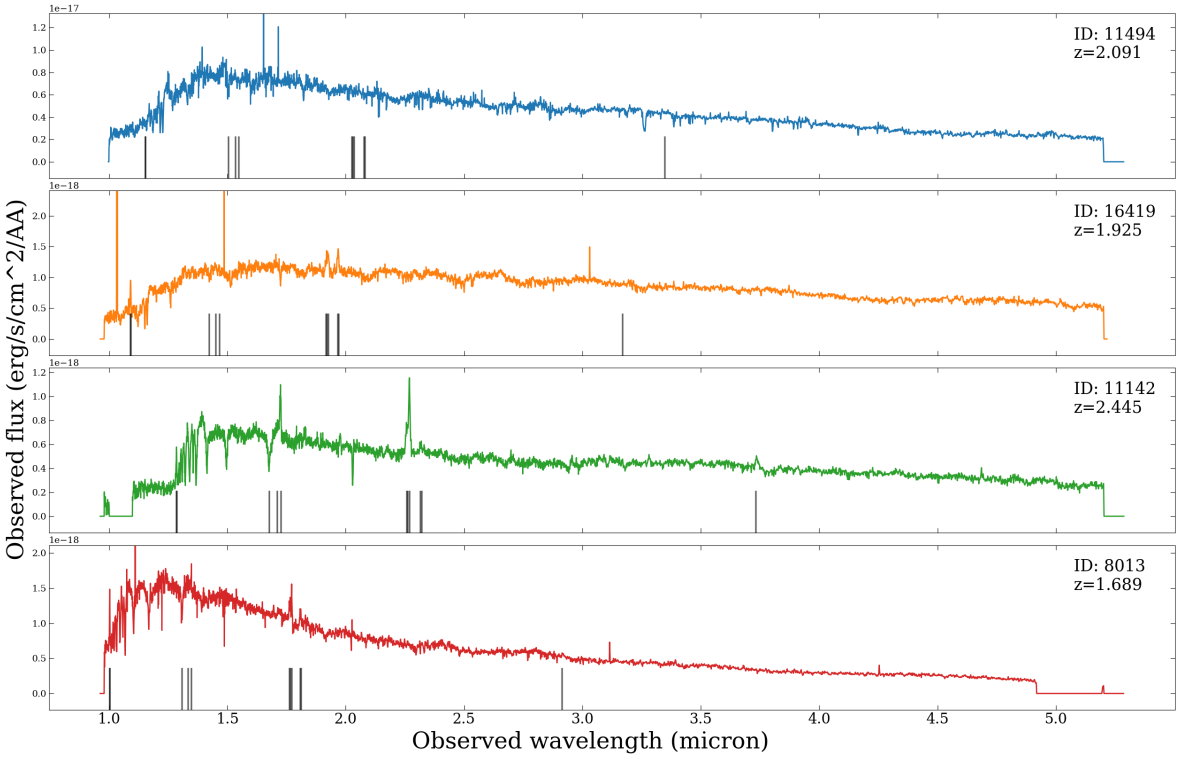

Figure 3.12: *Spectra of 4 sources observed by JWST/NIRSpec in my sample: the observed flux has not been calibrated for slit loss and numerous bad pixels are visible. In black, the galaxy-frame wavelength of fitted emission lines, from left to right: [OII]3727,3729 doublet; Hβ; [OIII]4959,5007 ;[NII] doublet and Hα, [SII]6716,6731 and He I*

Chapter 4

Emission line measurements

The aim of this work is to investigate the ionized gas content of quiescent galaxies at $z \sim 2$ through their rest-frame optical emission line. Through the study of emission lines in a galaxy's spectrum, it is possible to unlock a plethora of knowledge about the chemical abundance, dust content, electron density and temperature of the ionized gas that produced them. Furthermore, rest-frame optical spectra can reveal a galaxy's rate of star formation, as well as whether it hosts an actively feeding supermassive black hole in its center; they can reveal the presence of massive outflows and galactic-scale winds, investigate the velocity, density and mechanical energy of shocked gas and help us understand the dominant power source behind the galaxy's radiation field (see Kewley et al. (2019) for a complete review of what we can learn from emission lines in galaxy spectra).

But first, in order to extract this information from the spectra, I must be able to fit the emission lines in the sample and accurately measure them.

4.1 Fitting the stellar continuum with Prospector

The first step in the emission line measurements procedure is to isolate the observed emission which is only due to *gas* in each spectrum: this can be done by subtracting the emission due to stars and dust from the total observed flux. In turn, this can only be done by fitting the underlying stellar continuum in each galaxy.

The stellar continuum emission was modeled and fitted for each object in the Blue Jay sample using `Prospector` (Johnson et al., 2021), a fully Bayesian stellar population inference code. This code adopts the stellar population synthesis model `FSPS` (Conroy, Gunn, & White, 2009) and a set of free parameters (e.g., redshift, stellar mass, metallicity, dust parameters and star formation history) to generate a synthetic galactic spectral energy distribution which can then be fitted to the observations.
In this case, the `Prospector` code was used to fit both spectroscopic and photometric data (as described in the previous chapter) and only stars + dust contribution were considered, in order to isolate gas emission. For the spectroscopic data fitting, bad pixels and emission lines were masked out. The detailed procedure for continuum-fitting was done following Park et al. (2023) and will be explained in more detail in Park et al., 2023 (in preparation).

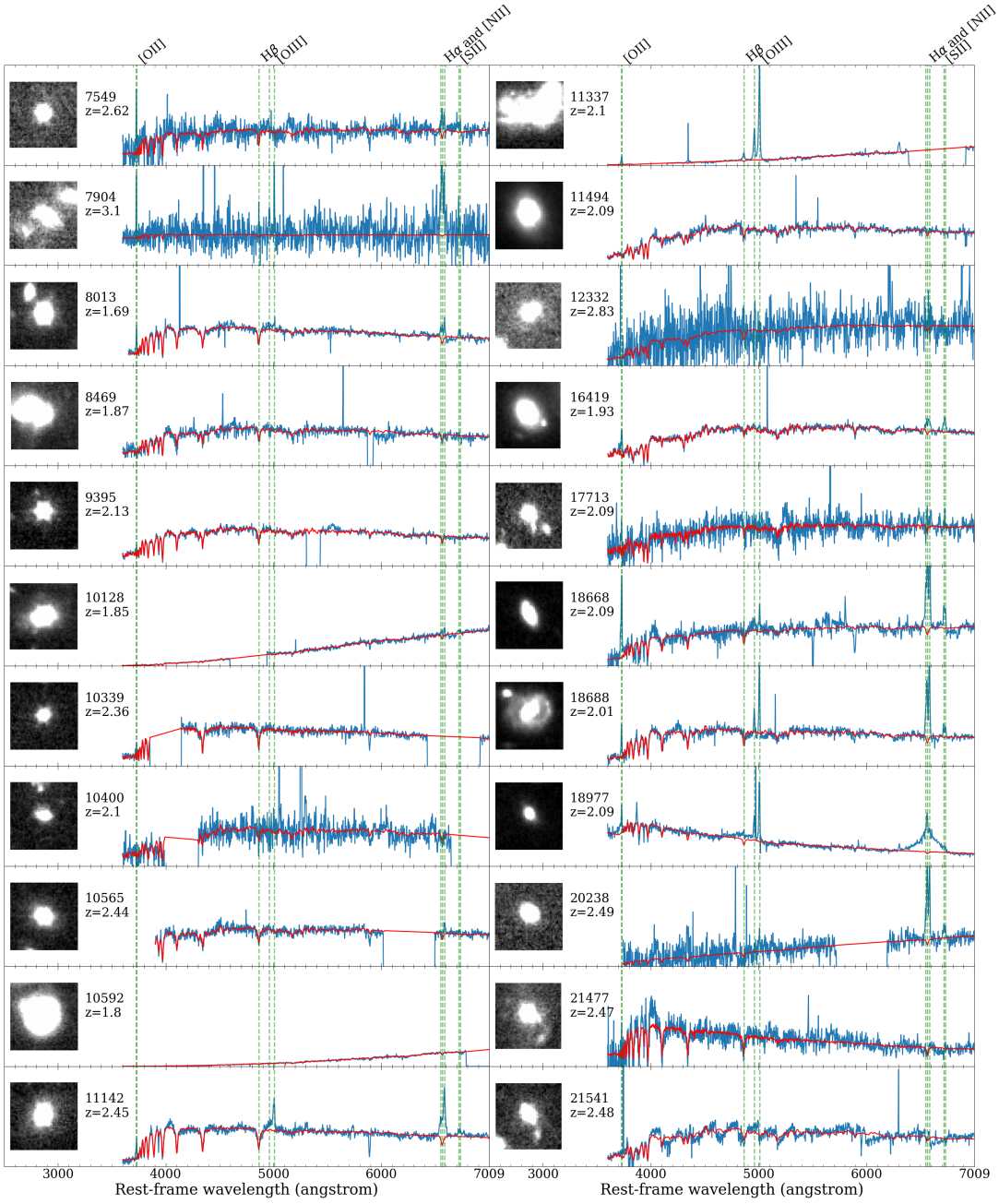

Figure 4.1: *Rest-frame observed spectra (blue plots) with Prospector fits (red overlay) of the sample, zoomed in up to λ=7000 Å, and 3" x 3" cutouts of F277W NIRCam's imaging data from PRIMER (Dunlop et al., 2021). Numerous bad pixels are visible.*

4.1.1 Final sample of continuum-fitted spectra

The spectral sample used in this work has been continuum-fitted with Prospector and flux-calibrated for slit loss. The UVJ-selected sample, discussed in the previous chapter, includes **22** quiescent galaxies with 1D spectra covering the rest frame 3000 to 14000 Å wavelength range. Each galaxy's has an estimated spectral redshift, dust content, stellar mass and age estimated by the stellar population synthesis fit done with `Prospector`.

The full sample's observed spectra, along with their respective Prospector fits, are plotted in Figure 4.1: in order to better highlight the deep absorption lines present in the spectra of these quiescent galaxies, I plotted a cropped version of the data (up to a rest-frame wavelength of 7000 Å). Next to the spectroscopic data, I also added a 3" x 3" cutout of each galaxy: these imaging data are taken from the public JWST Treasury Program (PRIMER - Public Release IMaging for Extragalactic Research; Dunlop et al., 2021) observations of the HST CANDELS COSMOS field. PRIMER obtained deep JWST imaging in 10 bands: F090W, F115W, F150W, F200W, F277W, F356W, F444W and F410M with NIRCam, and F770W and F1800W with MIRI. In particular, for the cutouts in Figure 4.1 I used only the imaging data taken in the F277W NIRCam's filter.

4.2 Spectral fitting

The spectral fitting of the emission lines was structured in the following way: first, in order to isolate the emission due only to the gas, each galaxy's spectrum was continuum-subtracted using the results of the `Prospector` fit. Once the continuum is subtracted, I searched for the brightest emission lines from ionized gas that could be present (an example in Figure 4.2): I find that several of them are visible in most of the spectra with a SNR > 3. In the case of no detection (SNR$<$3), only upper limits were estimated.

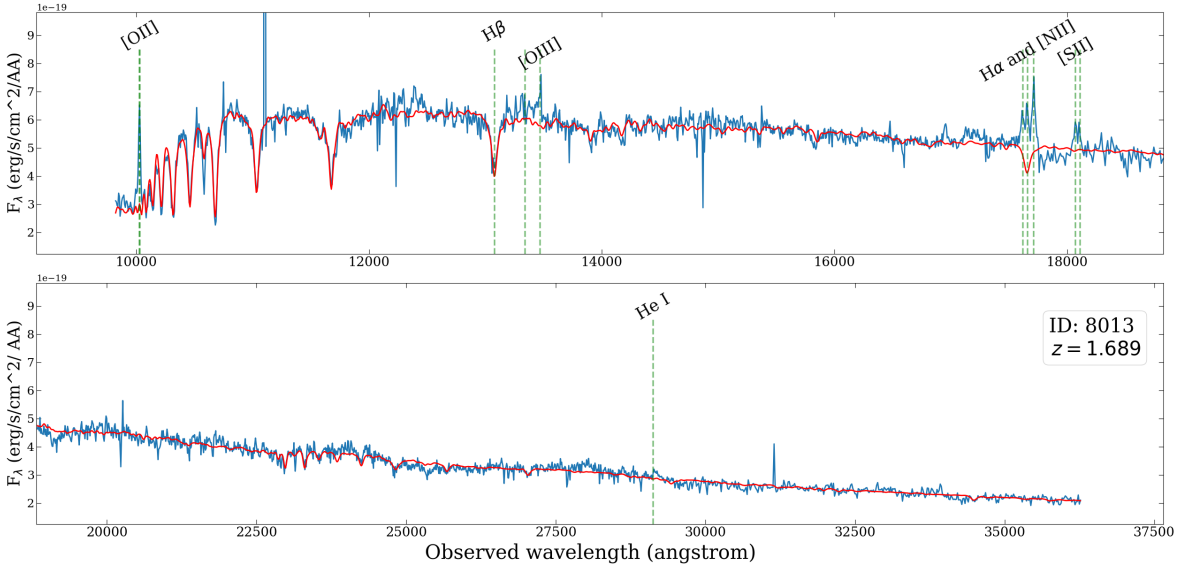

Figure 4.2: *Observed (blue plot) spectrum of COSMOS-8013. In green dashed, the observed-frame location of the emission lines. In red overlay, the prospector fit.*

The ionized gas emission lines relevant for this work (i.e., from $\lambda_{\rm rest} = 0.2$ μm to

$\lambda_{\rm rest} = 2\mu$m) and that we can detect for at least a subset of quiescent galaxies are summarized in Table 4.1.

The emission lines were fitted using Gaussian profiles with the help of the `specutils` (Earl et al., 2023) Python3 library. This library makes use of `astropy.fitting`[1] as a base for the fitting algorithm, which is based on the least-squares minimization `MPFIT` routine (Markwardt, 2009).

4.2.1 Fitting algorithm

The fitting script proceeds as follows: first, the rest-frame wavelength of the lines is shifted to the observed one by multiplying by (1+z), where the galaxy's redshift is estimated from continuum absorption lines by Prospector.
Then, the lines are grouped into 5 separate spectral regions depending on their closeness in wavelength:

1. the [OII]$\lambda\lambda$3727,3729 doublet
2. Hβ and [OIII]$\lambda\lambda$4959,5007
3. Hα and [NII]$\lambda\lambda$6548,6583
4. the [SII]$\lambda\lambda$6716,6731 doublet,
5. and finally the He I λ10830 line.

I then fitt all the lines in a single spectral region using simple Gaussian profiles: following the procedure used in Calabrò et al. (2023), I first identify and fit the highest-SNR line in the spectrum (usually the [OII] doublet or Hα), which gives me a measure of the flux, the centroid and velocity dispersion σ of the easiest-to-fit line. From the centroid's position, I correct the initial estimation of the redshift for the system, which was previously given by the Prospector fit and adjust the other emission lines' centroids position accordingly. Then I proceed to fit all other lines in each spectral region. For each fitting model, the following constraints were imposed, in order to obtain a more robust measurement for low-SNR lines:

[1] GitHub repository: https://github.com/astropy

Ion	$\lambda_{\rm rest}$ **(Å)**
[OII]	3727.10, 3729.86
Hβ	4862.71
[OIII]	4960.30, 5008.24
[NII]	6549.86, 6585.27
Hα	6564.60
[SII]	6718.29, 6732.67
He I	10833.30

Table 4.1: *Table with the list of optical line transitions (in vacuum) that are detected in emission in my sample and that are considered in this work.*

(i) the velocity dispersion σ of each line is fixed to the value found for the highest-SNR;

(ii) wavelength ratios between the lines' centroids are fixed to be equal to the laboratory reference ones and

(iii) the flux ratio between [OIII]5007/[OIII]4959 and [NII]6581/[NII]6548 were fixed at the theoretical value 3:1, following Osterbrock (1989).

From this spectral fitting, we get the flux, wavelength and width of each emission line. An example plot of the fitting results can be seen in Figure 4.3. In order to compare the results of my quiescent sample to the rest of the Blue Jay sample, I have repeated the same fitting procedure on the same set of lines also in the star-forming sample: these results will be useful for the analysis carried out in the next chapter.

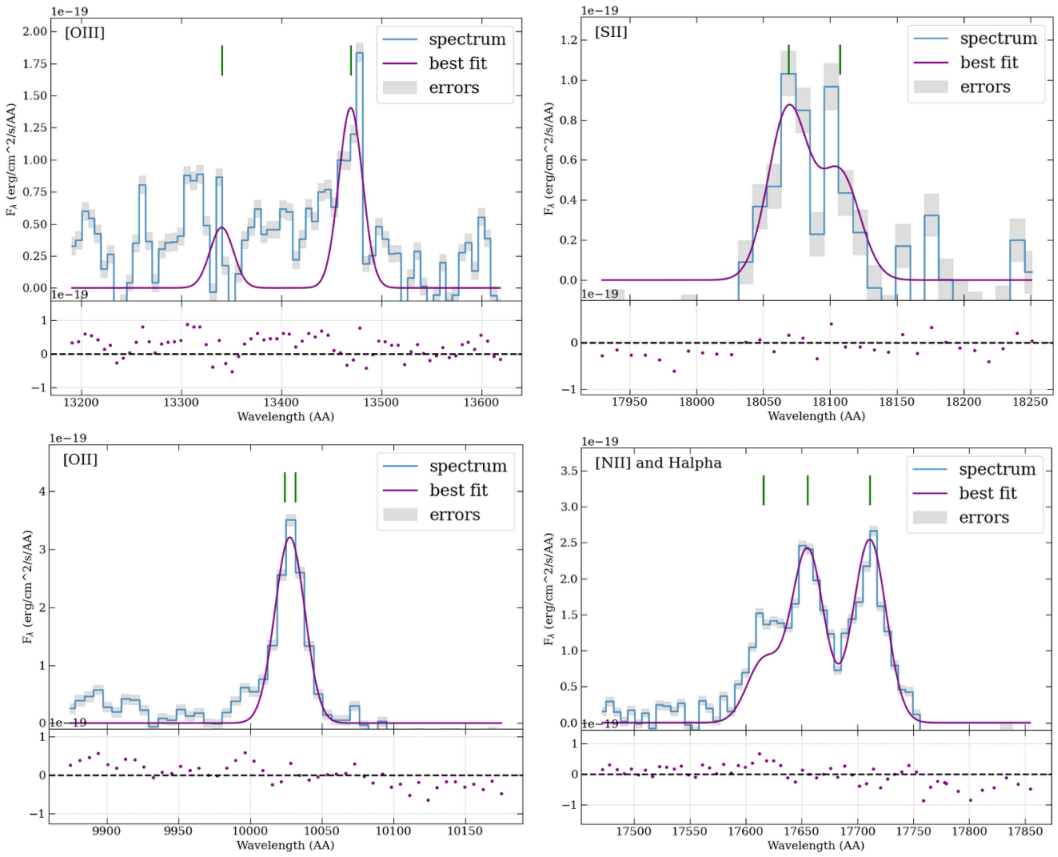

Figure 4.3: *Plots of the Gaussian fit for the emission lines of 4 spectral regions in the spectrum of COSMOS-8013. The best-fit is plotted in purple and the residuals of each fit are plotted under.*

The physical meaning behind these constraints is that the observations are not spatially resolved, thus the broadening of lines should only be given by the overall galaxy's kinematics and it should be fixed as equal for all of them; in addition, the gas' emission lines originate from the galaxy itself and so they are placed at the same systemic velocity as the stellar population (and each other). As will be explored in chapter 7, these assumptions do not hold up for all of the galaxies in the sample. It is also important to point out that the fit of the He I line was not done following these constraints, but was instead modeled to be free to vary in centroid position and width of the line: this choice was empirically determined by the different redshift and velocity

dispersion observed for this line compared to the other lines in the vast majority of spectra, in both the quiescent and the star-forming sample.

Finally, a caveat is to be made about the availability of the lines in different spectra: although the spectral range of the continuum-fitted sample should cover all of them, some are missing from a few spectra because they happen to fall in correspondence to a detector gap. In all of these cases, the fit simply ignores the missing lines.

4.2.2 Hα equivalent width

The equivalent width (EW) of the Hα line was also computed for those galaxies in which the line was successfully fitted. Since in most spectra of the sample the Hα line is blended with the neighboring [NII] lines, I chose to forgo the standard EW estimation from the observed spectra and employ a different method. In order to "deblend" the Hα line and obtain a more accurate measure of its EW, I created an artificial spectrum in which the fitted Gaussian line profile of only the Hα line was added to the continuum fit, so as to obtain a composite spectrum containing only its stellar continuum + a single, deblended Hα emission line: an example constructed on the Hα line region in COSMOS-8013 is illustrated in Figure 4.4.

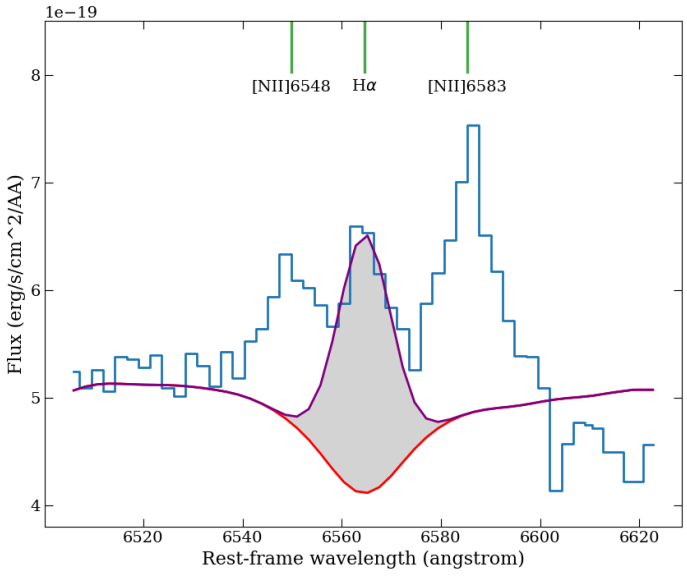

Figure 4.4: *A visualization of the spectrum constructed for the measurement of the Hα line: in purple, the line profile constructed from the Hα gaussian fit + the continuum emission, in red the Prospector continuum best-fit: the computed EW is defined as the width of a rectangle constructed under the continuum spectrum, whose area is equivalent to the shaded grey region between the emission and the continuum absorption.*

Finally, since a line's EW is conventionally defined in its rest-frame (laboratory) wavelength, I restored everything back to rest-frame using the redshift calculated from my emission lines fit. Once this is done, the EW of the line can simply be estimated

by computing:

$$EW = \int \frac{F_c - F_l}{F_c} d\lambda \ \text{Å}, \tag{4.1}$$

over the extent of the emission line.

The Hα line's EW is useful to get a first-order estimate of the importance of the nebular emission, tracing the ionized gas in the galaxy, with respect to the continuum, which in the optical/near-IR range is dominated by stellar emission. A very high EW is typical of star-forming galaxies, wherein the Hα emission produced by the many HII regions is very intense and the stellar continuum is low and dominated by massive O and B stars at lower wavelengths than 6562 Å. A low EW value, instead, is more common in red and quiescent galaxies, in which the continuum is much stronger due to the older (and redder) stellar population and the Hα line is not powerful due to the scarce presence of ionized gas and SF activity in the galaxy. The measured Hα EW is also useful as a diagnostic tool to investigate the origin of the underlying ionizing flux that produced the same line: this topic is further expanded upon in chapter 5.

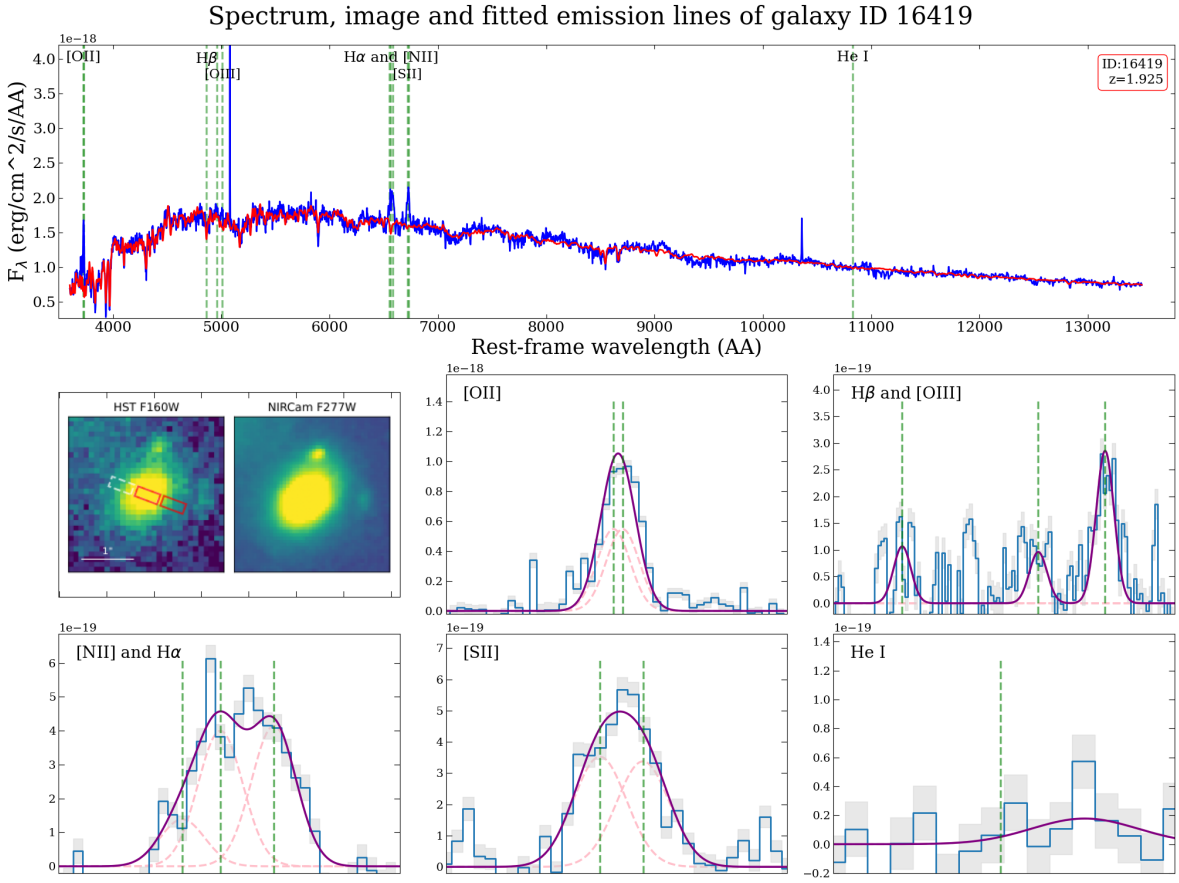

Figure 4.5: *Galaxy ID 16419: an example of a high SNR spectrum in my sample. Even though the continuum is very red and full of deep absorption lines, all of the plotted emission lines from ionized gas are present with SNR>3 (except for the He I line). In the top panel, the galaxy's spectrum (blue) with the continuum Prospector fit (red) plotted in the galaxy's rest-frame. Under that, we have the imaging data in the upper left panel and the emission lines in the remaining ones. In purple I have plotted the overall best fit, in pink dashed the single Gaussian profile of each line. In green dashed, the lines centroid positions given by the Prospector fit's redshift.*

4.3 Results from the Blue Jay sample

Out of the 22 galaxies of my sample, only **4** (i.e., $\sim 18\%$) show no ionized gas emission lines with SNR>3 (COSMOS-ID 8469, 10400, 12332 and 21477), which is the limit of line detection set in this work. The highest SNR line in most of the sample is the [OII]$\lambda\lambda$3727,3729 doublet, followed by the Hα/[NII] line group.

An example of the complete spectral fitting can be seen in Figure 4.5 where the full observed spectrum + stellar continuum fit of a single galaxy is plotted, along with a panel for each of the emission lines fitted and a stamp of the imaging data of the galaxy, in order to visualize the position of the slit with respect to the full extent of the object. The imaging data is shown in two panels: one contains the footprint of the NIRSpec MSA shutters during the target's observation superimposed onto HST imaging in the F160W filter from the 3D-HST parent sample's catalog (see ch. 3); the other panel shows JWST imaging data of the same object by the NIRCam instrument with the F277W filter, taken from the PRIMER Treasury Program (Dunlop et al., 2021).

In Table 4.2, I have collected the spectroscopic redshifts, velocity dispersions and Hα line equivalent width estimated by my fit in all of the sample galaxies.

Several emission lines have too low a SNR to be accurately fitted: in particular, the Hβ line is extremely faint in many systems. Furthermore, this line is actually seen in absorption in the observed spectra, so the fit of its component in emission depends on the accuracy of the stellar continuum model and it is often not detected as a consequence of an imperfect subtraction of the absorption component. The Hα line presents a continuum fit component in absorption as well: however, the component in emission is generally powerful enough to reach a sufficiently high SNR for most of the sample and thus still be detected. Interestingly, we observe a [NII]6581/Hα flux ratio higher than 1 in most of the sample, which is not typical of gas ionized by SF regions but is instead characteristic of AGN-powered photoionization: this topic will be further explored in the next chapter.

COSMOS ID	z (Prosp.)	z	σ_{em} km/s	EW (Hα) Å
7549	2.6248	2.6232±0.0004	99±62	7.3±0.7
7904	3.1003	3.09780±0.00016	89±16	266±20
8013	1.6894	1.68950±0.00023	227±34	7.7±0.4
8469	1.8683	–	–	–
9395	2.1273	2.1259±0.0007	461±73	$\leq$ 0.18
10128	1.8524	1.85170±0.00019	207±17	3.50±0.28
10339	2.3636	2.3634±0.0007	457±64	–
10400	2.1003	–	–	–
10565	2.4415	2.4421±0.0005	323±48	1.2±0.6
10592	1.8009	1.8004±0.0009	283±115	–
11142	2.4452	2.44480±0.00023	400±20	11.0±1.1
11337	2.0952	2.09400±0.00012	384±11	–
11494	2.0912	2.0891±0.0013	279±101	1.5±0.5
12175	3.5046	3.48900±0.00018	-126±16	174±10
12332	2.8260	–	–	–
16419	1.9254	1.9251±0.0007	365±74	5.7±0.8
17713	2.0914	2.0888±0.0016	300±187	$\leq$ 6.3
18668	2.0857	2.08580±0.00010	188±9	32.9±1.4
18688	2.0081	2.00680±0.00012	192±11	25.6±1.3
18977	2.0876	2.0865±0.0006	379±60	45±10
20238	2.4865	2.48590±0.00013	199±10	46.4±1.9
21477	2.4732	–	–	$\leq$ 3.9
21541	2.4770	2.4599±0.0013	722±102	$\leq$ 10.2

Table 4.2: *Global galaxy properties obtained from the emission lines fitting. The z (Prosp.) column shows the redshift estimated by the stellar Prospector fits, i.e. from the absorption lines. The 4 systems missing velocity dispersion measurements are the ones with no detected (SNR>3) emission lines. In some cases, EW(Hα) is not computed due the line falling in correspondence to a detector gap. Systems with Hα detected at SNR<3 only have upper limits on EW(Hα).*

Chapter 5

Ionized gas content and diagnostics from emission lines

5.1 Ionized gas in quiescent galaxies

Optical rest-frame emission lines in the spectrum of a galaxy are produced by the ionized gas phase of its ISM: the emitted lines are the result of electronic *recombination* or collisional excitation and are the carrier of a variety of information about the conditions they were produced in, such as the chemical composition, temperature and density of the ionized gas (see essential academic texts on nebular emissions Dopita & Sutherland, 2003; Osterbrock & Ferland, 2006; Strömgren, 1948; Tielens, 2005).
In a non-spatially resolved 1D spectrum of a galaxy, the measured optical emission lines are the integrated result of nebular emission coming from all around the galaxy and, if present, from the broad-line and/or narrow-line regions of an active nucleus.

Strong ionized gas emission lines are usually observed only in star-forming and active galaxies. In non-active galaxies, most of the ionized gas is indeed located in nebulas scattered throughout the galaxy, commonly referred to as *H II regions* since they contain mostly ionized hydrogen gas. In these regions, gas in the ISM is photoionized by the EUV flux of young O and B stars. These ions can produce emission when they recombine (as is the case for hydrogen emission lines) or as a result of collisional excitation.

In active galaxies, the predominant ionizing photon field is coming from the actively feeding SMBH at the galaxy's center and the produced emission lines can reveal complex dynamical structures in the circumnuclear ionized gas, with measurable narrow and broad velocity components (e.g. Brusa et al., 2015; Übler et al., 2023a, 2023b).

More difficult to constrain, gas in the ISM can also be excited by *shocks* that can be traced back to many phenomena, including galactic-scale outflows, galaxy interactions, RAM pressure stripping, and AGN related activity such as jets and AGN-driven winds and outflows (Kewley et al., 2019). Mergers can produce widespread shocks throughout galaxies which significantly affect the emission-line spectrum of a galaxy (Medling et al., 2015) and stellar wind-induced shocks have been observed both in star-forming and starburst galaxies (T. Heckman, Borthakur, Wild, Schiminovich, & Bordoloi, 2017; I. T. Ho et al., 2016).

The first and most important result of this work, however, is that in this new spectroscopic data many of previously unseen ionized gas emission lines in quiescent galaxies at z $\sim$ 2 are actually detected with SNR>3. This result is only made possible

by JWST and may represent a completely new window of investigation into the evolution of quiescent galaxies at high redshift.

5.1.1 Literature review and the new JWST frontier

The study of ionized gas in passive galaxies has represented a niche study topic in galaxy evolution studies for the past decades and has mainly focused on local Universe objects, due to the low percentage of warm ionized medium in passive galaxies' ISM and the difficulty of measuring faint emission lines beyond z $\sim$ 0.

The existence of a *warm* ionized gas phase in local passive galaxies, revealed by optical emission lines, has been known for a long time (see, for example, spectroscopic surveys by Buson et al., 1993; Phillips, Jenkins, Dopita, Sadler, & Binette, 1986). This kind of quiescent systems, sometimes referred to as *weak line* (or WL) quiescent galaxies, showed a warm ionized gas component estimated to represent around 1% of the total ISM (Buson et al., 1993) and sparked an interesting scientific debate in the early 90's about its origin: some sustained the hypothesis of an external origin of the warm ISM component, for example due to accretion from a companion galaxy (Bertola, Buson, & Zeilinger, 1992; Kim, 1989), others identified an internal ionizing source as the origin of the detected emission lines. Many internal ionizing mechanisms have been proposed, such as heat transfer from the hot, X-ray emitting gas halo to the cold phase ISM (Sparks, Macchetto, & Golombek, 1989; Voit & Donahue, 1990), low-power nuclear activity (as in LINERs) (Kim, 1989; Shields, 1992) and shocks (T. M. Heckman, Baum, van Breugel, & McCarthy, 1989).

The prevalent theory, however, explains the warm gas content as ionized by the hot evolved low-mass stars (HOLMES) contained in these no longer star-forming systems: this idea was put forward by Binette, Magris, Stasińska, and Bruzual (1994) and Macchetto et al. (1996) and theoretically proved even earlier, by considering the UV emission from hot HB stars, evolved massive stars and post-AGB star populations (di Serego Alighieri, Trinchieri, & Brocato, 1990; Minkowski & Osterbrock, 1959; Osterbrock, 1960; Terlevich & Melnick, 1985). This idea was taken up again more recently in the context of LINERs classification: Cid Fernandes et al. (2011, 2010), for example, have analyzed the "forgotten" WL galaxy population in the SDSS survey at z $\sim$ 0, in order to distinguish what they call *retired galaxies* (RGs), i.e. quiescent systems in which the remnants of ionized gas persists thanks to HOLMES photoionizing flux, from true LINERs, i.e. galaxies that hide low-power AGNs. This topic will be explored further in the next section of this chapter.

Beyond the limits of the local Universe, the picture becomes much less clear. The fitting of cosmic-noon's galaxies rest-frame optical emission lines is notoriously difficult to achieve from the ground, due to the high sky background emission and the partial absorption of light at these wavelengths by the Earth's atmosphere. This is even more challenging when the galaxy in question is *quiescent*, i.e. theoretically with very weak (if any) emission lines from ionized gas because of its low SFR. Even though many ground-based spectroscopic surveys of rest-frame optical emission lines in *star-forming* galaxies at Cosmic Noon exists, literature becomes much scarcer on the quiescent, non-active systems front: a study of this kind has been carried out by Belli et al. (2017), for example. Still, with the launch of JWST we are now seeing the first exciting results

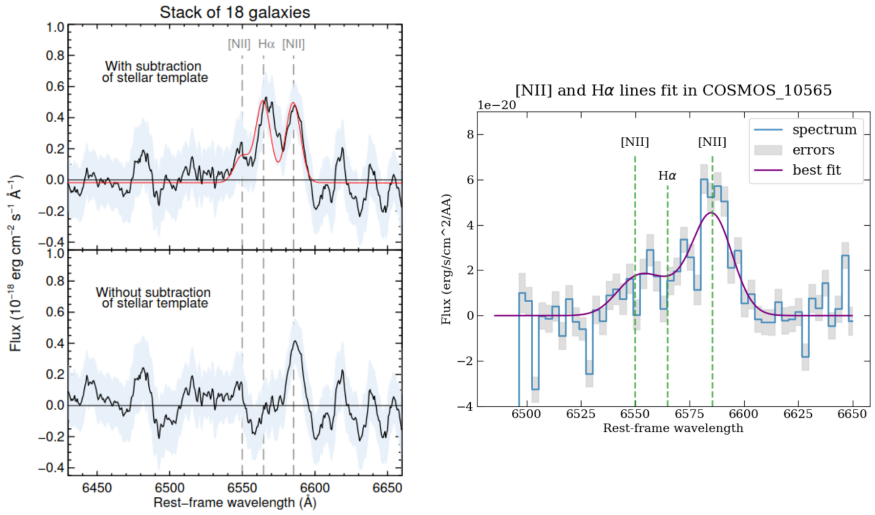

Figure 5.1: *Comparison between ground-based vs JWST spectral resolution: in the left panel, the [NII]/Hα lines + fit of the stacked spectra of 18 quiescent galaxies at* $1.5 < z < 2.5$ *observed with Keck's MOSFIRE, from Belli et al. (2019); in the right panel the same lines fitted in one of the lowest SNR galaxy in my sample. Notice the difference in flux of one order of magnitude between the two panels.*

regarding Cosmic Noon and higher-redshift galaxies, with some publications observing significant emission lines in (apparently) quiescent systems: Carnall et al. (2023), for example, observed a massive quiescent galaxy at z=4.658 with NIRSpec and found broadened Hα emission, indicative of the presence of a BL AGN.

The first important result of this emission line analysis on a relatively small sample of quiescent galaxies is the fact that I was able to successfully fit at least some emission lines from ionized gas in the spectra of most of the objects in my dataset. The quality of the new JWST NIRSpec data has made it possible to see what was hardly visible before (see Figure 5.1): the evidence is indicating that there is ionized gas in these passive systems at z $\sim$ 2, emitting not-so-powerful but clearly present emission lines typical of those found commonly in star-forming or active galaxies.

But once established that there is non-negligible ionized gas emission in these galaxies, the question that naturally follows is: what is the source behind the ionization of the gas?

5.2 Line diagnostic diagrams

For many galaxies in my sample, I was able to fit multiple emission lines in the same rest-frame optical spectrum, opening up the possibility to study this quiescent population through the *flux ratios* of different lines by the use of *line ratio diagrams*.

Line diagnostic diagrams are a valuable tool to investigate the underlying ionization mechanisms behind the production of ionized gas optical emission lines (see review by Kewley et al., 2019). Emission line strengths determined using photoionization models have proven to correlate with the signatures of different ionizing sources in galaxies (Cid Fernandes et al., 2011; Feltre, Charlot, & Gutkin, 2016; Shapley et al., 2015; Strom et al., 2017). This has led to the development of standard optical line ratio diagnostic diagrams to separate nebular emission by active and inactive galaxies, such as the Baldwin et al. (1981) (BPT) and Veilleux and Osterbrock (1987) diagrams. The comparison between emission line flux ratios obtained by standard photoioniza-

tion codes, e. g. MAPPINGS (Allen, Groves, Dopita, Sutherland, & Kewley, 2008a; Dopita, Sutherland, Nicholls, Kewley, & Vogt, 2013; Sutherland & Dopita, 1993) and CLOUDY (Ferland et al., 2013) and observations of star-forming and active galaxies (Kauffmann et al., 2003; Kewley et al., 2013; Kewley, Groves, Kauffmann, & Heckman, 2006; Stasińska, Cid Fernandes, Mateus, Sodré, & Asari, 2006) made it possible to further refine the empirical classification of galaxies through their simulated counterpart and a great number of different line ratios sensitive to different ionization sources have been found, spanning lines from the UV to the FIR wavelength range.

With the catalog of the emission lines at my disposal (Table 4.1), I was able to produce 4 different diagnostic diagrams and thus classify the underlying ionization source at the origin of the observed emission lines of my spectral sample. As will be shown in the next sections, these different diagnostic diagrams all point towards the same conclusion: most of the galaxies for which I was able to obtain measurements of all the required line ratios show clear signs of ionization due to an *active galactic nucleus*.

5.2.1 The BPT diagram

The most famous and widely used line diagnostic diagram is the so-called *BPT* diagram, after Baldwin, Phillips & Terlevich (Baldwin et al., 1981). This standard diagram uses the [NII]λ6584/Hα line ratio plotted against the [OIII]λ5007/Hβ ratio and has been proven a valuable observational criterion for differentiating between active and non-active galaxies up to high redshift, due to the fact that it employs relatively powerful and easy-to-measure emission lines (Kauffmann et al., 2003; Kewley et al., 2013; Kewley, Dopita, Sutherland, Heisler, & Trevena, 2001; Kewley et al., 2006, 2019; Stasińska et al., 2006).

In the case of quiescent (apparently non-active) galaxies, the BPT diagram has not been widely used in the literature as a means of classification, due to the general lack of powerful emission lines from ionized gas in these passive systems: some studies have focused on the BPT diagnostics of the so-called *retired* galaxy population at z $\sim$ 0 (e. g. Cid Fernandes et al., 2011, 2010; Lagos et al., 2022; Maddox, 2018), but scarce literature exists on this topic at redshifts higher than 1 because of the difficult observations of low-SNR lines when shifted to near-IR wavelengths. Some examples of this are found in Carnall et al. (2023) and Belli et al. (2023), but these articles, based on recent JWST data, only focus on a single object.

Many empirical, semi-empirical and theoretical selection criteria for nebular vs. AGN-powered emission lines exist in the literature: following the work done on the retired galaxy population by Cid Fernandes et al. (2011) (from now on CF11), I compared three different selection criteria:

(i) The observationally derived selection criteria by Kauffmann et al. (2003) (see also Kewley et al., 2013), based on the SDSS galaxies,

(ii) the theoretical limit of *extreme starburst* galaxies by Kewley et al. (2001) (K01), in which the authors used the SED modeling code STARBURST99 (Leitherer et al., 1999) to simulate the line ratios observed in extremely star-forming starburst galaxies;

(iii) and the empirical classification of the AGN population into Seyferts and LINERs given by Kewley et al. (2006).

The various selection criteria basically divide the diagram in two regions: HII regions and star forming galaxies form a clean sequence on the left part of the diagram, from low to high O[III]/Hβ ratios (Figure 5.2). This sequence is known as the *star forming galaxy abundance sequence* and its position can be affected by the metallicity of the ionized gas, the ISM pressure, the hardness of the ionizing radiation field, and the ionization parameter (Kewley et al., 2006).

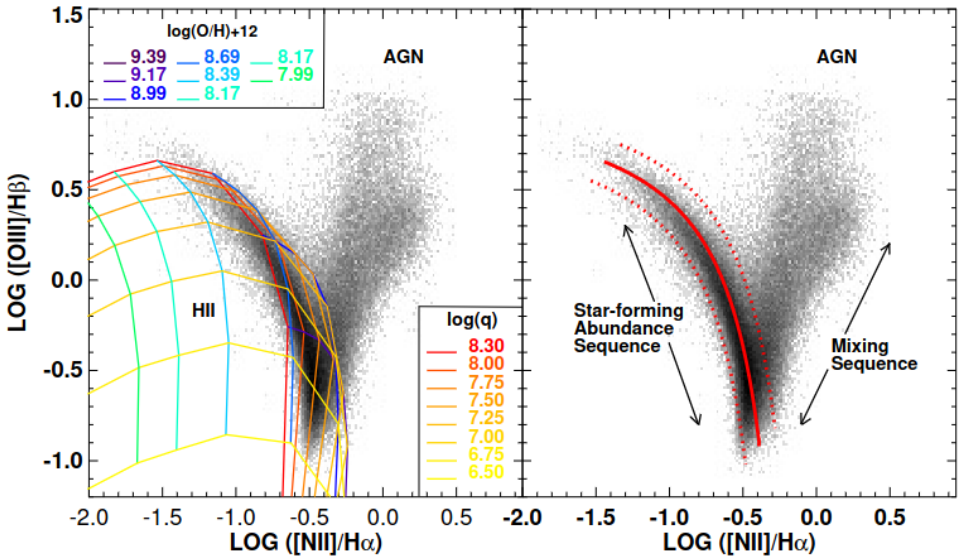

Figure 5.2: *The BPT diagram of the SDSS galaxies analyzed in Kewley et al. (2006). Left panel: the colored curves show theoretical photoionization model fits to the star forming abundance sequence; right panel: the mean star-forming sequence for local galaxies is traced by the red curve. From Kewley et al. (2019).*

An AGN contribution, on the other hand, raises the [NII]/Hα line ratio: this means that active galaxies are found at the higher-end of the [NII]/Hα axis. The position of AGN on the BPT diagram is sensitive to metallicity, and will move towards smaller [NII]/Hα ratios at low metallicity: low metallicity AGN are extremely rare in local galaxies (Groves, Heckman, & Kauffmann, 2006),but not so much at high redshift (see, for example, the extremely low-metallicity AGN found by Übler et al. (2023b) at z=5.55), possibly causing the AGN population to move towards the SF sequence. Shock ionized gas can also be responsible for the observed line ratios and occasionally overlaps with both the star-forming or the AGN sequence, further complicating the picture. The Kewley et al. (2001) selection limit is the theoretical *maximum starburst* line that marks the upper limit for star-forming galaxies on the BPT diagrams. Galaxies that lie above this line cannot be explained by any combination of pure starburst models, and must contain a significant fraction (30-50%) contribution from an AGN or shock excitation. The population of galaxies that are found between the maximum starburst line and the empirical SF limit by Kauffmann et al. (2003) is sometimes called the *composite* population or the *mixing sequence*: these galaxies may contain a mixture of star formation, shock excitation, and/or AGN activity.

Lastly, Kewley et al. (2006) found an empirical line of separation on the AGN side of the BPT that divides the Seyfert galaxies from the Low Ionization Nuclear Emission Regions galaxies, called LINERs: the exact nature of LINERs is a debated topic in extragalactic astronomy and the same LINER-type emissions could be traced back to a variety of different mechanisms (see Yan and Blanton (2012a) for a general review). Some LINER emission is associated with Low Luminosity AGN (LLAGN): these LINERs have properties consistent with gas ionized by the radiation from an inefficiently accreting, low luminosity supermassive black holes (L. C. Ho, Filippenko, & Sargent, 1993, 1996). Eracleous, Livio, and Binette (1995) proposed a "duty-cycle" hypothesis that could explain LINERs as the results of occasional bursts of activity by a central accreting black hole. Shocks by jets or other outflows may be required to power LINER emission, in addition to the emission from the AGN accretion disk (Molina et al., 2018): nevertheless, extended LINER emission can be produced by shocked regions produced by galactic-scale outflows (Dopita & Sutherland, 1995; I. T. Ho et al., 2016) or even by the ionizing flux of an evolved stellar population, such as post-AGB stars (Binette et al., 1994; Singh et al., 2013; Yan & Blanton, 2012b). These last kinds of objects are sometimes called LIERs, or *Low Ionisation Emission-line Regions*, in order to differentiate them from low-luminosity active nuclei.

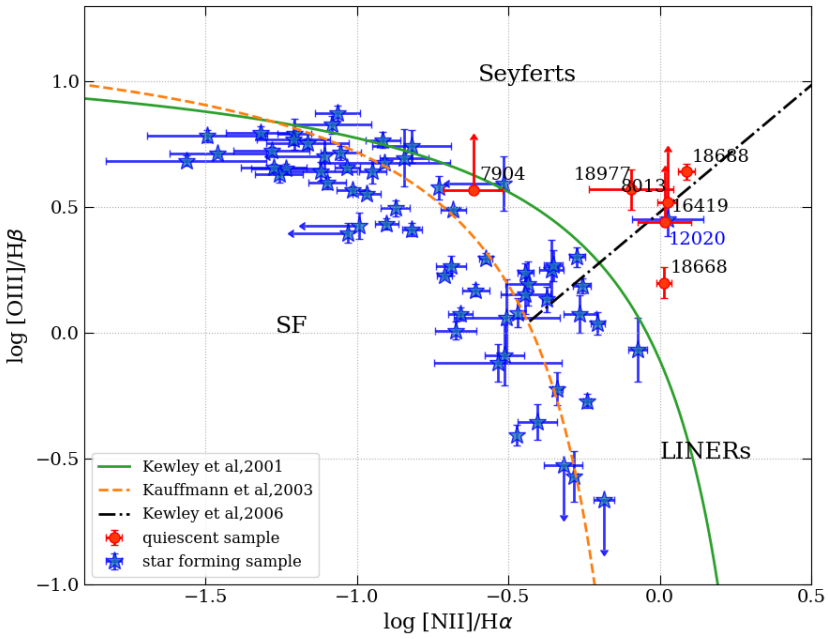

Figure 5.3: *BPT diagram of the Blue Jay galaxies. In red circles, my sample of quiescent galaxies, in blue stars the rest of the catalog. Plotted lines mark different classification criteria.*

To construct the diagram, I first selected only galaxies for which all of the four emission lines ([NII]λ6584, Hα, [OIII]λ5007 and Hβ) are detected with SNR >3, in line with the calibration used in Kewley et al. (2013). The same was done for the complementary SF galaxies sample, in order to compare the two populations from the Blue Jay survey, and everything is plotted in Figure 5.3.

These selection criteria are quite stringent for my galaxies, due to the fact that the Hβ line does not reach the required SNR in most of the quiescent sample: in order to

include as many systems as possible, I also chose to plot the galaxies that only have an upper or lower limit on the line ratios: this is done by selecting galaxies with at least one of the [NII]λ6584/Hα lines and one of the [OIII]λ5007/Hβ lines with SNR>3. The measured flux on the other line in the ratio is considered an upper limit and the point can still be plotted on the BPT diagram. An example of galaxies added this way are COSMOS-8013 and COSMOS-16419, as noted in Figure 5.3.

The first result from the BPT diagram is that we can immediately see a segregation of the two samples in different parts of the diagram: even though I was able to plot the line ratios for only some of the quiescent objects, all of the points are clustered together in the AGN-powered side of the diagnostic diagram, while the rest of the Blue Jay sample is firmly set in the star-formation part of the diagram. The only exception seems to be galaxy COSMOS-7904, which is straddling the upper end of the star-forming galaxy distribution.

The star-forming sample forms a nice sequence mostly contained within the K01 maximum starburst line: also in this sample we find a prominent exception, i.e. the only SF galaxy found in the AGN region: this is the galaxy COSMOS-20120, which is spectroscopically confirmed to be a broad-line AGN, as can be seen in fig. 5.4. This object is also detected in in the X-rays by the Chandra-COSMOS Legacy Survey Point Source Catalog (Civano et al., 2016).

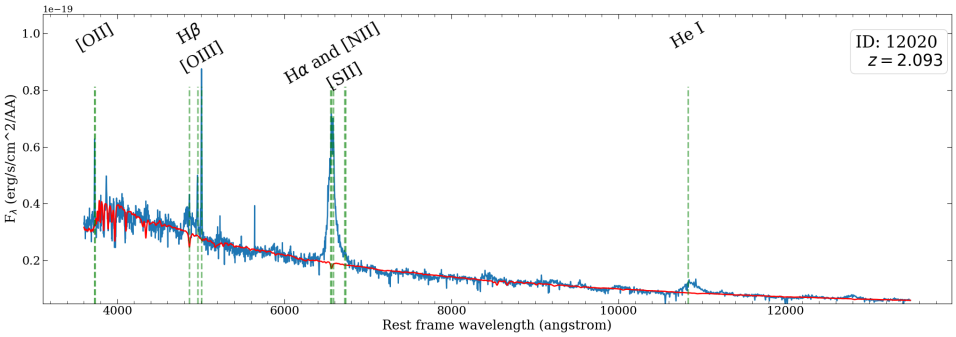

Figure 5.4: *Observed spectrum of the BL AGN COSMOS-12020 (blue) with the continuum fit superimposed in red. The line profiles of Hα, Hβ and He I are very broad.*

5.2.2 The WHaN diagram

The WHaN diagnostic diagram was introduced by Cid Fernandes et al. (2011, 2010) (CF10 and CF11) as an alternative diagnostic tool valid for those cases in which the fluxes of all 4 of the emission lines needed for the BPT diagram are not available: this makes it an excellent analysis diagram for my sample, since most of my quiescent galaxies cannot be placed on the BPT. The WHaN diagram replaces the [OIII]/Hβ line ratio (the most difficult to measure because of the Hβ line) with the *equivalent width* of the Hα line, which is usually the easiest to obtain. This diagram is particularly useful to differentiate between (weak) AGN and EL RGs (or emission line retired galaxies), which are passive systems in which gas is ionized by hot evolved p-AGB stars: CF10 and Stasińska et al. (2006) showed that the the proportion of such RGs misclassified as AGN in the BPT increases dramatically when considering weak emission line systems at z $\sim$ 0.

To distinguish true AGN from fake ones (i.e., the RGs), CF11 propose a practical division of the two populations in the WHaN diagram at EW(Hα) < 3 Å. The separation criteria between SF and AGN ionization in the [NII]/Hα ratio are the same as those showed in the previous section.

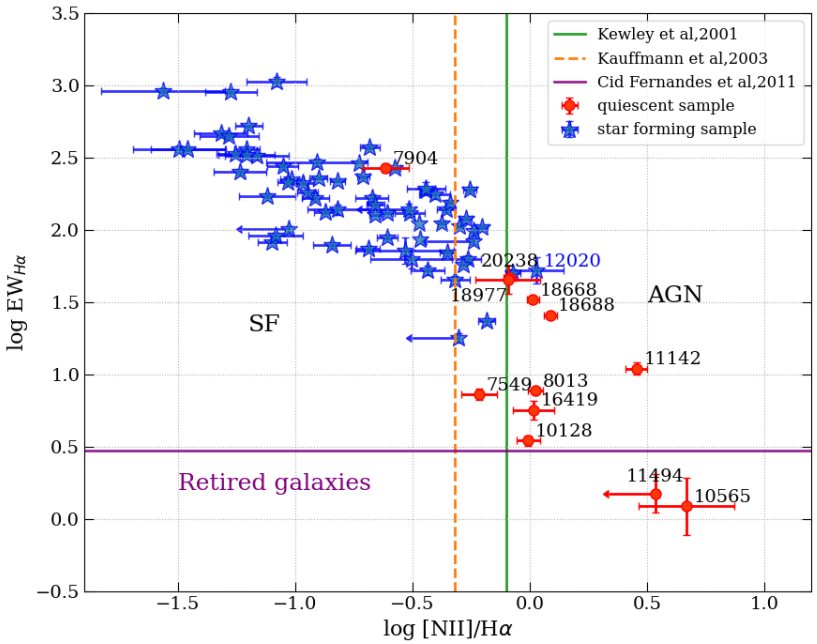

Figure 5.5: *WhaN diagram of the Blue Jay catalog.*

The WHaN diagram of the whole Blue Jay catalog is illustrated in Figure 5.5; quiescent galaxies are shown as red circles. The plotted vertical lines are the transposed version of the ones in fig. 5.3 and divide the SF from the AGN region. Immediately it is clear the advantage of using this diagram in the fact that I can plot almost double the points from my sample with respect to the classic BPT.

Nevertheless, the results of this diagram are in line with the BPT: most of my sample is still found clustered on the right side of the maximum starburst K01 line, while the rest of the Blue Jay catalog occupies the SF-powered left side of the plot. As before, the most notable exception is again COSMOS-7904, which can now safely be classified as a SFG.

All of the galaxies found in the BPT are present in the WHaN diagram, plus some additional ones: in total, **12** out of 22 galaxies are plotted. The purple horizontal line marks the 3 Å limit for the Hα EW, under which only two of my galaxies are found: according to CF11, this would mean that the only emission line galaxies whose emission can be completely attributed to the ionizing flux of an old stellar population are 2 out of 12. Similarly to what seen in the BPT, we find again the 12020 BL AGN amidst the quiescent galaxies sample.

5.2.3 Other line diagnostics

It is possible to extend the array of optical diagnostic diagrams to include the [SII]$\lambda\lambda$6716, 6731/Hα and [OIII]λ5007/[OII]$\lambda\lambda$3727,3729 line ratios, which are also sensitive to the

hardness of the ionizing radiation field.

The BPTo2 diagram, for example, replaces the Hβ line of the BPT with the easier-to-measure [OII]$\lambda\lambda$3727,3729 doublet and thus it is very useful in the case of weak emission lines such as the present study. Like the BPT diagram, this BPTo2 diagram also opens up into SF and AGN wings. One difference, though, is that the two branches of Seyferts and LINERs are more pronounced than in the classic BPT (CF10), probably due to the fact that ionization state and reddening are positively correlated, i.e, that Seyferts are more heavily reddened than LINERs (L. C. Ho, Filippenko, & Sargent, 2003; Kewley et al., 2006), and thus the value of the observed [OIII]/[OII] ratio varies significantly. Besides this extrinsic effect, [OIII]/[OII] is more sensitive to the ionization state than [OIII]/Hβ, which also enhances the separation between Seyferts and LINERs (CF10).

The BPTo2 diagram of the Blue Jay galaxies can be seen in Figure 5.6: again, this plot is in agreement with the previous two. The quiescent sample is still found on the AGN-powered side of the diagram and, additionally, we can see a more drastic separation of the red points above and below the Seyferts/LINERs separation line, suggesting a more robust classification than the one offered by the BPT. As before, 7904 is the only galaxy of the sample found among the star-forming sequence.

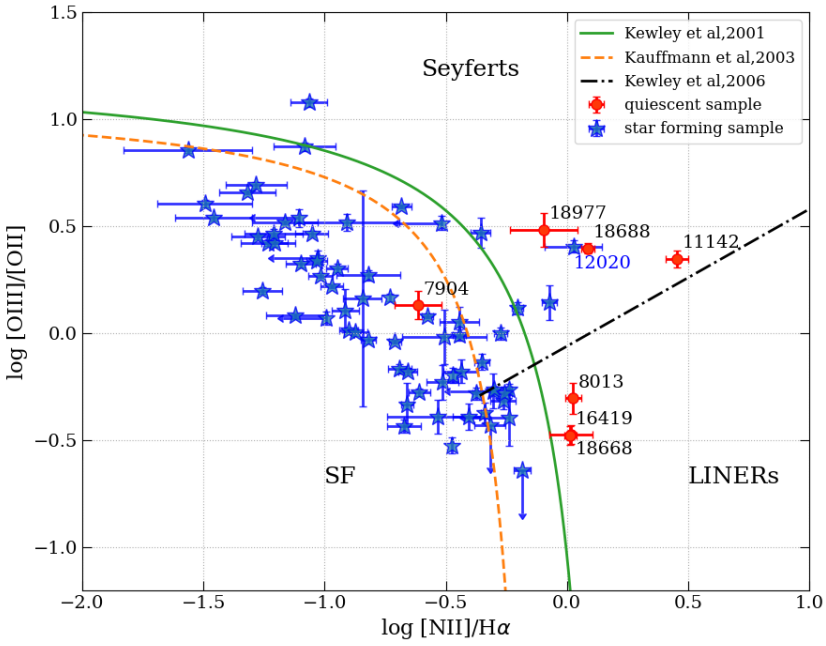

Figure 5.6: *The BPTo2 diagram.*

The last diagram constructed from my data is the [SII]$\lambda\lambda$6716,6731/Hα vs [OIII]/Hβ, which was first empirically calibrated for SF/AGN diagnostics by Veilleux and Osterbrock (1987): the [SII]/Hα line ratio is very much sensitive to the hardness of the ionizing radiation field (Veilleux & Osterbrock, 1987), but this diagram has the disadvantage of suffering from low SNR of both the Hβ line and the [SII] doublet, which is hardly detected in most of the quiescent sample. This results in a less clear diagnostic diagram visible in Figure 5.7, in which the general trends observed in the previous plots

are retained, but the SF and quiescent sample are much more intermixed: one sure hint of this fact is that the known BL AGN COSMOS-12020 is actually found mixed in with the star-forming Blue Jay galaxies and not clearly separated from them, as it happened in the other plots. Aside from the 7904 system, also COSMOS-18668 is found within the maximum starburst K01 boundary in this diagram. The [SII]/Hα diagram is also able to distinguish between Seyfert galaxies and LINERs (black dash-dotted line in Figure 5.7).

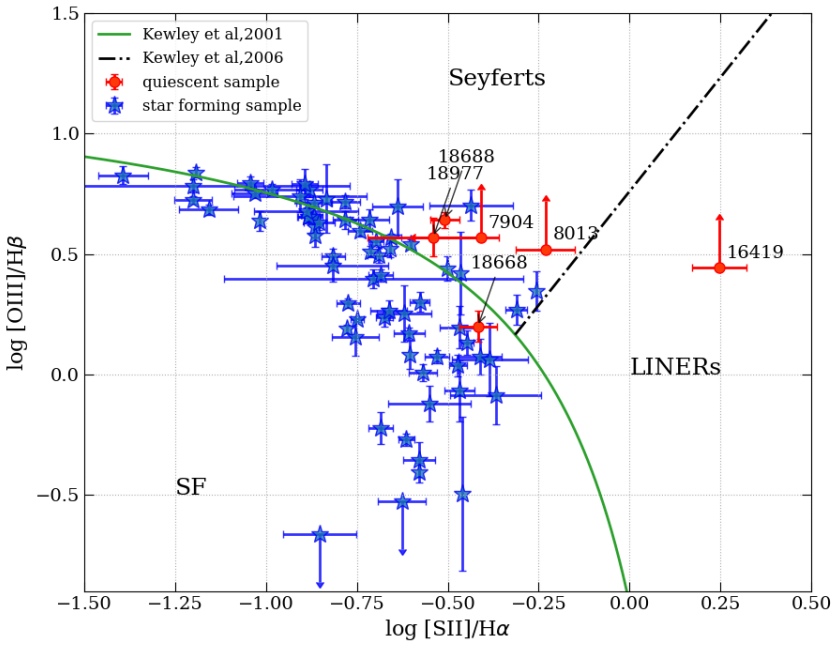

Figure 5.7: *[SII]/Hα diagnostic diagram.*

The less clearly defined results from this last diagram could be traced back to the fitting of the [SII] doublet lines, which suffers from low flux and slightly worse continuum subtraction in many galaxies of both the SF and the quiescent sample: this is reflected in the generally larger horizontal error bars in the plot.

5.2.4 Comparison with SDSS data

It is very instructive to compare the distribution of my points with the general distribution of a very large sample of galaxies on the diagrams: one quick way to do this is to use data from the Sloan Digital Sky Survey telescope. The SDSS data used in this work is taken from the MPA-JHU DR7 release of spectral measurements [1] (Tremonti et al., 2004) and their distribution on the diagnostic diagrams is illustrated by the grey points in Figure 5.8.

From the BPT diagram we can observe that the star-forming sequence formed by the Blue Jay galaxies is shifted towards higher [OIII]/Hβ ratios than with respect to the

[1] Online repository: https://wwwmpa.mpa-garching.mpg.de/SDSS/DR7/platelist

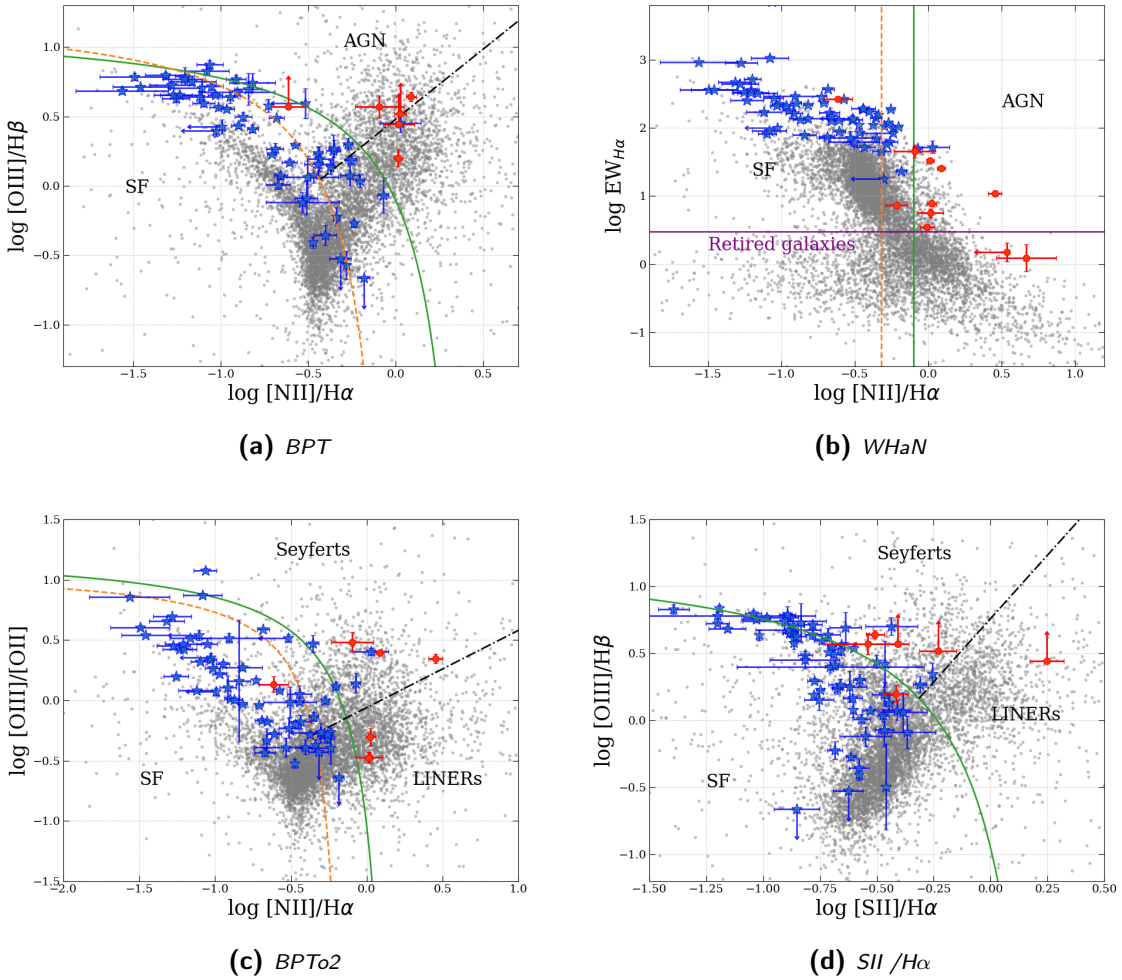

Figure 5.8: *Diagnostic diagrams of the Blue Jay galaxies compared to the SDSS galaxies, mapped in grey points.*

SDSS sequence: this is a well known difference between z $\sim$ 0 and Cosmic Noon star-forming galaxies (Kewley et al., 2019; Strom et al., 2017). One possible explanation of this shift towards higher line ratios, observed also in the BPTo2 and the [SII]/Hα diagrams, is given by Kewley et al. (2013) and Shapley et al. (2019): this shift can be traced back to the effect of a harder EUV ionizing flux, which can be linked to the *metallicity* of z $\sim$ 2 galaxies. Indeed, a lower-metallicity and α-enhanced young stellar population, as typically observed in Cosmic Noon SF galaxies, naturally produces a harder EUV ionizing flux than the one typical of a local Universe SF galaxy's stellar population (Sanders et al., 2020; Steidel et al., 2016). Even though these observations do not concern the population of interest in this work, i.e. the quiescent one, it is still important that I was able to replicate these known results from literature as an indication of the validity of my results as a whole.

Even considering the effects of metallicity evolution with redshift on the BPT diagrams, my quiescent sample is still clearly separated from the SF sequence; thus the quiescent sample cannot be interpreted as a mistaken population of low-metallicity SF galaxies. This can easily be seen comparing my results to Figure 5.9, taken from Shapley et al. (2019), in which the SF sequence for galaxies at z $\sim$ 2 is traced.

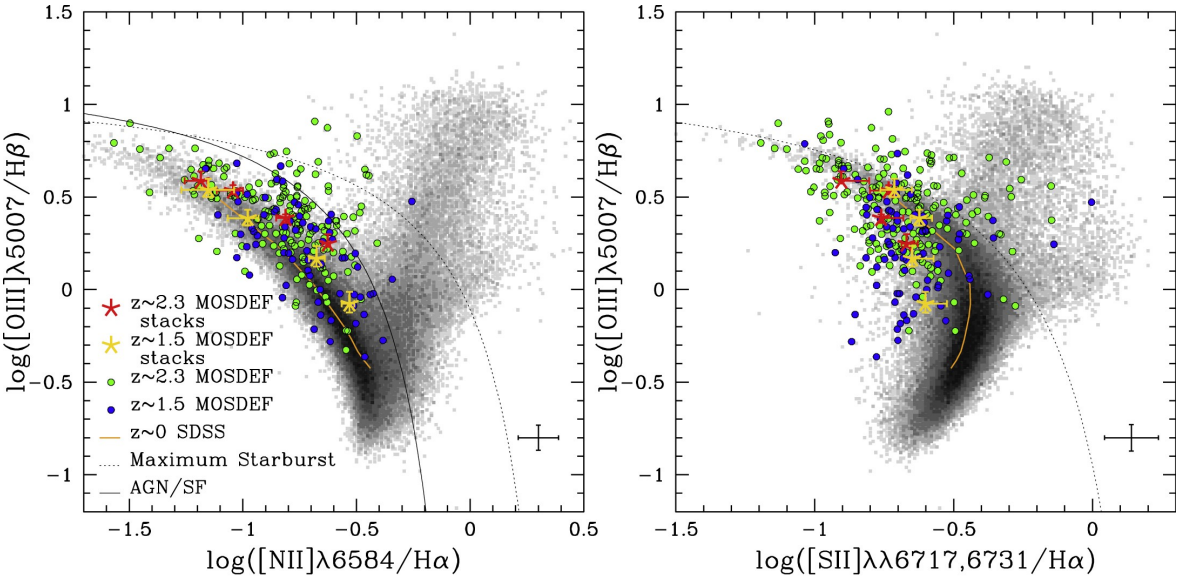

Figure 5.9: *BPT (left) and [SII]/ Hα (center) diagrams for 1.4 ≤ z ≤ 2.7 MOSDEF star-forming galaxies, adapted from Shapley et al. (2019). The grayscale histogram and orange curve correspond, respectively, to the distribution and running median of local SDSS galaxies.*

On the WHaN diagram, the distribution of both the SF and the quiescent sample is systematically shifted towards higher values of EW(Hα) with respect to the SDSS catalog. A similar, although less prominent shift, can also be seen in Belli et al. (2017)'s WHaN diagram of KMOS-3D galaxies at $0.7 < z < 2.7$. This shift could be traced back to the higher SFR typical of Cosmic Noon galaxies with respect to the local ones (Madau & Dickinson, 2014), which in turn would produce higher Hα EW and shift the diagram's distribution upwards along the vertical axis.

The question that remains open is whether the ionization by old stars limit set at EW = 3 Å by CF11, which is empirically calibrated on local galaxies, still holds up at high redshift. The quiescent galaxies observed by Blue Jay are necessarily younger than those observed at $z \sim 0$, since the age of the Universe at $z \sim 2$ is only 3 Gyr. Photoionization models show that the "LIER" emission due to post-AGB stars is actually weaker in young stellar populations (Byler et al., 2019). This means that the Hα emission by retired galaxies at Cosmic Noon must be even fainter than the EW=3 Å limit set by CF11. We thus conclude that this type of ionization is not relevant for the vast majority of the galaxies considered in this study.

5.3 The nature of emission line excitation in the Blue Jay quiescent sample

The classification of galaxies in my sample using diagnostic diagrams is summed up in Table 5.1. The subset of galaxies that I was able to classify is **12** out of 22 in the quiescent sample: the rest of them are either missing the required emission lines altogether or they have way too low SNRs for the diagrams to be reliable. As we can see from the Table 5.1, 5 galaxies (IDs 7549, 10128, 10565, 11494 and 20238) are only classified by a single diagram: the two retired galaxies, 10565 and 11494, are not missing any emission line in their spectra, but the WHaN diagram is the only one that contains them since the SNR of all of the other line ratios is systematically too low. This is an

ID	BPT	WHaN	BPTo2	[SII]/Hα
7549	-	Composite	-	-
7904	Composite	SF	SF	SF
8013	Seyfert	AGN	LINER	Seyfert
10128	-	AGN	-	-
10565	-	RG	-	-
11142	-	AGN	Seyfert	-
11494	-	RG	-	-
16419	LINER	AGN	LINER	LINER
18668	LINER	AGN	LINER	SF
18688	Seyfert	AGN	Seyfert	Seyfert
18977	Seyfert	AGN	Seyfert	Seyfert
20238	-	AGN	-	-

Table 5.1: *Classification of the quiescent Blue Jay sample according to various diagnostic diagrams*

expected result and nicely shows the usefulness of the WHaN diagram in "catching" and classifying galaxies that would otherwise be lost.

One galaxy (7904) is classified as star-forming/composite by every diagram and thus can be considered a contaminant of the UVJ-selected quiescent sample. Another galaxy, COSMOS-7549, is also classified as part of the *composite* galaxy population: since this system can only be plotted in the WHaN diagram, as it completely lacks any [OIII] emission, the classification is not so sure as it is the previous case. The gas in this particular system could be ionized by a mixture of star-formation and low nuclear activity. Its spectrum can be seen in Figure 5.10: it shows some metal and Balmer absorption lines and some weak [OII] and Hα emission. A clearer picture of the amount of SF going on in this system will be provided by the SFR estimation in the next chapter.

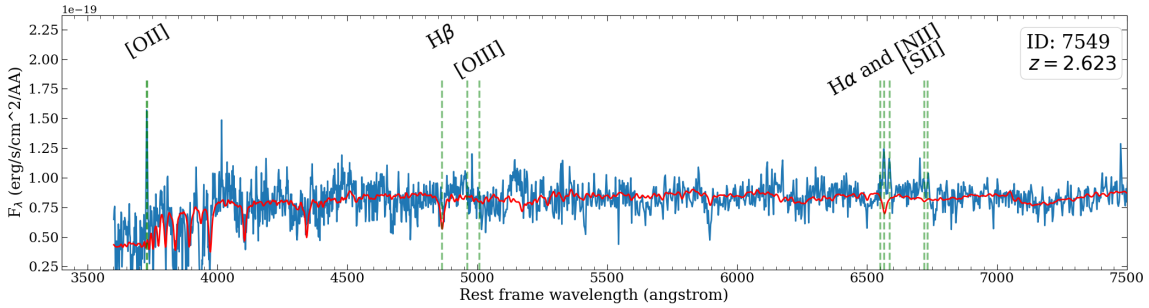

Figure 5.10: *Rest-frame spectrum of COSMOS-7549 (blue) with continuum fit superimposed in red.*

5.3.1 Hidden nuclear activity and the link to star-formation quenching

The most important insight that we get from Table 5.1 is that the majority of this subsample of quiescent galaxies hosts an active nucleus. Two of these systems are

actually classified as LINERs (COSMOS-16419 and COSMOS-18668), which is a not-so-well defined category that could refer either to low ionization emission galaxies that host a low-luminosity AGN or to emission attributable to shock-ionized gas from stellar outflows and/or ionization from hot evolved stars. However, these systems are classified as quiescent by the rest- frame UVJ color selection, thus the hypothesis of shocks from stellar outflows hardly holds up; furthermore, the WHaN diagram does not classify these systems as retired galaxies. Thus I can reasonably trace back the LINER emission of these galaxies to a LL AGN.

AGN detections represent 67% of the quiescent galaxy population for which we have strong detection of at least the [NII]λ6583 and Hα emission lines, corresponding to a global 36% of all galaxies in the quiescent sample. This is a surprising result, since these sources are not classified as AGN in other COSMOS field surveys: for example, these sources are not detected in the X-rays by either the Chandra-COSMOS Legacy Survey Point Source Catalog (Civano et al., 2016) or the COSMOS XMM Point-like Source Catalog (Cappelluti et al., 2009). One of these X-ray undetected sources in my sample, COSMOS-18977, is even showing evidence of broadened Hα and Hβ emission lines, typical of a Broad Line AGN (Figure 5.11).

This means that without being able to get high-quality NIR spectra of these galaxies to measure their optical rest-frame emission line ratios, no signs of nuclear activity would be suspected to be going on inside these systems.

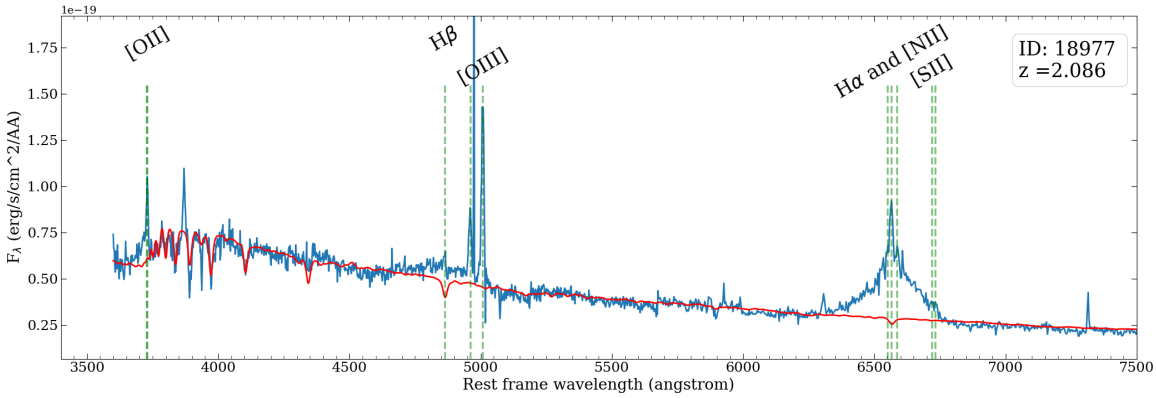

Figure 5.11: *Rest-frame spectrum of the BL AGN COSMOS-18977 (blue) with continuum fit superimposed in red.*

This result is relevant to the question at the heart of star-formation quenching: what caused these galaxies to become (and remain) quiescent? The physical origin of the star formation quenching is still unclear, and many mechanisms have been proposed: for high-mass galaxies, the most frequently invoked one sees the quenching of star formation as a consequence of *AGN feedback* (Fabian, 2012). The observational evidence for AGN feedback remains elusive, however. Several approaches have been exploited so far to find and study galaxies in the quenching phase (Park et al., 2023; Quai, Pozzetti, Citro, Moresco, & Cimatti, 2018), while some studies focus on passive, already quenched populations (Belli et al., 2017, 2019). The amount of hidden AGN in my quiescent sample points towards an empirical link between the quenched nature of these systems and the presence of an active nucleus: in this case, the evidence suggests an important contribution of AGN-driven feedback processes for the star-forming to

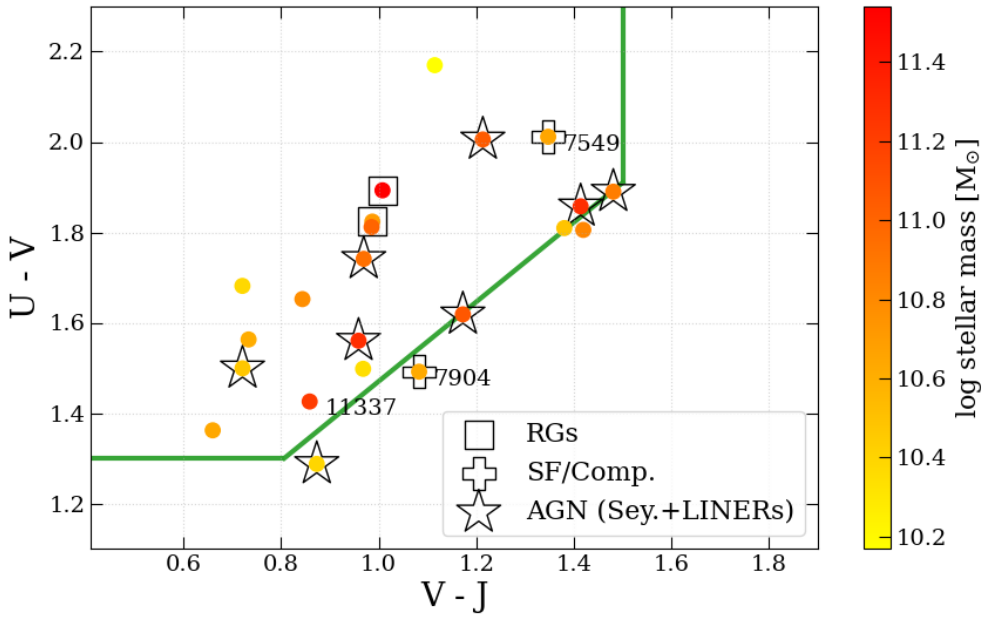

Figure 5.12: *UVJ diagram of my sample after the classification, colored with respect to the stellar mass: the black contours indicate the galaxy's classification. The green line marks the standard UVJ selection criteria illustrated in ch. 3. The three annotated objects are the two SF (Composite) galaxies COSMOS-7904 and 7549 and the merger COSMOS-11337.*

passive transformation of these galaxies at z $\sim$ 2.

Particularly interesting, in these regards, are the "quenching" galaxies I selected by relaxing the UVJ color-selection criteria, i. e. those galaxies found at the boundaries of the selection and that are supposedly caught in the transition phase between star-forming and quiescent. Going back to the rest-frame UVJ diagram, in Figure 5.12 I plotted my quiescent sample with respect to their line ratio classification (various symbols) and colored the scatter plots depending on their stellar mass, to investigate if any trend with mass is present. As we can see from the plot, in the region below and across the standard Muzzin et al. (2013) UVJ-selection boundary we find only one star-forming galaxy: the rest of the objects are classified as AGN, apart from two galaxies whose nature could not be determined. This trend is in line with the hypotesis of quenching of star formation in massive systems brought on by AGN feedback, as these "transitioning" galaxies overwhelmingly show evidence of nuclear activity.

We also notice a pattern in the non-classifiable vs classified objects' stellar mass: in particular, galaxies with too-low SNR to be put onto a diagnostic diagram are low-mass, which is to be expected. This could also mean that the same line ratios observed in higher-mass systems are also present in these galaxies, but are simply below the detection limit. There is only one exception to this trend: galaxy COSMOS-11337, which under closer inspection seems to be a *merger*, as seen from the very broad forbidden emission lines and the HST/NIRCam imaging in Figure 5.13. Unfortunately, most of the lines in its spectrum fall into the detector gaps, thus making it impossible to classify using diagnostic diagrams. This merger is also detected in the X-rays by the Chandra-COSMOS Legacy Survey Point Source Catalog (Civano et al., 2016).

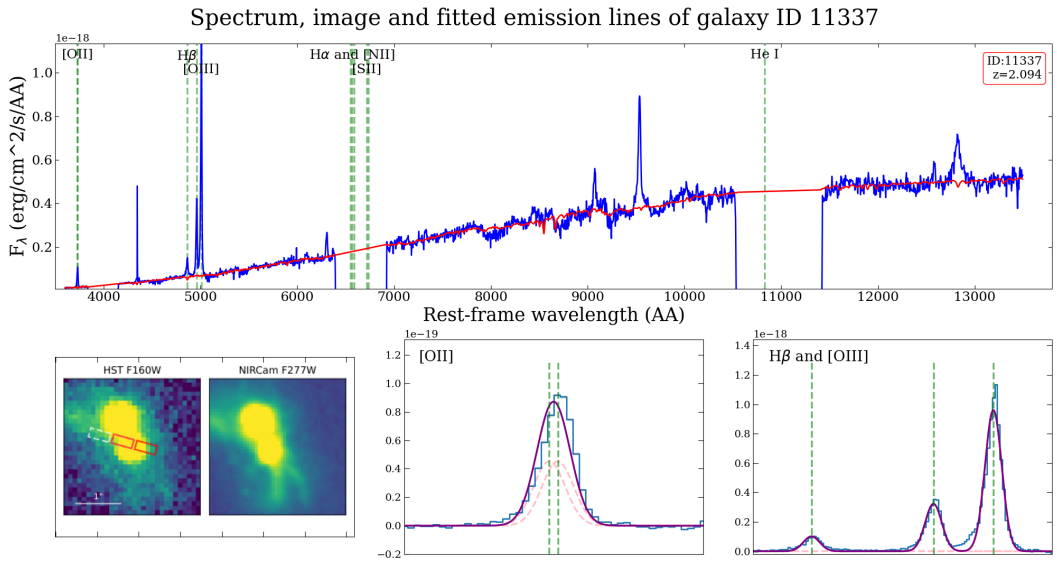

Figure 5.13: *Rest frame spectrum + continuum fit (upper panel) with imaging data and fitted emission lines (lower panels) of the merger COSMOS-11337*

The diagnostic diagram analysis of my sample has shown exciting results that revealed a relevant presence of never-before detected active galaxies in a sample of quiescent galaxies at Cosmic Noon. My analysis thus reveals a connection between the quiescent nature of these massive galaxies and AGN activity and feedback. An assumption that still needs to be verified, however, is whether my sample is actually composed of quiescent galaxies, i.e. whether the selection of my sample is accurate. This can be verified by estimating the current SFR of the sample and is the topic of the next chapter.

Chapter 6

SFR estimation from the Hα line

The current star formation rate (SFR) is one of the most important parameters used for characterizing a galaxy: the primary division between *star-forming* and *quiescent* galaxies lies in the fact that the former are actively producing new stars, while in the latter few or no new stars are born, leaving systems made up of mainly old, red and aging stellar populations.

Various indicators of galaxy SFR exist at different wavelengths, and include Hα and [OII] emission line luminosities, ultraviolet continuum luminosity, far-infrared (FIR) luminosity and radio luminosities (Hopkins et al., 2003; Kennicutt, 1998; Ly et al., 2011; Rosa-González, Terlevich, & Terlevich, 2002; Salim et al., 2007). Most studies rely on these indicators to estimate the current SFR of a galaxy because they are all linked to the typical emission spectrum of HII (or star-forming) regions.

In particular, the luminosity of the Hα nebular emission line has been widely used as a reliable SFR indicator both at high and at low redshifts, since it can be physically connected almost directly to short-lived massive stars. In the local universe, this relation has been well calibrated (Kennicutt, 1998; Kennicutt et al., 2009), and subsequently has been extended to calculate the SFR of distant galaxies (Brinchmann et al., 2004; Förster Schreiber & Wuyts, 2020; Shapley, 2011).

From the fitting of emission lines in my sample, I have highlighted the surprising results derived from the line ratios diagnostic diagrams (Chapter 5), which point to an AGN-powered origin of the ionized gas emission for many of these quenched systems.

The calculation of the current SFR for the galaxies in my sample is crucial in order to verify whether these are actually quiescent systems. Given that the observed emission lines are produced by an active nucleus, this would be another, important piece of the puzzle that links the quenching of SF in passive systems to AGN activity and, in particular, AGN feedback.

6.1 Theoretical relations

In estimating the SFR from the Hα luminosity we adopt the calibration given by Kennicutt (1998), applied to a Chabrier IMF (Chabrier, 2003):

$$SFR_{H\alpha}\,[M_{\odot}/yr] = 4.63 \cdot 10^{-42}\; L_{H\alpha}\,[\mathrm{erg/s}], \tag{6.1}$$

in which the Hα line luminosity is given by the measured Hα fitted line flux, adopting the standard ΛCDM cosmology for the calculation of the luminosity distance.

6.1.1 Dust correction

There are two main issues that need to be taken into account in order to obtain an Hα luminosity representative of the full emission from the galaxy: first, we need to consider the effects of slit loss on the measured flux of the observed emission line, and secondly we need to correct for intrinsic obscuration effects due to possible *dust attenuation* present in the galaxy (Salim & Narayanan, 2020).

As already discussed, the observed flux over the whole spectrum of each galaxy has already been flux-corrected using the spectroscopic + photometric Prospector fit of the stellar continuum: considering, as a simplification, that the Hα emission that we see is originating mainly in HII regions evenly scattered throughout the galaxy (and not, for example, only from a central source), the flux scaling applied to the spectrum's continuum can be reasonably applied also to the emission line flux, to account for the Hα flux lost from the slit. This will be an assumption to keep in mind in the interpretation of the measured SFR, since in the case of Hα originating mainly from an active nucleus the slit-loss calibrated SFR is higher than the true one.

The second flux correction, accounting for dust, is applied following the didactic example present in Rosa-González et al. (2002) and uses the standard Calzetti et al. (2000) dust extinction law.

Calzetti (1999) and Calzetti et al. (2000) have developed an empirical method based on the UV slope of starburst galaxies to estimate the effects of dust attenuation which is also applicable to the spectrum of cosmic-noon galaxies. In this hypothesis, the intrinsic flux at wavelength λ is related to the observed one by:

$$F_{int}(\lambda) = F_{obs}(\lambda)10^{0.4A(\lambda)}, \quad \text{with} \quad A(\lambda) = A_V k(\lambda)/R_V \tag{6.2}$$

where A_V is the V-band extinction and $k(\lambda)$ is given by Calzetti et al. (2000)'s extinction law:

$$k(\lambda) = 2.659 \cdot (-2.156 + 1.509/\lambda - 0.198/\lambda^2 + 0.011/\lambda^3) + R_V, \tag{6.3}$$

with $R_V = 4.05$.

The extinction law $k(\lambda)$ is given by eq.(6.3), so the only quantity missing for obtaining the intrinsic Hα line flux is A_V: in order to derive it, I take advantage of the Prospector continuum fit. The Prospctor code, indeed, was used to fit both the stellar population of each galaxy and its dust content.

Similarly to what was done in Park et al. (2023), the dust attenuation curve in the Prospector fitting of the sample employs the two-components dust model of Charlot and Fall (2000), in which the overall stellar continuum attenuation is due to a dust optical depth associated with diffuse ISM dust, attenuating the emission of all stars, plus an additional dust component that is found inside dense star-forming clouds and is only attenuating the light of young, massive stars still embedded in their birth clouds. This two-component dust model is fitted by Prospector using two parameters:

(i) τ_{ISM} = diffuse ISM dust optical depth
(ii) $f_{\tau,BC}$ = fraction of ISM dust found in birth clouds

so that the total dust optical depth of the galaxy is given by:

$$\tau_{dust} = \tau_{ISM} + \tau_{BC} = \tau_{ISM}(1 + f_{\tau,BC}) \tag{6.4}$$

There is also a third dust parameters that is used by Prospector in order to better model dust extinction: this parameter is a power-law modifier δ to the Calzetti dust attenuation curve. The modifier is estimated using the empirical relation found in Kriek and Conroy (2013) and is supposed to improve the Calzetti model for distant galaxies. Eq.(6.2) is modified with:

$$A(\lambda) = \frac{A_V}{R_V} k(\lambda) \left(\frac{\lambda}{\lambda_V} \right)^{\delta}. \tag{6.5}$$

In my case, however, I chose to ignore the power law modifier in my SFR estimation and use directly use the unmodified Calzetti law, since at the Hα line wavelength the term $\frac{\lambda}{\lambda_V} \sim 1$ and the estimated SFR from Hα luminosity remains the same. Thus, the V-band dust attenuation estimated from Prospector is:

$$A_V = 1.086 * \tau_{ISM}(1 + f_\tau) \tag{6.6}$$

This is then plugged into eq.(6.7) to get the unattenuated Hα line flux.

Finally, eq. (6.2) can be used to work out the dust-corrected Hα emission line flux:

$$F_{int}(H\alpha) = F_{obs}(H\alpha) 10^{0.4 A_V k(H\alpha)/R_V}. \tag{6.7}$$

The choice of including both the diffuse ISM and the birth-cloud dust components for my sample is not straightforward and requires a logical justification: it would be compelling to simply discard the dust component of star-forming regions, since galaxies in my sample are *quiescent* and thus should not contain active sites of star formation. The ultimate goal of estimating the SFR in my sample, however, is to prove that (most) of my galaxies are in fact quiescent and do not have substantial dust-hidden star formation activity. In order to prove so, then, we need to drop the quiescent assumption from the dust attenuation calculation and consider the "worst-case scenario" of attenuation given by both dust components: this is why the SFRs of the quiescent sample estimated in this way are to be considered strictly *upper limits* on the actual SFR of these galaxies. Furthermore, from Chapter 5, we know that most of these galaxies actually host an active nucleus and thus the Hα emission that we measure is not produced by star-forming regions, but rather by the gas surrounding the central accreting SMBH: this further stresses the importance of considering the measured SFRs as upper limits.

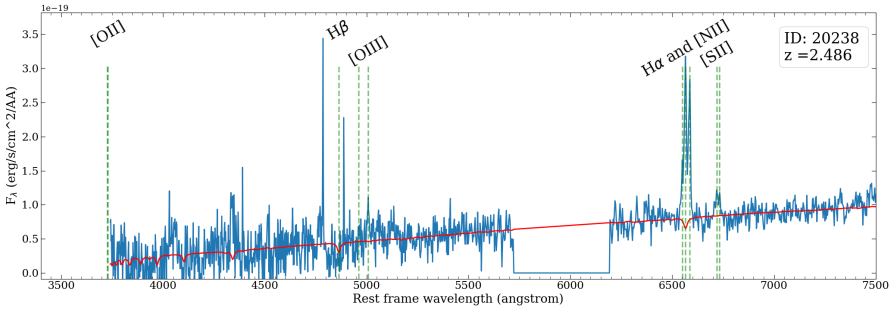

Figure 6.1: *Rest-frame spectrum (blue) of COSMOS-20238 with continuum fit (red), cut to λ=7000 Å*

6.2 Results

The results of the SFR estimate from the Hα line are gathered in Table 6.1: as we can see from the fourth column, most of the sample is indeed very quiescent, with many systems having SFR lower than 1 $M_\odot$/yr, keeping in mind that these values are *upper limits* on the actual SFR. The systems that are hosting an AGN, as expected, have generally higher SFR that the rest of the sample: their measured SFR are not reliable, however, since the Hα emission is mostly produced by the active nucleus and not from actual star-formation regions in the galaxy.

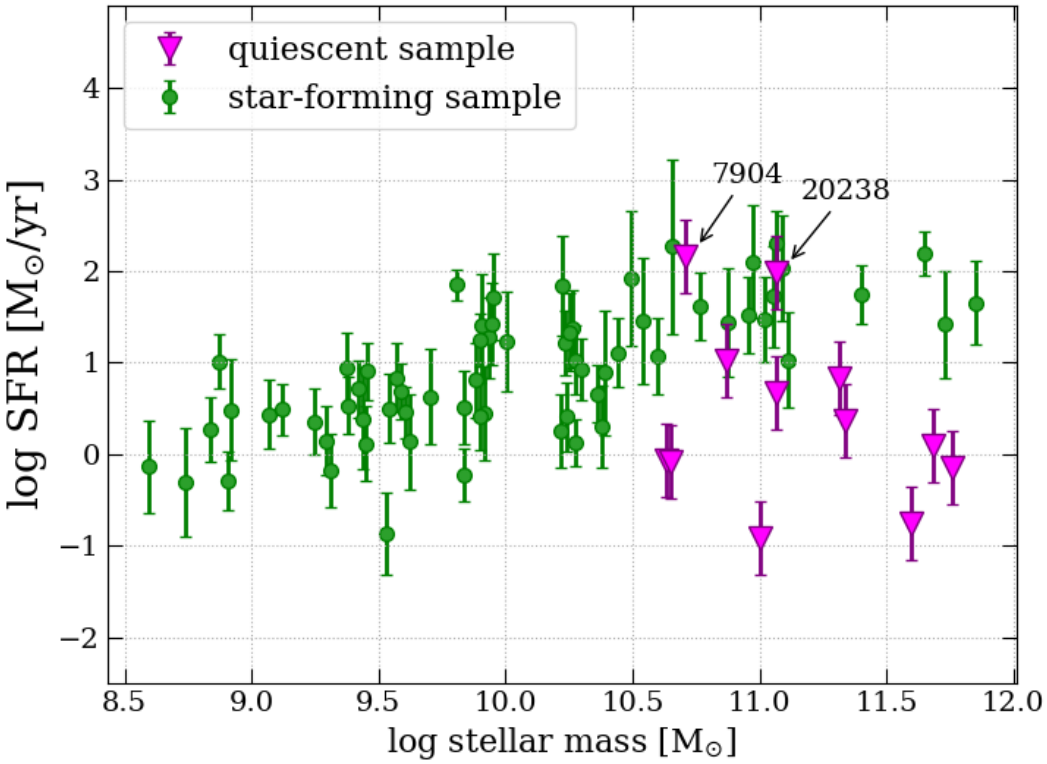

Figure 6.2: *SFR from Hα luminosity as a function of stellar mass for the Blue Jay galaxies: the y-axis value of the magenta points is to be considered an upper limit.*

I have included a mean SFR value of each galaxy in Table 6.1, calculated by averaging the SFR over the last 100 Myr (fifth column). This average value is calculated from the Prospector estimation of the SFH of each object and it is supplied in order to have something to compare the current SFR to: it is important to keep in mind that Prospector computes the SFH as a continuous function between adjacent time bins (Leja, Carnall, Johnson, Conroy, & Speagle, 2019), thus the average SFR value computed in this way is often higher than the real value, particularly in the case of rapid quenching.

Two outliers with very high SFR are visible in Table 6.1: COSMOS-7904, already confirmed to be a star-forming galaxy from the BPT diagrams, and COSMOS-20238, which has a very high V-band extinction of $A_v \sim 6.5$ and SFR = 98±11 $M_\odot$/yr. This latter system is classified as AGN (although straddling the K01 maximum starburst line) by the WHaN diagram, but it lacks any significant [OIII] emission and thus cannot

be classified by the BPT: given the high A_V and SFR values, it is probably a very dusty star-forming galaxy which has contaminated the sample in the UVJ-color selection, and that may harbour an obscured AGN. This is also confirmed by the spectrum, which is quite red but lacks significant absorption lines typical of quiescent galaxies' spectra (see Figure 6.1).

By computing the SFR for the rest of the Blue Jay catalog as well, we can easily compare the two populations and conclude that the sample of galaxies analyzed in this work are indeed quiescent, as they lie below the SFR main sequence traced by the star-forming sample on the stellar mass vs SFR plot in Figure 6.2. This result is even stronger when considering that the plotted values are actually upper limits on the SFR for the quiescent sample.

Thus I have proven that my sample is indeed composed of quiescent galaxies. Given that we found a high incidence of AGN among these galaxies (which would appear as normal quiescent galaxies in absence of a measure of their optical line ratios), this study represents strong evidence of the fact that nuclear activity and quenching of star formation are closely linked together.

ID	BPT class.	A_V	SFR (Hα) [$M_\odot$/yr]	<SFR> (<100Myr) [$M_\odot$/yr]	SNR Hα
7549	Composite	2.477	0.87±0.08	32.1	7.4
7904	SF	3.961	147±11	108.5	9.9
8013	AGN	1.390	0.83±0.05	5.4	25.3
8469	–	0.606	–	4.5	-0.164
9395	–	0.639	≤0.15	5.5	1.5
10128	AGN	4.042	2.35±0.19	1.9	8.3
10339	–	1.303	–	0.8	–
10400	–	0.562	–	0.2	-0.9
10565	RG	1.207	0.12±0.05	0.5	3.1
10592	–	7.306	–	5.2	-1.9
11142	AGN	2.539	4.6±0.5	1.4	22.2
11337	Merger*	7.697	–	13.5	–
11494	RG	0.681	0.70±0.22	2.8	3.6
12332	–	1.670	–	1.9	1.184
16419	AGN	0.197	1.23±0.18	4.8	10.9
17713	–	0.999	≤0.24	0.9	1.5
18668	AGN	2.682	10.6±0.4	82.1	26.4
18688	AGN	1.537	6.90±0.35	10.6	27.3
18977	BL AGN	0.005	0.18±0.04	0.7	41.2
20238	AGN	6.508	98±4	112.9	15.9
21477	–	1.527	≤0.51	2.7	0.1
21541	–	0.063	0.17±0.20	0.2	2.4

Table 6.1: *SFR calculation results. The last column gives the SNR of the Hα line: for galaxies with non-detected lines (SNR<3), only the upper limit on the measured SFR is given. (*Not a classification from the BPT but from the imaging and spectroscopic data)*

Chapter 7

Ionized gas outflows

AGN feedback and its effects on the galactic environment are very complex phenomena that have been linked both to the quenching of star-formation in a galaxy and to starburst events (see Fabian (2012); King and Pounds (2015) for reviews on the subject). AGN activity, anyway, seems to be an important mechanism for star-formation quenching: its negative feedback mechanisms acting on the host galaxy's environment are to blow away gas useful for SF (often referred to as kinetic feedback) and heat the surrounding medium and thus prevent cooling (thermal feedback). Many studies using simulations have shown that AGN activity is essential in reproducing post-starburst populations (e.g., Davis et al., 2019; Pontzen et al., 2017; Zheng et al., 2020). However, it is very challenging to directly observe evidence of the ongoing AGN activity. Galactic outflows have been observed for a number of post-starburst galaxies (e.g., Baron, Netzer, Poznanski, Prochaska, & Förster Schreiber, 2017; Maltby et al., 2019), and given their high speed (> 1000 km/s), the outflows are thought to be driven by ejective AGN feedback (Förster Schreiber et al., 2019). Very recently, Belli et al. (2023) found evidence of AGN activity ejecting neutral gas from an actively quenching galaxy at $z \sim 2$: this system, COSMOS-11142 , is a Blue Jay galaxy also present in my sample and in the next section we will be looking at its outflows in the ionized gas phase.

With a more in-depth spectral fitting of emission lines in the quiescent sample's newly-found AGNs, I will show that we can see and model galaxy-wide *ionized gas outflows* in 4 out of the 22 galaxies of my sample: this finding is made possible by the NIRSpec's sensitivity and it represents a direct observational proof of gas actively leaving the galaxies and contributing to the quenching of star formation in quiescent AGN hosts at Cosmic Noon.

7.1 Line fitting with multiple Gaussian components

As already hinted at in chapter 4, I was not able to successfully fit all of the sample's spectra using a simple, single-Gaussian profile model. In particular, for 4 out of 22 galaxies more than one Gaussian component in the fitting model was needed: this is the case for galaxies COSMOS-8013, 11142, 18668 and 18977, which are all hosts of an AGN (according to the line ratio diagnostics). For each of these objects I realized a more complex fitting model in order to obtain the best fit possible and better constrain the underlying emission. Following the examples of Brusa et al. (2015) and of Übler et al. (2023a), I first considered three different Gaussian components for each line:

1 **Systemic component:** a single Gaussian model with a **narrow** profile centered at the systemic redshift given by the absorption lines. The FWHMs of these lines are fixed to be lower than 550 km/s. The same constraints of wavelength and flux ratios as the previous fit are imposed.

2 **Broad component:** a very broad (FWHM>2000 km/s) Gaussian component fixed at systemic velocity modeled like the first one, but only applied to Hα, Hβ and He I.

3 **Shifted component:** the last component is a third Gaussian free to vary in both FWHM and centroid position. This allows me to fit potential components of the observed emission lines which appear to be blueshifted or redshifted from the galaxy's rest frame. In this case, the line width is NOT imposed equal for each lines but is instead individually fitted. The same constraints on flux and wavelength ratios remain.

The systemic, narrow component should trace lines coming from the central NLR and/or lines coming from SF, if present, or from gas ionized by old stars in the galaxy. The broad component should trace broadening of the lines at systemic velocity due to BLR emission (only in the case of the permitted transitions, i. e. Hα, Hβ and He I). The last component is used to trace outflowing gas, that can be red or blueshifted with respect to the galaxy's systemic velocity, i.e. showing an asymmetric line profile.

However, there is a possible degeneracy present in the BLR vs outflowing component used to fit the Hα and [NII] line region, since the broadening of these lines may be due either to the BLR component given by Hα or by the broad component of all three lines due to outflowing gas. This degeneracy is hard to break using any other observational evidence. The Hβ line is also considered, in order to see if its kinematics is compatible to the one observed for the Hα line, however Hβ is significantly fainter than Hα and thus it is difficult to fit. Also, if indeed there is outflowing gas, this could also be visible in Hβ, bringing us back again to the same outflow/BLR degeneracy.

One important observation to be made, however, is whether outflowing gas is also traced by forbidden emission lines, e. g. by the [OII] doublet or the [OIII] lines: the broadening of these lines cannot be due to the central, BLR emission and so it is only traceable to outflowing, ionized gas. The natural conclusion is that, since we do see outflows traced by other lines, we should also be able to see them traced in the Balmer emission lines, in addition to a possible BLR component.

Of course, this last consideration does not solve the degeneracy in the fit, but can be used as a justification for the use of a simpler fitting model made up of only two Gaussian components, as it is done in Förster Schreiber et al. (2019); Zakamska et al. (2016) and Davies et al. (2020):

1 **Narrow, systemic component** for the host galaxy + central NLR emission, whose velocity dispersion is fixed to be the same for all lines;

2 **Broad component** for the outflows and/or BLR, free to vary in redshift: in this case, I chose to not fix the velocity dispersion as the same throughout all broad components. This is firstly because this component could be tracing BL emission in one line but outflows in another, secondly because even considering

only outflows, many studies have found that differently-ionized gas components show different outflows velocities.

Eventually, this is the method that was applied to model the emission lines, since it requires fewer parameters for the modeling and the least-square fitting is more likely to succeed.

7.2 Results of the spectral fitting

Table 7.1 summarizes the outflows properties measured in the subsample of 4 galaxies: the relative outflow velocity (v_{out}) has been calculated using the standard definition

$$v_{out} = |\Delta v| + 2 \cdot \sigma_{out}, \tag{7.1}$$

where $|\Delta v|$ is the difference between the central wavelength of the outflow and the galactic rest-frame wavelength of the line expressed in km/s and σ_{out} is the outflow's velocity dispersion.

We can immediately notice a wide difference in velocity dispersion of the broad component under the permitted lines in 18977, which is a BL AGN and shows a broadening of Hα, Hβ and He I with σ of the order of $\sim$ 4000 km/s, as opposed to the observed values in the hundreds of km/s observed in the rest of the systems. Of course, it is logical to assume that a fraction of the observed broad component in the permitted lines of COSMOS-18977 is actually due to outflowing gas rater than to the BLR: this is also supported by the fact that we do see outflows in the forbidden oxygen lines of the same galaxy, however our fitting model is not able to successfully resolve these two components in the line profile.

Figures 7.1, 7.2, 7.3 and 7.4 show the two Gaussian components fits for every fitted line in each galaxy spectrum. As we can see, the [OII] doublet is highly asymmetric in all spectra, and to a lesser degree the [OIII] lines are as well. The blueshifted excess that we measure in these lines means that our line of sight is intercepting ionized gas that is actively being ejected from the galaxy in our direction. The redshifted half of the outflow, ejected in the opposite direction with respect to us, is not seen in the lines because it is attenuated by the dust in the galaxy.

The [NII]/Hα line compound is slightly broad in 8013, 11142 and 18688. I have fitted an outflowing component under these lines in these galaxies instead of looking for a BLR-like component under Hα: this is because I have the example of the actual BL AGN COSMOS-18977, in which we can see how extreme the Hα broadening is with respect to the narrow lines. Since nothing of this magnitude is seen in the other systems and there is already evidence of outflowing gas coming from the forbidden oxygen lines, I make an assumption that the broadening of the [NII]-Hα complex is also traceable to emission coming from outflowing material.

A separate case has to be made for the He I λ10830 emission line fit in COSMOS-18977 (lower central panel in fig. 7.4). Since this is a permitted line, the same broad profile found under Hα and Hβ was also fitted here: however, in order to reproduce the observed profile I found that the broad component had to be *redshifted* with respect to the galaxy rest-frame He I line. This is a phenomenon called *resonant scattering* and it is often found in observations of the Lyα line, where the emitted photons are

	COSMOS-8013			COSMOS-18668		
line	Δv	σ	v_{out}	Δv	σ	v_{out}
[OII]	-260±174	731±171	1722±384	-213±90	668±100	1548±211
Hβ	–	–	–	-303±59	800±160	1903±325
[OIII]	-604±72	1103±220	2809±446	-303±59	800±160	1903±325
Hα	-172±57	441±220	1055±444	-283±45	694±220	1670±442
[NII]	-172±57	441±220	1055±444	-283±45	694±220	1670±442
[SII]	–	–	–	–	–	–
He I	–	–	–	–	–	–
	COSMOS-11142			COSMOS-18977		
line	Δv	σ	v_{out}	Δv	σ	v_{out}
[OII]	-595±84	164±116	923±246	-1231±372	1060±314	3350±730
Hβ	–	–	–	0 (fixed)	4115±113†	–
[OIII]	-533±56	694±159	1921±323	0±79	400±92	800±200
Hα	-45±44	582±220	1209±442	0 (fixed)	4115±113†	–
[NII]	-45±44	582±220	1209±442	–	–	–
[SII]	–	–	–	–	–	–
He I	–	–	–	1444±54	4115±113†	–

Table 7.1: *Outflow velocity relative to the galaxy rest-frame and velocity dispersion of the broad components fitted in each emission line for COSMOS-8013, 18668, 11142 and 18977. Everything is given in units of km/s. Missing entries were not successfully fitted. (†Not outflowing gas but the BLR's emission).*

then re-absorbed by the neutral hydrogen in the galaxy unless they are substantially redshifted. Since the He I transition involves a meta-stable level of the helium atom, it can give rise to the same effect, with the difference that the He I line traces gas that is ionized, and not neutral. This behaviour is discussed in Belli et al. (2023).

7.3 Physical nature of the outflows

The evidence demonstrates that ionized gas is actively leaving these galaxies with velocities of the order of thousands of km/s. In all of these systems, the SFR is too low to be able to justify star-formation driven outflows. We can also rule out a star-formation driven fossil outflow since the ionized gas velocity we measure is substantially higher than what observed in the most powerful star-formation driven outflows at z $\sim$ 2 (Davies et al., 2019). One possible scenario could be that the outflowing gas consists of tidally ejected material due to a major merger, but the lack of any tidal features visible in the near-IR imaging data (as visible in the lower right panels of Figures 7.1,7.2,7.3 and 7.4) rules out this possibility.

Given that we know from the analysis of the line ratios carried out in Chapter 5 that these galaxies all host an active nucleus, the only reasonable origin of the observed outflows is AGN feedback. This constitutes observational evidence of the negative action of AGN feedback on star-formation, since we are seeing gas actively leaving these already gas-poor, quiescent systems. Thus, we can link the observation of powerful ionized gas outflows observed in quiescent galaxies at z $\sim$ 2 to their AGN activity and conclude that the main mechanism responsible for the quenching of star-formation in

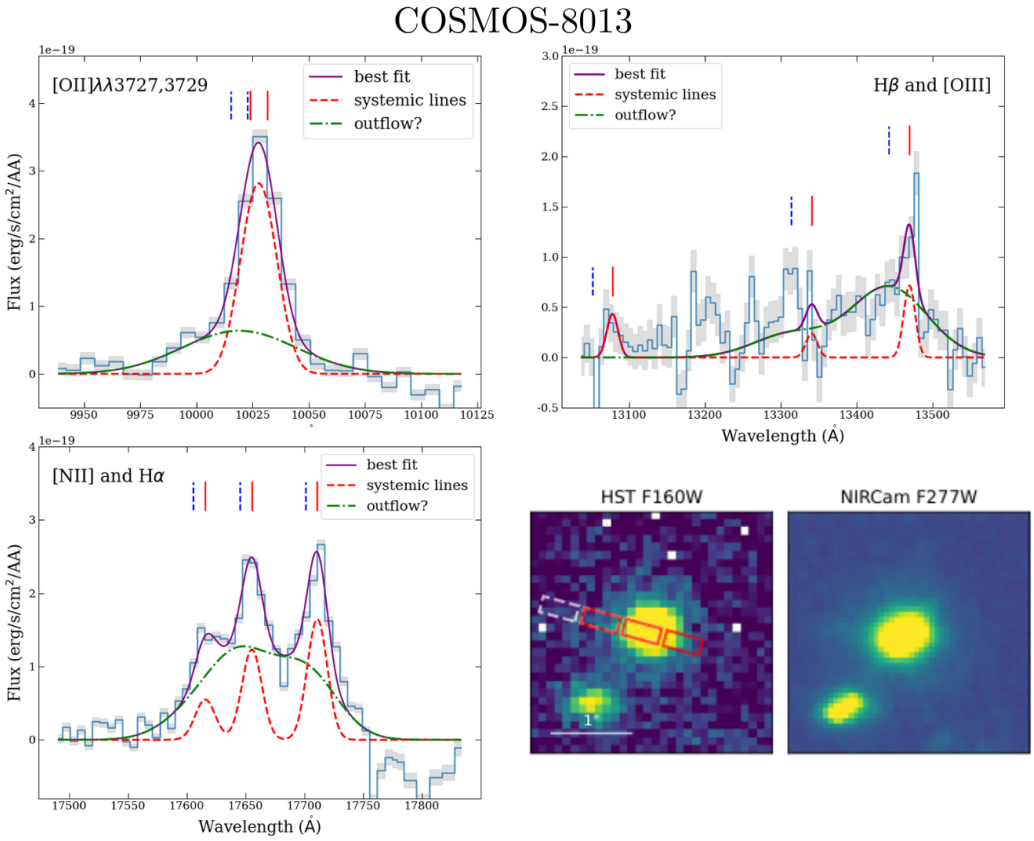

Figure 7.1: *Multiple components line fitting in galaxy 8013. On the lower right, the HST imaging data and JWST's NIRCam images of the galaxy, as seen in ch. 3.*

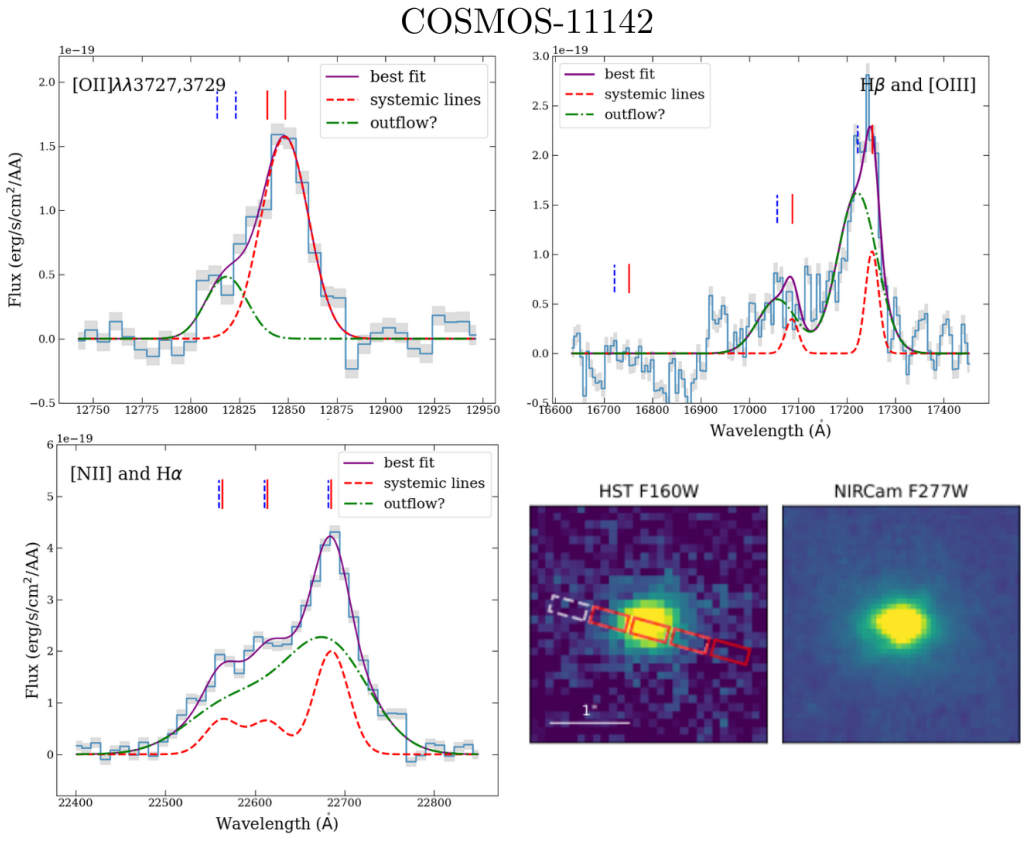

Figure 7.2: *Multiple components line fitting in galaxy 11142 + imaging data (as above)*

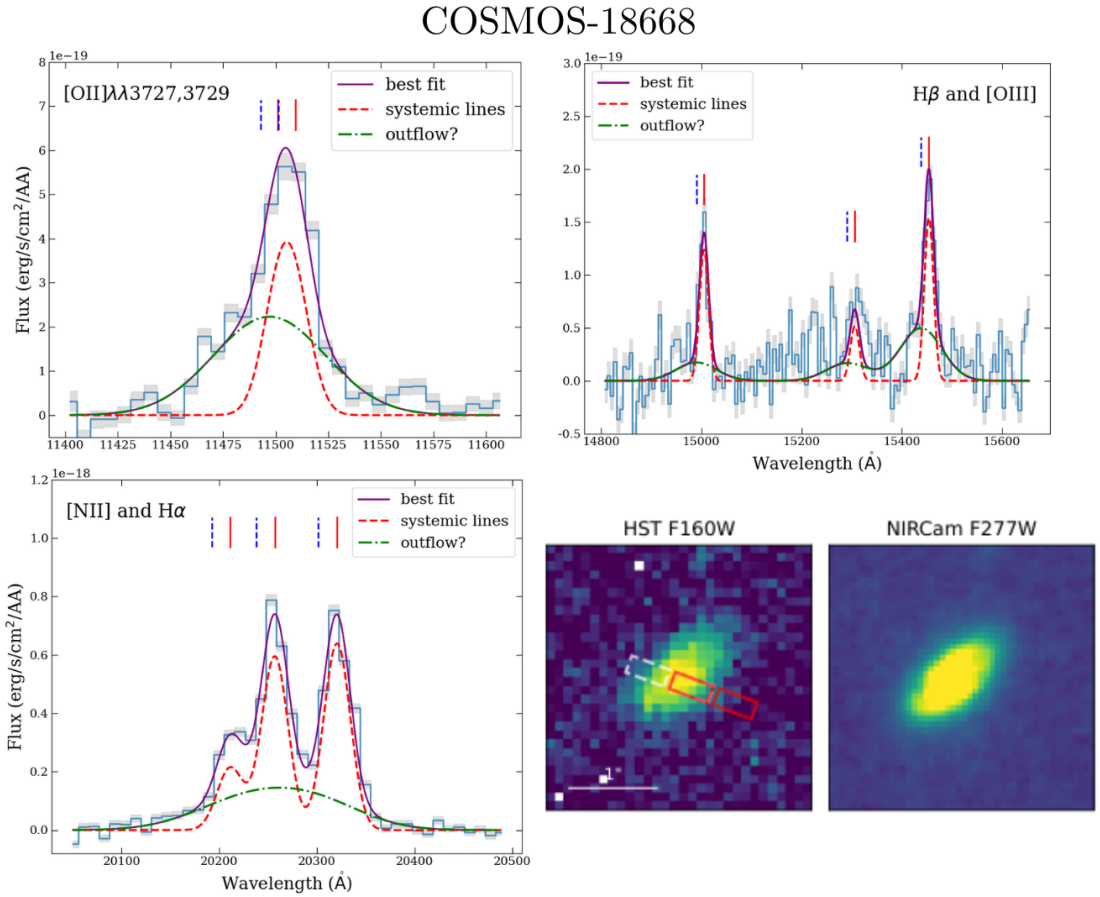

Figure 7.3: *Multiple components line fitting in galaxy 18668 + imaging data (as above)*

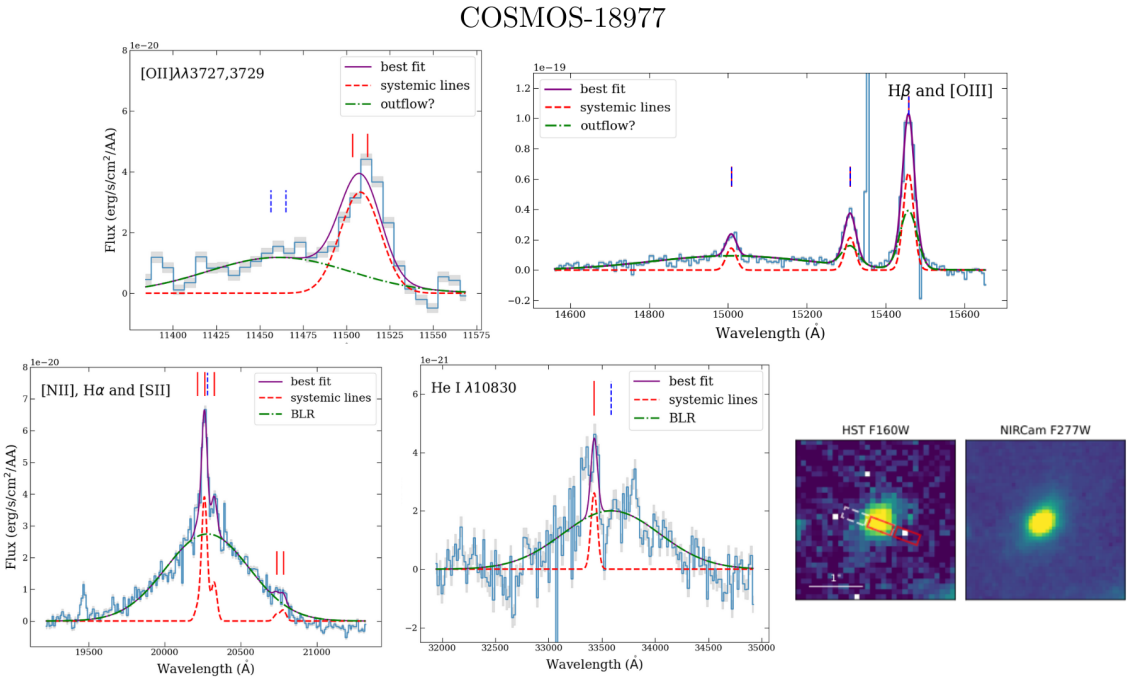

Figure 7.4: *Multiple components line fitting in galaxy 18977 + imaging data (as above)*

these systems at Cosmic Noon is likely to be AGN feedback.

Of course, in order to securely relate the observed outflows to the quenching of star formation in a galaxy we would need to get measurements on the mass outflow rate, defined as the rate of gas mass leaving the galaxy in $M_\odot$/yr, and compare it to the galaxy's star formation history, but this kind of analysis goes beyond the scope of this thesis. However, this exact in-depth assessment on the mechanisms of quenching has been carried out by Belli et al. (2023) on one particular object in my sample, i.e. COSMOS-11142. This galaxy, in fact, shows not only powerful outflows in the ionized gas phase, but also in the neutral one, measured from blueshifted Na I D $\lambda\lambda 5892, 5898$ and Ca II K $\lambda 3935$ lines seen in *absorption*. As shown in that study, even though the mass outflow rate of the ionized gas phase compared to the galaxy's SFH is not sufficient to explain the quenching of star formation, the outflow mass rate calculated from the neutral phase is.

As visible from the SFH plot in Figure 7.5 (taken from Belli et al., 2023), COSMOS-11142 is clearly a post-starburst galaxy: it formed most of its stellar mass in a rapid and powerful starburst $\sim$ 300 Myr before the observations, and then experienced a rapid quenching of the star formation rate by two orders of magnitude on a remarkably short time scale. The mass outflow rate calculated from ionized gas phase is comparable, if slightly lower, to the current star formation rate and not able to fully justify the sudden quenching of 11142. The mass outflow rate for the neutral gas, however, is substantially higher than the residual SFR, implying that the outflow is able to strongly suppress the star formation activity and quench the galaxy.

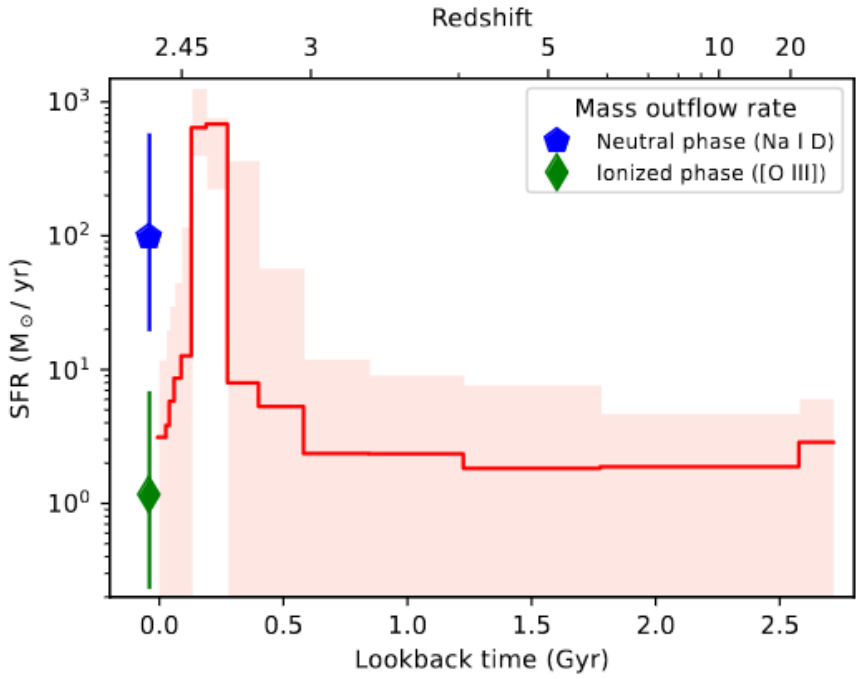

Figure 7.5: *Star formation history for COSMOS-11142 (red line) and 95% credible region (shaded area). The mass outflow rate is shown for neutral and ionized gas at a lookback time of zero (i.e., the epoch at which the galaxy is observed). From Belli et al. (2023).*

Chapter 8

Conclusions and future prospects

This last chapter is dedicated to summarizing the main results of my thesis and to explore the many follow-up possibilities on the findings of this work.

The data analyzed have been taken from the Blue Jay survey, a medium-sized Cycle 1 JWST program which observed ~ 150 galaxies at redshift $1.7 < z < 3.5$ with NIRSpec, between 1-5 μm. A sample of 22 massive quiescent galaxies have been selected from the parent catalog using rest-frame UVJ color-selection criteria and limiting the sample to objects with stellar mass $M_* > 10^{10}$ $M_\odot$.

Subsequently, the sample's spectra were continuum-fitted using the `Propector` SPS code in order to subtract the stellar emission and isolate the contribution due to gas. Several rest-frame optical emission lines from ionized gas were found and fitted using single Gaussian profiles, estimating their fluxes, velocity dispersion and redshift. Using the fluxes calculated this way, I was able to construct several line ratios diagnostic diagrams, such as the BPT diagram, and investigate the underlying source of excitation behind the observed emission lines.

From emission line ratios diagrams it was found that at least **8** out of the 22 galaxies of the sample are harbouring an active nucleus in their center, with one of the 8 objects spectroscopically confirmed to be a BL AGN. In order to further confirm that the observed emission lines are not actually due to hidden star-formation and validate the quiescent nature of the sample as well as the diagnostic diagrams' results, I measured the current SFR of each galaxy from Hα line luminosity and confirmed that most of the sample is indeed quiescent.

Lastly, it was noted that the original single-Gaussian fitting was not able to completely reproduced the observed emission in 4 of the BPT-confirmed AGNs in my sample, but a multiple Gaussian components model was needed instead. This more complex spectral fitting found evidence of powerful ionized gas outflows actively leaving these galaxies with velocities of $v_{out} \sim 1000$ km/s: the most logical explanation for the origin of these outflows is AGN activity and feedback.

These are the main scientific findings of this thesis:

Quiescent galaxies selection through rest-frame UVJ colors

Although the selection criteria that were employed to derive the quiescent sample analyzed in this work were deliberately relaxed with respect to the classic ones used in literature, in order to include actively quenching massive galaxies, the general picture that comes out from the SFR calculation step is that rest-frame UVJ colors are a

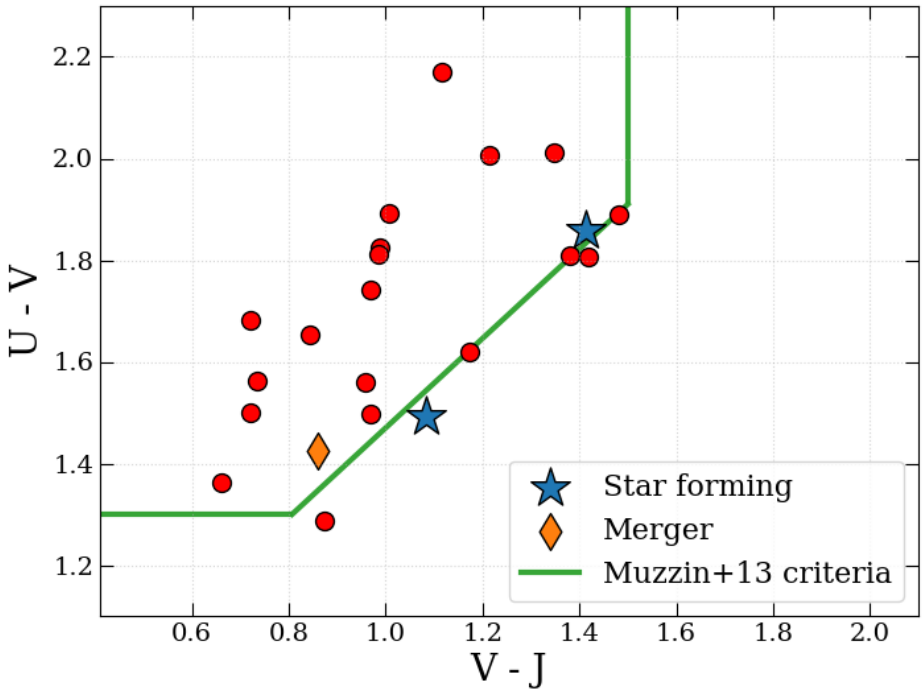

Figure 8.1: *Quiescent sample used in this work and their final classification: two star-forming and one merger contaminants were found.*

valid tool to select quiescent galaxies at least up to z $\sim$ 3.5, as already found by many previous studies.

Two star-forming galaxies were found within the sample, COSMOS-7904 and COSMOS-20238, respectively having SFR(Hα) = 147 ± 11 and 98 ± 4 $M_{\odot}$/yr, and a merger whose exact star formation rate I was not able to derive because the Hα emission line in its spectrum falls in a detector gap. These contaminants represent 13% of my sample, which is a low percentage considering that a more relaxed selection criteria was applied. In fact, as visible in Figure 8.1 only one of the star-forming galaxies actually falls inside the stricter Muzzin et al. (2013) selection criteria, reiterating the validity of this method as a way of selecting quiescent populations at Cosmic Noon.

AGN activity in massive quiescent hosts at Cosmic Noon

The main result of this work consists in the discovery of a population of never-before-detected low-luminosity AGNs at z $\sim$ 2 found among a sample of apparently non-active massive quiescent galaxies. The great sensitivity of JWST's NIRSpec observations in the near-IR has enabled the detection of weak ionized gas emission lines in the spectra of these galaxies that would have been otherwise missed by ground-based observation. This, in turn, made it possible to classify the sample using line ratio diagnostic diagrams, to then find out that most of the quiescent systems with detected emission lines are actually harboring an active nucleus in their center.

The high number of AGN discovered in this relatively small sample at z $\sim$ 2 (36% of the whole quiescent population, 67% of the BPT-classified sample) indicates that many quiescent galaxies at Cosmic Noon may actually harbour low-luminosity active

nuclei that have remained up until now undetected.

Ionized gas outflows in quiescent galaxies and star formation quenching

Powerful outflows of ionized gas actively leaving these passive gas-poor systems at velocities of thousands of km/s were identified through the emission lines of a subsample of 4 out of 22 galaxies. These ionized gas outflows were all found in systems classified as AGN and constitute observational proof of the quenching of star formation through gas ejection. The fact that all of these objects are confirmed AGNs and that no other mechanism is able to explain such fast galaxy-wide outflows is an important piece of evidence that points to AGN activity and feedback as the main star-formation quenching mechanism responsible for the "death" of massive galaxies observed at Cosmic Noon.

The special case of galaxy COSMOS-11142, belonging to my sample, represents the first direct observational evidence of AGN feedback actively quenching star formation in a galaxy at z=2.445 through the observation of outflows both in the ionized and in the neutral gas phase, as illustrated by Belli et al. (2023). It is reasonable to assume that such neutral gas outflows are present (in a weaker form) also in the other galaxies in which I detected ionized gas outflows. The ionized outflows may thus be crucial to understand quenching: even if their mass outflow rates are too low to affect the host galaxy, they may represent a signpost for the presence of stronger, yet harder to detect, neutral outflows.

8.1 Future prospects

The results of this thesis work are surely exciting: it remains, however, much work to be done.

Spectral fitting

The fitting of the emission lines could be improved by implementing a full-spectrum fitting code that fits all lines together and not separately, as was done for this thesis. Also, a higher number of emission lines could be searched for and fitted, including for example lines from the Paschen series. Even if very weak or not detected, these additional lines could help in constraining measured properties of the galaxies in my sample.

Classification through line diagnostic diagrams

Line ratio diagnostic diagrams are a valid tool for investigating the origin of ionizing emission in a galaxy, but they are fundamentally empirical means of classification calibrated on present-day galaxies: thus, some caution must be exercised when applying them to the high-redshift universe. We have briefly touched upon the effect of metallicity, α-enhancement and galaxy evolution in changing the location of galaxies on the diagram (ch. 5), and we have concluded that our results hold even after considering all of these effects.

The question of gas ionization by shocks, however, has been mentioned but not accurately explored, since according to numerical models (Allen, Groves, Dopita, Sutherland, & Kewley, 2008b), shock-ionization systems can occupy the same regions of

AGN-photoionization ones in the BPT and other diagnostic diagrams, with very little hope of successfully separating the two components.

The same reasoning that we have applied in investigating the origin of observed gas outflows, anyway, can also be applied in this case: even if the main source of ionization for gas in these galaxies were to be shocks and not AGN radiation field, the measured SFRs are way too low to be able to trace the origin of these galaxy-wide shocks back to star formation and none of the typical features of mergers have been observed as well. This means that the only mechanism capable of generating shocks that would be able to produce the observed emission line is AGN feedback, thus coming back again to the initial hypothesis of an active nucleus origin to the excitation of the observed emission lines.

It still remains to be determined how much the photoionizing flux of an evolved stellar population is effective in exciting ionized gas emission lines in massive quiescent galaxies at z $\sim$ 2. Scarce literature exists on simulations of EUV flux in cosmic-noon galaxies emitted by old stars: it would be interesting to get simulated data produced using photoionization codes such as CLOUDY for these systems in order to try and understand whether the emission lines observed in weak line galaxies, for which no BPT classification was possible, can be produced by evolved stars only. This would be particularly useful so as to redefine the WHaN diagram classification of *retired galaxies* to work in the high-redshift Universe.

The search for direct evidence of AGN-induced quenching in massive quiescent galaxies

We have empirically linked the presence of an AGN in most of the (BPT-detected) galaxies in the sample to the evolution of these systems from star-forming to quiescent through AGN feedback-induced quenching. The ionized gas outflows observed in a selected few of these galaxies and analyzed in chapter 7 constitutes strong evidence in support of this scenario.

It still remains to be assessed, however, how much impact do these outflows have on the wider galaxy environment through the calculation of the mass outflow rates and the comparison with the galaxy's recent star formation history, as was done in Belli et al. (2023). In addition, we should be able to get the full picture on the entity and nature of these outflows by investigating the neutral and cold gas phase, which is the one that constitutes most of the ISM's gas mass: this could be done by further investigating neutral gas visible through optical absorption lines, as was done for COSMOS-11142, and/or by obtaining mm/sub-mm observations of this sample in order to investigate the molecular phase of the outflows.

References

Allen, M. G., Groves, B. A., Dopita, M. A., Sutherland, R. S., & Kewley, L. J. (2008a, September). The MAPPINGS III Library of Fast Radiative Shock Models. *ApJS*, *178*(1), 20-55. doi: 10.1086/589652

Allen, M. G., Groves, B. A., Dopita, M. A., Sutherland, R. S., & Kewley, L. J. (2008b, September). The MAPPINGS III Library of Fast Radiative Shock Models. *ApJS*, *178*(1), 20-55. doi: 10.1086/589652

Antwi-Danso, J., Papovich, C., Leja, J., Marchesini, D., Marsan, Z. C., Martis, N. S., ... Tran, K.-V. H. (2023, February). Beyond UVJ: Color Selection of Galaxies in the JWST Era. *ApJ*, *943*(2), 166. doi: 10.3847/1538-4357/aca294

Arimoto, N., & Yoshii, Y. (1987, February). Chemical and photometric properties of a galactic wind model for elliptical galaxies. *A & A*, *173*, 23-38.

Baldwin, J. A., Phillips, M. M., & Terlevich, R. (1981, February). Classification parameters for the emission-line spectra of extragalactic objects. *PASP*, *93*, 5-19. doi: 10.1086/130766

Balogh, M. L., Baldry, I. K., Nichol, R., Miller, C., Bower, R., & Glazebrook, K. (2004, November). The Bimodal Galaxy Color Distribution: Dependence on Luminosity and Environment. *ApJL*, *615*(2), L101-L104. doi: 10.1086/426079

Baron, D., Netzer, H., Poznanski, D., Prochaska, J. X., & Förster Schreiber, N. M. (2017, September). Evidence of ongoing AGN-driven feedback in a quiescent post-starburst E+A galaxy. *MNRAS*, *470*(2), 1687-1702. doi: 10.1093/mnras/stx1329

Bell, E. F., Wolf, C., Meisenheimer, K., Rix, H.-W., Borch, A., Dye, S., ... McIntosh, D. H. (2004, June). Nearly 5000 Distant Early-Type Galaxies in COMBO-17: A Red Sequence and Its Evolution since z~1. *ApJ*, *608*(2), 752-767. doi: 10.1086/420778

Belli, S., Genzel, R., Förster Schreiber, N. M., Wisnioski, E., Wilman, D. J., Wuyts, S., ... van Dokkum, P. (2017, May). KMOS^{3D} Reveals Low-level Star Formation Activity in Massive Quiescent Galaxies at $0.7 < z < 2.7$. *ApJL*, *841*(1), L6. doi: 10.3847/2041-8213/aa70e5

Belli, S., Newman, A. B., & Ellis, R. S. (2019, March). MOSFIRE Spectroscopy of

Quiescent Galaxies at 1.5 < z < 2.5. II. Star Formation Histories and Galaxy Quenching. *ApJ*, *874*(1), 17. doi: 10.3847/1538-4357/ab07af

Belli, S., Park, M., Davies, R. L., Mendel, J. T., Johnson, B. D., Conroy, C., ... Weinberger, R. (2023, August). Massive and Multiphase Gas Outflow in a Quenching Galaxy at z=2.445. *arXiv e-prints*, arXiv:2308.05795. doi: 10.48550/arXiv.2308.05795

Bertola, F., Buson, L. M., & Zeilinger, W. W. (1992, December). The External Origin of the Gas in S0 Galaxies. *ApJl*, *401*, L79. doi: 10.1086/186675

Binette, L., Magris, C. G., Stasińska, G., & Bruzual, A. G. (1994, December). Photoionization in elliptical galaxies by old stars. *A & A*, *292*, 13-19.

Blanton, M. R., & Moustakas, J. (2009, September). Physical Properties and Environments of Nearby Galaxies. *ARA & A*, *47*(1), 159-210. doi: 10.1146/annurev-astro-082708-101734

Blumenthal, G. R., Faber, S. M., Primack, J. R., & Rees, M. J. (1984, October). Formation of galaxies and large-scale structure with cold dark matter. *Nat*, *311*, 517-525. doi: 10.1038/311517a0

Böker, T., Arribas, S., Lützgendorf, N., Alves de Oliveira, C., Beck, T. L., Birkmann, S., ... Zeidler, P. (2022, May). The Near-Infrared Spectrograph (NIRSpec) on the James Webb Space Telescope. III. Integral-field spectroscopy. *A & A*, *661*, A82. doi: 10.1051/0004-6361/202142589

Böker, T., Beck, T. L., Birkmann, S. M., Giardino, G., Keyes, C., Kumari, N., ... Willott, C. J. (2023, March). In-orbit Performance of the Near-infrared Spectrograph NIRSpec on the James Webb Space Telescope. *PASP*, *135*(1045), 038001. doi: 10.1088/1538-3873/acb846

Brammer, G. B., van Dokkum, P. G., Franx, M., Fumagalli, M., Patel, S., Rix, H.-W., ... Williams, A. (2012, June). 3D-HST: A Wide-field Grism Spectroscopic Survey with the Hubble Space Telescope. *ApJS*, *200*(2), 13. doi: 10.1088/0067-0049/200/2/13

Brammer, G. B., Whitaker, K. E., van Dokkum, P. G., Marchesini, D., Labbé, I., Franx, M., ... Rudnick, G. (2009, November). The Dead Sequence: A Clear Bimodality in Galaxy Colors from z = 0 to z = 2.5. *ApJL*, *706*(1), L173-L177. doi: 10.1088/0004-637X/706/1/L173

Bressan, A., Chiosi, C., & Fagotto, F. (1994, September). Spectrophotometric Evolution of Elliptical Galaxies. I. Ultraviolet Excess and Color-Magnitude-Redshift Relations. *ApJS*, *94*, 63. doi: 10.1086/192073

Brinchmann, J., Charlot, S., White, S. D. M., Tremonti, C., Kauffmann, G., Heckman, T., & Brinkmann, J. (2004, July). The physical properties of star-forming galaxies

in the low-redshift Universe. *MNRAS*, *351*(4), 1151-1179. doi: 10.1111/j.1365-2966.2004.07881.x

Brusa, M., Bongiorno, A., Cresci, G., Perna, M., Marconi, A., Mainieri, V., ... Zamorani, G. (2015, January). X-shooter reveals powerful outflows in z $\sim$ 1.5 X-ray selected obscured quasi-stellar objects. *mnras*, *446*(3), 2394-2417. doi: 10.1093/mnras/stu2117

Buson, L. M., Sadler, E. M., Zeilinger, W. W., Bertin, G., Bertola, F., Danzinger, J., ... de Zeeuw, P. T. (1993, December). Tghe distribution of ionized gas in early-type galaxies. *A & A*, *280*, 409-425.

Byler, N., Dalcanton, J. J., Conroy, C., Johnson, B. D., Choi, J., Dotter, A., & Rosenfield, P. (2019, July). Self-consistent Predictions for LIER-like Emission Lines from Post-AGB Stars. *AJ*, *158*(1), 2. doi: 10.3847/1538-3881/ab1b70

Calabrò, A., Pentericci, L., Feltre, A., Arrabal Haro, P., Radovich, M., Seillé, L. M., ... Vulcani, B. (2023, June). Near-infrared emission line diagnostics for AGN from the local Universe to redshift 3. *arXiv e-prints*, arXiv:2306.08605. doi: 10.48550/arXiv.2306.08605

Calzetti, D. (1999, January). UV Emission and bust properties of high redshift galaxies. *Apss*, *266*, 243-253. doi: 10.48550/arXiv.astro-ph/9902107

Calzetti, D., Armus, L., Bohlin, R. C., Kinney, A. L., Koornneef, J., & Storchi-Bergmann, T. (2000, April). The Dust Content and Opacity of Actively Star-forming Galaxies. *ApJ*, *533*(2), 682-695. doi: 10.1086/308692

Cappelluti, N., Brusa, M., Hasinger, G., Comastri, A., Zamorani, G., Finoguenov, A., ... Urry, C. M. (2009, April). The XMM-Newton wide-field survey in the COSMOS field. The point-like X-ray source catalogue. *A & A*, *497*(2), 635-648. doi: 10.1051/0004-6361/200810794

Carnall, A. C., McLure, R. J., Dunlop, J. S., McLeod, D. J., Wild, V., Cullen, F., ... Walker, S. (2023, July). A massive quiescent galaxy at redshift 4.658. *Nature*, *619*(7971), 716-719. doi: 10.1038/s41586-023-06158-6

Chabrier, G. (2003, July). Galactic Stellar and Substellar Initial Mass Function. *PASP*, *115*(809), 763-795. doi: 10.1086/376392

Charlot, S., & Fall, S. M. (2000, August). A Simple Model for the Absorption of Starlight by Dust in Galaxies. *ApJ*, *539*(2), 718-731. doi: 10.1086/309250

Cid Fernandes, R., Stasińska, G., Mateus, A., & Vale Asari, N. (2011, May). A comprehensive classification of galaxies in the Sloan Digital Sky Survey: how to tell true from fake AGN? *MNRAS*, *413*(3), 1687-1699. doi: 10.1111/j.1365-2966.2011.18244.x

Cid Fernandes, R., Stasińska, G., Schlickmann, M. S., Mateus, A., Vale Asari, N., Schoenell, W., & Sodré, L. (2010, April). Alternative diagnostic diagrams and the 'forgotten' population of weak line galaxies in the SDSS. *MNRAS*, *403*(2), 1036-1053. doi: 10.1111/j.1365-2966.2009.16185.x

Cimatti, A., Fraternali, F., & Nipoti, C. (2019). *Introduction to Galaxy Formation and Evolution: From Primordial Gas to Present-Day Galaxies.*

Civano, F., Marchesi, S., Comastri, A., Urry, M. C., Elvis, M., Cappelluti, N., ... Vignali, C. (2016, March). The Chandra Cosmos Legacy Survey: Overview and Point Source Catalog. *ApJ*, *819*(1), 62. doi: 10.3847/0004-637X/819/1/62

Conroy, C., Gunn, J. E., & White, M. (2009, July). The Propagation of Uncertainties in Stellar Population Synthesis Modeling. I. The Relevance of Uncertain Aspects of Stellar Evolution and the Initial Mass Function to the Derived Physical Properties of Galaxies. *ApJ*, *699*(1), 486-506. doi: 10.1088/0004-637X/699/1/486

Contreras, J. W., & Lightsey, P. A. (2004, October). Optical design and analysis of the James Webb Space Telescope: optical telescope element. In J. M. Sasian, R. J. Koshel, P. K. Manhart, & R. C. Juergens (Eds.), *Novel optical systems design and optimization vii* (Vol. 5524, p. 30-41). doi: 10.1117/12.559871

Davies, R. L., Förster Schreiber, N. M., Lutz, D., Genzel, R., Belli, S., Shimizu, T. T., ... Wuyts, S. (2020, May). From Nuclear to Circumgalactic: Zooming in on AGN-driven Outflows at z $\sim$ 2.2 with SINFONI. *ApJ*, *894*(1), 28. doi: 10.3847/1538-4357/ab86ad

Davies, R. L., Förster Schreiber, N. M., Übler, H., Genzel, R., Lutz, D., Renzini, A., ... Wuyts, S. (2019, March). Kiloparsec Scale Properties of Star Formation Driven Outflows at z $\sim$ 2.3 in the SINS/zC-SINF AO Survey. *ApJ*, *873*(2), 122. doi: 10.3847/1538-4357/ab06f1

Davis, T. A., van de Voort, F., Rowlands, K., McAlpine, S., Wild, V., & Crain, R. A. (2019, April). Evolution of the cold gas properties of simulated post-starburst galaxies. *MNRAS*, *484*(2), 2447-2461. doi: 10.1093/mnras/stz180

di Serego Alighieri, S., Trinchieri, G., & Brocato, E. (1990, January). Hα Imaging of X-Ray Luminous Early-Type Galaxies: Clues on the Hot, Warm and Cold Phases of the ISM. In G. Fabbiano, J. S. Gallagher, & A. Renzini (Eds.), *Windows on galaxies* (Vol. 160, p. 301). doi: 10.1007/978-94-009-0543-6_39

Dopita, M. A., & Sutherland, R. S. (1995, December). Spectral Signatures of Fast Shocks. II. Optical Diagnostic Diagrams. *ApJ*, *455*, 468. doi: 10.1086/176596

Dopita, M. A., & Sutherland, R. S. (2003). *Astrophysics of the diffuse universe.*

Dopita, M. A., Sutherland, R. S., Nicholls, D. C., Kewley, L. J., & Vogt, F. P. A. (2013, September). New Strong-line Abundance Diagnostics for H II Regions:

Effects of κ-distributed Electron Energies and New Atomic Data. *ApJS*, *208*(1), 10. doi: 10.1088/0067-0049/208/1/10

Doyon, R., Hutchings, J. B., Beaulieu, M., Albert, L., Lafrenière, D., Willott, C., ... Sawicki, M. (2012, September). The JWST Fine Guidance Sensor (FGS) and Near-Infrared Imager and Slitless Spectrograph (NIRISS). In M. C. Clampin, G. G. Fazio, H. A. MacEwen, & J. Oschmann Jacobus M. (Eds.), *Space telescopes and instrumentation 2012: Optical, infrared, and millimeter wave* (Vol. 8442, p. 84422R). doi: 10.1117/12.926578

Doyon, R., Willott, C. J., Hutchings, J. B., Sivaramakrishnan, A., Albert, L., Lafreniere, D., ... Sawicki, M. (2023, June). The Near Infrared Imager and Slitless Spectrograph for the James Webb Space Telescope – I. Instrument Overview and in-Flight Performance. *arXiv e-prints*, arXiv:2306.03277. doi: 10.48550/arXiv.2306.03277

Dunlop, J. S., Abraham, R. G., Ashby, M. L. N., Bagley, M., Best, P. N., Bongiorno, A., ... van der Werf, P. (2021, March). *PRIMER: Public Release IMaging for Extragalactic Research.* JWST Proposal. Cycle 1, ID. #1837.

Earl, N., Tollerud, E., O'Steen, R., brechmos, Kerzendorf, W., Busko, I., ... Ferguson, H. (2023, June). *astropy/specutils: v1.11.0.* Zenodo. Retrieved from https://doi.org/10.5281/zenodo.8049033 doi: 10.5281/zenodo.8049033

Eracleous, M., Livio, M., & Binette, L. (1995, May). A Duty Cycle Hypothesis for the Central Engines of LINERs. *ApJL*, *445*, L1. doi: 10.1086/187875

Fabian, A. C. (2012, September). Observational Evidence of Active Galactic Nuclei Feedback. *ARA & A*, *50*, 455-489. doi: 10.1146/annurev-astro-081811-125521

Feltre, A., Charlot, S., & Gutkin, J. (2016, March). Nuclear activity versus star formation: emission-line diagnostics at ultraviolet and optical wavelengths. *MNRAS*, *456*(3), 3354-3374. doi: 10.1093/mnras/stv2794

Ferland, G. J., Porter, R. L., van Hoof, P. A. M., Williams, R. J. R., Abel, N. P., Lykins, M. L., ... Stancil, P. C. (2013, April). The 2013 Release of Cloudy. *Revista Mexicana de Astronomía y Astrofísica*, *49*, 137-163. doi: 10.48550/arXiv.1302.4485

Ferruit, P., Jakobsen, P., Giardino, G., Rawle, T., Alves de Oliveira, C., Arribas, S., ... Zeidler, P. (2022, May). The Near-Infrared Spectrograph (NIRSpec) on the James Webb Space Telescope. II. Multi-object spectroscopy (MOS). *A & A*, *661*, A81. doi: 10.1051/0004-6361/202142673

Förster Schreiber, N. M., Übler, H., Davies, R. L., Genzel, R., Wisnioski, E., Belli, S., ... Wuyts, S. (2019, April). The KMOS^{3D} Survey: Demographics and Properties of Galactic Outflows at z = 0.6-2.7. *ApJ*, *875*(1), 21. doi: 10.3847/1538-4357/ab0ca2

Förster Schreiber, N. M., & Wuyts, S. (2020, August). Star-Forming Galaxies at Cosmic Noon. *ARAA*, *58*, 661-725. doi: 10.1146/annurev-astro-032620-021910

Gardner, J. P., Mather, J. C., Abbott, R., Abell, J. S., Abernathy, M., Abney, F. E., ... Zondag, E. (2023, June). The James Webb Space Telescope Mission. *PASP*, *135*(1048), 068001. doi: 10.1088/1538-3873/acd1b5

Gardner, J. P., Mather, J. C., Clampin, M., Doyon, R., Greenhouse, M. A., Hammel, H. B., ... Wright, G. S. (2006, April). The James Webb Space Telescope. *Space Science Reviews*, *123*(4), 485-606. doi: 10.1007/s11214-006-8315-7

Girelli, G., Bolzonella, M., & Cimatti, A. (2019, December). Massive and old quiescent galaxies at high redshift. *A & A*, *632*, A80. doi: 10.1051/0004-6361/201834547

Girelli, G., Pozzetti, L., Bolzonella, M., Giocoli, C., Marulli, F., & Baldi, M. (2020, February). The stellar-to-halo mass relation over the past 12 Gyr. I. Standard ΛCDM model. *A & A*, *634*, A135. doi: 10.1051/0004-6361/201936329

Grogin, N. A., Kocevski, D. D., Faber, S. M., Ferguson, H. C., Koekemoer, A. M., Riess, A. G., ... Yun, M. S. (2011, December). CANDELS: The Cosmic Assembly Near-infrared Deep Extragalactic Legacy Survey. *ApJS*, *197*(2), 35. doi: 10.1088/0067-0049/197/2/35

Groves, B. A., Heckman, T. M., & Kauffmann, G. (2006, October). Emission-line diagnostics of low-metallicity active galactic nuclei. *MNRAS*, *371*(4), 1559-1569. doi: 10.1111/j.1365-2966.2006.10812.x

Heckman, T., Borthakur, S., Wild, V., Schiminovich, D., & Bordoloi, R. (2017, September). COS-burst: Observations of the Impact of Starburst-driven Winds on the Properties of the Circum-galactic Medium. *ApJ*, *846*(2), 151. doi: 10.3847/1538-4357/aa80dc

Heckman, T. M., Baum, S. A., van Breugel, W. J. M., & McCarthy, P. (1989, March). Dynamical, Physical, and Chemical Properties of Emission-Line Nebulae in Cooling Flows. *ApJ*, *338*, 48. doi: 10.1086/167181

Ho, I. T., Medling, A. M., Bland-Hawthorn, J., Groves, B., Kewley, L. J., Kobayashi, C., ... Valiante, E. (2016, April). The SAMI Galaxy Survey: extraplanar gas, galactic winds and their association with star formation history. *MNRAS*, *457*(2), 1257-1278. doi: 10.1093/mnras/stw017

Ho, L. C., Filippenko, A. V., & Sargent, W. L. W. (1993, November). A Reevaluation of the Excitation Mechanism of LINERs. *ApJ*, *417*, 63. doi: 10.1086/173291

Ho, L. C., Filippenko, A. V., & Sargent, W. L. W. (1996, May). New Insights into the Physical Nature of LINERs from a Multiwavelength Analysis of the Nucleus of M81. *ApJ*, *462*, 183. doi: 10.1086/177140

Ho, L. C., Filippenko, A. V., & Sargent, W. L. W. (2003, January). A Search for "Dwarf" Seyfert Nuclei. VI. Properties of Emission-Line Nuclei in Nearby Galaxies. *ApJ*, *583*(1), 159-177. doi: 10.1086/345354

Hogg, D. W., Blanton, M. R., Brinchmann, J., Eisenstein, D. J., Schlegel, D. J., Gunn, J. E., ... Meiksin, A. (2004, January). The Dependence on Environment of the Color-Magnitude Relation of Galaxies. *ApJL*, *601*(1), L29-L32. doi: 10.1086/381749

Hopkins, A. M., Miller, C. J., Nichol, R. C., Connolly, A. J., Bernardi, M., Gómez, P. L., ... Lamb, D. Q. (2003, December). Star Formation Rate Indicators in the Sloan Digital Sky Survey. *ApJ*, *599*(2), 971-991. doi: 10.1086/379608

Horner, S. D., & Rieke, M. J. (2004, October). The near-infrared camera (NIRCam) for the James Webb Space Telescope (JWST). In J. C. Mather (Ed.), *Optical, infrared, and millimeter space telescopes* (Vol. 5487, p. 628-634). doi: 10.1117/12.552281

Jakobsen, P., Ferruit, P., Alves de Oliveira, C., Arribas, S., Bagnasco, G., Barho, R., ... Zincke, C. (2022, May). The Near-Infrared Spectrograph (NIRSpec) on the James Webb Space Telescope. I. Overview of the instrument and its capabilities. *A & A*, *661*, A80. doi: 10.1051/0004-6361/202142663

Johnson, B. D., Leja, J., Conroy, C., & Speagle, J. S. (2021, June). Stellar Population Inference with Prospector. *ApJS*, *254*(2), 22. doi: 10.3847/1538-4365/abef67

Kauffmann, G., Heckman, T. M., White, S. D. M., Charlot, S., Tremonti, C., Peng, E. W., ... York, D. (2003, May). The dependence of star formation history and internal structure on stellar mass for 10^5 low-redshift galaxies. *MNRAS*, *341*(1), 54-69. doi: 10.1046/j.1365-8711.2003.06292.x

Kennicutt, J., Robert C. (1998, January). Star Formation in Galaxies Along the Hubble Sequence. *ARA & A*, *36*, 189-232. doi: 10.1146/annurev.astro.36.1.189

Kennicutt, J., Robert C., Hao, C.-N., Calzetti, D., Moustakas, J., Dale, D. A., Bendo, G., ... Lee, J. C. (2009, October). Dust-corrected Star Formation Rates of Galaxies. I. Combinations of Hα and Infrared Tracers. *ApJ*, *703*(2), 1672-1695. doi: 10.1088/0004-637X/703/2/1672

Kewley, L. J., Dopita, M. A., Leitherer, C., Davé, R., Yuan, T., Allen, M., ... Sutherland, R. (2013, September). Theoretical Evolution of Optical Strong Lines across Cosmic Time. *ApJ*, *774*(2), 100. doi: 10.1088/0004-637X/774/2/100

Kewley, L. J., Dopita, M. A., Sutherland, R. S., Heisler, C. A., & Trevena, J. (2001, July). Theoretical Modeling of Starburst Galaxies. *ApJ*, *556*(1), 121-140. doi: 10.1086/321545

Kewley, L. J., Groves, B., Kauffmann, G., & Heckman, T. (2006, November). The host

galaxies and classification of active galactic nuclei. *MNRAS*, *372*(3), 961-976. doi: 10.1111/j.1365-2966.2006.10859.x

Kewley, L. J., Nicholls, D. C., & Sutherland, R. S. (2019, August). Understanding Galaxy Evolution Through Emission Lines. *ARA & A*, *57*, 511-570. doi: 10.1146/annurev-astro-081817-051832

Kim, D.-W. (1989, November). Interstellar Matter in Early-Type Galaxies: Optical Observations. *ApJ*, *346*, 653. doi: 10.1086/168048

King, A., & Pounds, K. (2015, August). Powerful Outflows and Feedback from Active Galactic Nuclei. *ARA & A*, *53*, 115-154. doi: 10.1146/annurev-astro-082214-122316

Koekemoer, A. M., Faber, S. M., Ferguson, H. C., Grogin, N. A., Kocevski, D. D., Koo, D. C., ... Yun, M. S. (2011, December). CANDELS: The Cosmic Assembly Near-infrared Deep Extragalactic Legacy Survey—The Hubble Space Telescope Observations, Imaging Data Products, and Mosaics. *ApJS*, *197*(2), 36. doi: 10.1088/0067-0049/197/2/36

Kriek, M., & Conroy, C. (2013, September). The Dust Attenuation Law in Distant Galaxies: Evidence for Variation with Spectral Type. *ApJL*, *775*(1), L16. doi: 10.1088/2041-8205/775/1/L16

Labbé, I., Huang, J., Franx, M., Rudnick, G., Barmby, P., Daddi, E., ... van der Werf, P. (2005, May). IRAC Mid-Infrared Imaging of the Hubble Deep Field-South: Star Formation Histories and Stellar Masses of Red Galaxies at z>2. *ApJL*, *624*(2), L81-L84. doi: 10.1086/430700

Lagos, P., Loubser, S. I., Scott, T. C., O'Sullivan, E., Kolokythas, K., Babul, A., ... Sengupta, C. (2022, November). Spatially resolved properties of early-type group-dominant galaxies with MUSE: gas content, ionization mechanisms, and metallicity gradients. *MNRAS*, *516*(4), 5487-5506. doi: 10.1093/mnras/stac2535

Leitherer, C., Schaerer, D., Goldader, J. D., Delgado, R. M. G., Robert, C., Kune, D. F., ... Heckman, T. M. (1999, July). Starburst99: Synthesis Models for Galaxies with Active Star Formation. *ApJS*, *123*(1), 3-40. doi: 10.1086/313233

Leja, J., Carnall, A. C., Johnson, B. D., Conroy, C., & Speagle, J. S. (2019, May). How to Measure Galaxy Star Formation Histories. II. Nonparametric Models. *ApJ*, *876*(1), 3. doi: 10.3847/1538-4357/ab133c

Leja, J., Tacchella, S., & Conroy, C. (2019, July). Beyond UVJ: More Efficient Selection of Quiescent Galaxies with Ultraviolet/Mid-infrared Fluxes. *ApJL*, *880*(1), L9. doi: 10.3847/2041-8213/ab2f8c

Lightsey, P. A., Atkinson, C., Clampin, M., & Feinberg, L. D. (2012, January). James Webb Space Telescope: large deployable cryogenic telescope in space. *Optical*

Engineering, *51*(1), 011003-011003-20. doi: 10.1117/1.OE.51.1.011003

Ly, C., Lee, J. C., Dale, D. A., Momcheva, I., Salim, S., Staudaher, S., ... Finn, R. (2011, January). The Hα Luminosity Function and Star Formation Rate Volume Density at z = 0.8 from the NEWFIRM Hα Survey. *ApJ*, *726*(2), 109. doi: 10.1088/0004-637X/726/2/109

Macchetto, F., Pastoriza, M., Caon, N., Sparks, W. B., Giavalisco, M., Bender, R., & Capaccioli, M. (1996, December). A survey of the ISM in early-type galaxies. I. The ionized gas. *A & A*, *120*, 463-488.

Madau, P., & Dickinson, M. (2014, August). Cosmic Star-Formation History. *ARAA*, *52*, 415-486. doi: 10.1146/annurev-astro-081811-125615

Maddox, N. (2018, November). [O II] as a proxy for star formation in AGN host galaxies: beware of extended emission line regions. *MNRAS*, *480*(4), 5203-5210. doi: 10.1093/mnras/sty2201

Maltby, D. T., Almaini, O., McLure, R. J., Wild, V., Dunlop, J., Rowlands, K., ... Talia, M. (2019, October). High-velocity outflows in massive post-starburst galaxies at z $>$ 1. *MNRAS*, *489*(1), 1139-1151. doi: 10.1093/mnras/stz2211

Man, A., & Belli, S. (2018, September). Star formation quenching in massive galaxies. *Nature Astronomy*, *2*, 695-697. doi: 10.1038/s41550-018-0558-1

Markwardt, C. B. (2009, September). Non-linear Least-squares Fitting in IDL with MPFIT. In D. A. Bohlender, D. Durand, & P. Dowler (Eds.), *Astronomical data analysis software and systems xviii* (Vol. 411, p. 251). doi: 10.48550/arXiv.0902.2850

Marsan, Z. C., Marchesini, D., Brammer, G. B., Geier, S., Kado-Fong, E., Labbé, I., ... Stefanon, M. (2017, June). A Spectroscopic Follow-up Program of Very Massive Galaxies at 3 $<$ z $<$ 4: Confirmation of Spectroscopic Redshifts, and a High Fraction of Powerful AGNs. *ApJ*, *842*(1), 21. doi: 10.3847/1538-4357/aa7206

McElwain, M. W., Feinberg, L. D., Perrin, M. D., Clampin, M., Mountain, C. M., Lallo, M. D., ... Zielinski, T. P. (2023, May). The James Webb Space Telescope Mission: Optical Telescope Element Design, Development, and Performance. *PASP*, *135*(1047), 058001. doi: 10.1088/1538-3873/acada0

Medling, A. M., U, V., Rich, J. A., Kewley, L. J., Armus, L., Dopita, M. A., ... Sutherland, R. (2015, April). Shocked gas in IRAS F17207-0014: ISM collisions and outflows. *MNRAS*, *448*(3), 2301-2311. doi: 10.1093/mnras/stv081

Menzel, M., Davis, M., Parrish, K., Lawrence, J., Stewart, A., Cooper, J., ... Bowers, C. (2023, May). The Design, Verification, and Performance of the James Webb Space Telescope. *PASP*, *135*(1047), 058002. doi: 10.1088/1538-3873/acbb9f

Minkowski, R., & Osterbrock, D. (1959, May). Interstellar Matter in Elliptical Nebulae. *ApJ*, *129*, 583. doi: 10.1086/146656

Mo, H., van den Bosch, F. C., & White, S. (2010). *Galaxy Formation and Evolution.*

Molina, M., Eracleous, M., Barth, A. J., Maoz, D., Runnoe, J. C., Ho, L. C., ... Walsh, J. L. (2018, September). The Shocking Power Sources of LINERs. *ApJ*, *864*(1), 90. doi: 10.3847/1538-4357/aad5ed

Momcheva, I. G., Brammer, G. B., van Dokkum, P. G., Skelton, R. E., Whitaker, K. E., Nelson, E. J., ... Wuyts, S. (2016, August). The 3D-HST Survey: Hubble Space Telescope WFC3/G141 Grism Spectra, Redshifts, and Emission Line Measurements for ~100,000 Galaxies. *ApJS*, *225*(2), 27. doi: 10.3847/0067-0049/225/2/27

Moresco, M., Pozzetti, L., Cimatti, A., Zamorani, G., Bolzonella, M., Lamareille, F., ... Welikala, N. (2013, October). Spot the difference. Impact of different selection criteria on observed properties of passive galaxies in zCOSMOS-20k sample. *A & A*, *558*, A61. doi: 10.1051/0004-6361/201321797

Mowla, L. A., Cutler, S. E., Brammer, G. B., Momcheva, I. G., Whitaker, K. E., van Dokkum, P. G., ... van der Wel, A. (2022, July). 3D-DASH: The Widest Near-infrared Hubble Space Telescope Survey. *ApJ*, *933*(2), 129. doi: 10.3847/1538-4357/ac71af

Muzzin, A., Marchesini, D., Stefanon, M., Franx, M., McCracken, H. J., Milvang-Jensen, B., ... van Dokkum, P. G. (2013, November). The Evolution of the Stellar Mass Functions of Star-forming and Quiescent Galaxies to z = 4 from the COSMOS/UltraVISTA Survey. *ApJ*, *777*(1), 18. doi: 10.1088/0004-637X/777/1/18

Nella, J., Atcheson, P. D., Atkinson, C. B., Au, D., Bronowicki, A. J., Bujanda, E., ... Woods, R. (2004, October). James Webb Space Telescope (JWST) Observatory architecture and performance. In J. C. Mather (Ed.), *Optical, infrared, and millimeter space telescopes* (Vol. 5487, p. 576-587). doi: 10.1117/12.548928

Osterbrock, D. E. (1960, September). Interstellar Matter in Elliptical Galaxies. II. *ApJ*, *132*, 325. doi: 10.1086/146930

Osterbrock, D. E. (1989). *Astrophysics of gaseous nebulae and active galactic nuclei.*

Osterbrock, D. E., & Ferland, G. J. (2006). *Astrophysics of gaseous nebulae and active galactic nuclei.*

Park, M., Belli, S., Conroy, C., Tacchella, S., Leja, J., Cutler, S. E., ... Emami, R. (2023, aug). Rapid quenching of galaxies at cosmic noon. *The Astrophysical Journal*, *953*(1), 119. Retrieved from https://doi.org/10.3847%2F1538-4357%2Facd54a doi: 10.3847/1538-4357/acd54a

Phillips, M. M., Jenkins, C. R., Dopita, M. A., Sadler, E. M., & Binette, L. (1986, May). Ionized gas in elliptical and SO galaxies. I. A survey for H alpha and N II emission. *AJ*, *91*, 1062-1085. doi: 10.1086/114083

Pontzen, A., Tremmel, M., Roth, N., Peiris, H. V., Saintonge, A., Volonteri, M., ... Governato, F. (2017, February). How to quench a galaxy. *MNRAS*, *465*(1), 547-558. doi: 10.1093/mnras/stw2627

Pozzetti, L., Bolzonella, M., Zucca, E., Zamorani, G., Lilly, S., Renzini, A., ... Scoville, N. (2010, November). zCOSMOS - 10k-bright spectroscopic sample. The bimodality in the galaxy stellar mass function: exploring its evolution with redshift. *A & A*, *523*, A13. doi: 10.1051/0004-6361/200913020

Quai, S., Pozzetti, L., Citro, A., Moresco, M., & Cimatti, A. (2018, August). Galaxies in the act of quenching star formation. *MNRAS*, *478*(3), 3335-3355. doi: 10.1093/mnras/sty1045

Rees, M. J. (1997, January). The Universe at z $>$ 5: When and How Did the 'Dark Age' End? In N. R. Tanvir, A. Aragon-Salamanca, & J. V. Wall (Eds.), *The hubble space telescope and the high redshift universe* (p. 115). doi: 10.48550/arXiv.astro-ph/9608196

Rieke, G. H., Ressler, M. E., Morrison, J. E., Bergeron, L., Bouchet, P., García-Marín, M., ... Walker, H. (2015, July). The Mid-Infrared Instrument for the James Webb Space Telescope, VII: The MIRI Detectors. *PASP*, *127*(953), 665. doi: 10.1086/682257

Rieke, M., Kelly, D., Horner, S., & NIRCam Team. (2005, December). The Near Infrared Camera (NIRCam) for the James Webb Space Telescope (JWST). In *American astronomical society meeting abstracts* (Vol. 207, p. 115.09).

Rieke, M. J., Baum, S. A., Beichman, C. A., Crampton, D., Doyon, R., Eisenstein, D., ... Young, E. T. (2003, March). NGST NIRCam Scientific Program and Design Concept. In J. C. Mather (Ed.), *Ir space telescopes and instruments* (Vol. 4850, p. 478-485). doi: 10.1117/12.489103

Rieke, M. J., Kelly, D. M., Misselt, K., Stansberry, J., Boyer, M., Beatty, T., ... Young, E. T. (2023, February). Performance of NIRCam on JWST in Flight. *PASP*, *135*(1044), 028001. doi: 10.1088/1538-3873/acac53

Rigby, J., Perrin, M., McElwain, M., Kimble, R., Friedman, S., Lallo, M., ... Zonak, S. (2023, April). The Science Performance of JWST as Characterized in Commissioning. *PASP*, *135*(1046), 048001. doi: 10.1088/1538-3873/acb293

Rosa-González, D., Terlevich, E., & Terlevich, R. (2002, May). An empirical calibration of star formation rate estimators. *MNRAS*, *332*(2), 283-295. doi: 10.1046/j.1365-8711.2002.05285.x

Salim, S., & Narayanan, D. (2020, August). The Dust Attenuation Law in Galaxies. *ARAA*, *58*, 529-575. doi: 10.1146/annurev-astro-032620-021933

Salim, S., Rich, R. M., Charlot, S., Brinchmann, J., Johnson, B. D., Schiminovich, D., ... Yi, S. K. (2007, December). UV Star Formation Rates in the Local Universe. *ApJS*, *173*(2), 267-292. doi: 10.1086/519218

Sanders, R. L., Shapley, A. E., Reddy, N. A., Kriek, M., Siana, B., Coil, A. L., ... Barro, G. (2020, January). The MOSDEF survey: direct-method metallicities and ISM conditions at z $\sim$ 1.5-3.5. *MNRAS*, *491*(1), 1427-1455. doi: 10.1093/mnras/stz3032

Schreiber, C., Glazebrook, K., Nanayakkara, T., Kacprzak, G. G., Labbé, I., Oesch, P., ... Straatman, C. (2018, October). Near infrared spectroscopy and star-formation histories of $3 \leq z \leq 4$ quiescent galaxies. *A & A*, *618*, A85. doi: 10.1051/0004-6361/201833070

Shapley, A. E. (2011, September). Physical Properties of Galaxies from z = 2-4. *ARAA*, *49*(1), 525-580. doi: 10.1146/annurev-astro-081710-102542

Shapley, A. E., Reddy, N. A., Kriek, M., Freeman, W. R., Sanders, R. L., Siana, B., ... de Groot, L. (2015, March). The MOSDEF Survey: Excitation Properties of z $\sim$ 2.3 Star-forming Galaxies. *ApJ*, *801*(2), 88. doi: 10.1088/0004-637X/801/2/88

Shapley, A. E., Sanders, R. L., Shao, P., Reddy, N. A., Kriek, M., Coil, A. L., ... Barro, G. (2019, August). The MOSDEF Survey: Sulfur Emission-line Ratios Provide New Insights into Evolving Interstellar Medium Conditions at High Redshift. *ApJL*, *881*(2), L35. doi: 10.3847/2041-8213/ab385a

Shields, J. C. (1992, November). Normal O Stars in Dense Media Generate LINERs. *ApJl*, *399*, L27. doi: 10.1086/186598

Singh, R., van de Ven, G., Jahnke, K., Lyubenova, M., Falcón-Barroso, J., Alves, J., ... Ziegler, B. (2013, October). The nature of LINER galaxies:. Ubiquitous hot old stars and rare accreting black holes. *A & A*, *558*, A43. doi: 10.1051/0004-6361/201322062

Skelton, R. E., Whitaker, K. E., Momcheva, I. G., Brammer, G. B., van Dokkum, P. G., Labbé, I., ... Wuyts, S. (2014, October). 3D-HST WFC3-selected Photometric Catalogs in the Five CANDELS/3D-HST Fields: Photometry, Photometric Redshifts, and Stellar Masses. *ApJS*, *214*(2), 24. doi: 10.1088/0067-0049/214/2/24

Sparks, W. B., Macchetto, F., & Golombek, D. (1989, October). Imaging Observations of Gas and Dust in NGC 4696 and Implications for Cooling Flow Models. *ApJ*, *345*, 153. doi: 10.1086/167890

Stasińska, G., Cid Fernandes, R., Mateus, A., Sodré, L., & Asari, N. V. (2006, September). Semi-empirical analysis of Sloan Digital Sky Survey galaxies -

III. How to distinguish AGN hosts. *MNRAS*, *371*(2), 972-982. doi: 10.1111/j.1365-2966.2006.10732.x

Steidel, C. C., Strom, A. L., Pettini, M., Rudie, G. C., Reddy, N. A., & Trainor, R. F. (2016, August). Reconciling the Stellar and Nebular Spectra of High-redshift Galaxies. *ApJ*, *826*(2), 159. doi: 10.3847/0004-637X/826/2/159

Straatman, C. M. S., Spitler, L. R., Quadri, R. F., Labbé, I., Glazebrook, K., Persson, S. E., ... Whitaker, K. E. (2016, October). The FourStar Galaxy Evolution Survey (ZFOURGE): Ultraviolet to Far-infrared Catalogs, Medium-bandwidth Photometric Redshifts with Improved Accuracy, Stellar Masses, and Confirmation of Quiescent Galaxies to z $\sim$ 3.5. *ApJ*, *830*(1), 51. doi: 10.3847/0004-637X/830/1/51

Strom, A. L., Steidel, C. C., Rudie, G. C., Trainor, R. F., Pettini, M., & Reddy, N. A. (2017, February). Nebular Emission Line Ratios in z = 2-3 Star-forming Galaxies with KBSS-MOSFIRE: Exploring the Impact of Ionization, Excitation, and Nitrogen-to-Oxygen Ratio. *ApJ*, *836*(2), 164. doi: 10.3847/1538-4357/836/2/164

Strömgren, B. (1948, September). On the Density Distribution and Chemical Composition of the Interstellar Gas. *ApJ*, *108*, 242. doi: 10.1086/145068

Sutherland, R. S., & Dopita, M. A. (1993, September). Cooling Functions for Low-Density Astrophysical Plasmas. *ApJS*, *88*, 253. doi: 10.1086/191823

Tacchella, S., Conroy, C., Faber, S. M., Johnson, B. D., Leja, J., Barro, G., ... Yesuf, H. M. (2022, February). Fast, Slow, Early, Late: Quenching Massive Galaxies at z $\sim$ 0.8. *ApJ*, *926*(2), 134. doi: 10.3847/1538-4357/ac449b

Taylor, E. N., Franx, M., van Dokkum, P. G., Bell, E. F., Brammer, G. B., Rudnick, G., ... Rix, H.-W. (2009, April). The Rise of Massive Red Galaxies: The Color-Magnitude and Color-Stellar Mass Diagrams for $z_{phot} \lesssim 2$ from the Multiwavelength Survey by Yale-Chile. *ApJ*, *694*(2), 1171-1199. doi: 10.1088/0004-637X/694/2/1171

Terlevich, R., & Melnick, J. (1985, April). Warmers : the missing link between Starburst and Seyfert galaxies. *MNRAS*, *213*, 841-856. doi: 10.1093/mnras/213.4.841

Thomas, D., Maraston, C., Schawinski, K., Sarzi, M., & Silk, J. (2010, June). Environment and self-regulation in galaxy formation. *MNRAS*, *404*(4), 1775-1789. doi: 10.1111/j.1365-2966.2010.16427.x

Tielens, A. G. G. M. (2005). *The Physics and Chemistry of the Interstellar Medium.*

Tremonti, C. A., Heckman, T. M., Kauffmann, G., Brinchmann, J., Charlot, S., White, S. D. M., ... Brinkmann, J. (2004, October). The Origin of the Mass-Metallicity

Relation: Insights from 53,000 Star-forming Galaxies in the Sloan Digital Sky Survey. *ApJ*, *613*(2), 898-913. doi: 10.1086/423264

Übler, H., Maiolino, R., Curtis-Lake, E., Pérez-González, P. G., Curti, M., Perna, M., ... Rawle, T. (2023a, February). GA-NIFS: A massive black hole in a low-metallicity AGN at $z \sim 5.55$ revealed by JWST/NIRSpec IFS. *arXiv e-prints*, arXiv:2302.06647. doi: 10.48550/arXiv.2302.06647

Übler, H., Maiolino, R., Curtis-Lake, E., Pérez-González, P. G., Curti, M., Perna, M., ... Rawle, T. (2023b, February). GA-NIFS: A massive black hole in a low-metallicity AGN at $z \sim 5.55$ revealed by JWST/NIRSpec IFS. *arXiv e-prints*, arXiv:2302.06647. doi: 10.48550/arXiv.2302.06647

Veilleux, S., & Osterbrock, D. E. (1987, February). Spectral Classification of Emission-Line Galaxies. *ApJS*, *63*, 295. doi: 10.1086/191166

Voit, G. M., & Donahue, M. (1990, September). Self-irradiated Cooling Condensations: The Source of the Optical Line Emission from Cooling Flows. *ApJl*, *360*, L15. doi: 10.1086/185801

Weigel, A. K., Schawinski, K., & Bruderer, C. (2016, June). Stellar mass functions: methods, systematics and results for the local Universe. *MNRAS*, *459*(2), 2150-2187. doi: 10.1093/mnras/stw756

Whitaker, K. E., Labbé, I., van Dokkum, P. G., Brammer, G., Kriek, M., Marchesini, D., ... Wake, D. A. (2011, July). The NEWFIRM Medium-band Survey: Photometric Catalogs, Redshifts, and the Bimodal Color Distribution of Galaxies out to z ~3. *ApJ*, *735*(2), 86. doi: 10.1088/0004-637X/735/2/86

White, S. D. M., & Rees, M. J. (1978, May). Core condensation in heavy halos: a two-stage theory for galaxy formation and clustering. *MNRAS*, *183*, 341-358. doi: 10.1093/mnras/183.3.341

Williams, R. J., Quadri, R. F., Franx, M., van Dokkum, P., & Labbé, I. (2009, February). Detection of Quiescent Galaxies in a Bicolor Sequence from Z = 0-2. *ApJ*, *691*(2), 1879-1895. doi: 10.1088/0004-637X/691/2/1879

Wright, G. S., Rieke, G. H., Glasse, A., Ressler, M., García Marín, M., Aguilar, J., ... Wolff, S. (2023, April). The Mid-infrared Instrument for JWST and Its In-flight Performance. *PASP*, *135*(1046), 048003. doi: 10.1088/1538-3873/acbe66

Wright, G. S., Wright, D., Goodson, G. B., Rieke, G. H., Aitink-Kroes, G., Amiaux, J., ... Zhender, A. (2015, July). The Mid-Infrared Instrument for the James Webb Space Telescope, II: Design and Build. *PASP*, *127*(953), 595. doi: 10.1086/682253

Yan, R., & Blanton, M. R. (2012a, March). The Nature of LINER-like Emission in Red Galaxies. *ApJ*, *747*(1), 61. doi: 10.1088/0004-637X/747/1/61

Yan, R., & Blanton, M. R. (2012b, March). The Nature of LINER-like Emission in Red Galaxies. *ApJ*, *747*(1), 61. doi: 10.1088/0004-637X/747/1/61

Zakamska, N. L., Hamann, F., Pâris, I., Brandt, W. N., Greene, J. E., Strauss, M. A., ... Ross, N. P. (2016, July). Discovery of extreme [O III] λ5007 Å outflows in high-redshift red quasars. *mnras*, *459*(3), 3144-3160. doi: 10.1093/mnras/stw718

Zheng, Y., Wild, V., Lahén, N., Johansson, P. H., Law, D., Weaver, J. R., & Jimenez, N. (2020, October). Comparison of stellar populations in simulated and real post-starburst galaxies in MaNGA. *MNRAS*, *498*(1), 1259-1277. doi: 10.1093/mnras/staa2358